

A comprehensive review of nonlinear oscillators in hydrokinetic energy harnessing using flow-induced vibrations

Yanfang Lv^c, Liping Sun^c, Michael M. Bernitsas^{b,d,e}, Hai Sun^{a,b,*}

^a College of Aerospace and Civil Engineering, Harbin Engineering University, China

^b Marine Renewable Energy Laboratory, Dept. of Naval Architecture & Marine Engineering, University of Michigan, 2600 Draper Road, Ann Arbor, MI, 48109-2145, USA

^c College of Ship Building Engineering, Harbin Engineering University, China

^d Department of Mechanical Engineering, University of Michigan, USA

^e Vortex Hydro Energy, Ann Arbor, MI, USA



ARTICLE INFO

Keywords:

Nonlinear oscillator
Flow-induced vibration
Vortex induced vibration
Galloping
Hydrodynamic stiffness
Nonlinear stiffness
Nonlinear adaptive damping

ABSTRACT

A comprehensive review of hydrokinetic energy converters based on **alternating lift technology** (ALT) is provided. Emphasis is on nonlinear oscillators based on Flow Induced Vibration (FIV) or Oscillation (FIO). Due to strong coupling in Fluid-Structure Interaction (FSI), and in order to maximize the hydrokinetic harnessed energy, design of nonlinear oscillators and analysis by model tests or computational fluid dynamics dominates this area. Research confirmed that the nonlinear oscillator can harvest energy from a **stochastic** excitation modeled by a **generic wide spectrum**, and overcome the most severe oscillator limitations: specifically, the need for continuous frequency tuning due to the narrow bandwidth response, and low efficiency outside the narrow bandwidth oscillator response. This review covers the following aspects of nonlinear oscillators in ALT converters: (1) Geometric changes in oscillator cross-section; e.g., circular, square, rectangular, or trilateral shapes. (2) Passive turbulence control of FIV/FIO. (3) Position based nonlinear stiffness. (4) Multi-cylinder synergistic FIV/FIO. (5) Mechanically linked oscillators. (6) Velocity-based, nonlinear, adaptive harnessing damping.

1. Introduction

As a phenomenon encountered frequently, fluid-structure interaction occurs in slender structures, with bluff cross-section, such as a cylinder or prism in transverse flow, resulting in flow induced vibration/oscillation [1–4]. Vortex-induced vibration (VIV) and **galloping** are the common forms of FIV. Those phenomena can be used for harnessing hydrokinetic energy.

In recent years, harnessing of **horizontal marine hydrokinetic** (MHK) **energy**, which is **abundant in steady current flows**, such as those in rivers, tides, and ocean currents have attracted a lot of attention. Devices used to harness horizontal MHK energy are referred to as **Current Energy Converters (CEC)** including FIV based and turbines. The vortex induced vibration for aquatic clean energy (VIVACE) converter [5] proposed in 2006 uses alternating lift [6] rather than steady-lift like turbines. It is based on VIV, galloping, and their coexistence, and can harvest MHK energy from flows as slow as **0.343 m/s** with substantial efficiency

[7–11]. With the introduction of nonlinear piecewise stiffness, onset of harnessed MHK power is achieved at 0.274 m/s [12]. The class of CEC using alternating lift are called Alternating Lift Technologies (ALT) [6]. This mechanism is similar to that of propulsion of fish in water. Fish thrive in wake streets with alternating vortices [13], thus making ALTs compatible with the marine environment.

In FIV, different flow regions, such as VIV and galloping, can be placed back-to-back, leading to a wide range of high amplitude responses by the properly design of the ALT Converter. This band is in terms of flow velocity relating to the oscillating frequency through the reduced velocity parameter [2–4]. It starts with the VIV initial branch near the natural oscillation frequency of the cylinder in quiescent water. The transition region in-between of the VIV and galloping should be eliminated to achieve the potential maximum energy through the entire flow region. Ideally, the initiation of galloping should happen as the end of the upper branch of VIV. This phenomenon requires the understanding of the regions, which consist of termination of synchronization for VIV, then follows the onset of galloping.

* Corresponding author. Marine Renewable Energy Laboratory, Dept. of Naval Architecture & Marine Engineering, University of Michigan, 2600 Draper Road, Ann Arbor, MI, 48109-2145, USA.

E-mail address: sunhai2009@gmail.com (H. Sun).

Abbreviations

a	Radius of Coil [mm]	by the Cylinders [W]
λ_1	Linear Term of Nonlinear Galloping Force Coefficient	Harnessed Power [W]
λ_3	Cubic Term of Nonlinear Galloping Force Coefficient	Average Extracted Power [W]
A	Amplitude [m]	Passive Turbulence Control
A_{max}	Maximum Amplitude [m]	PTO System Power Take-Off System
ALT	Alternating Lift Technology	PZT Piezoelectric Ceramic Transducer
c_{adapt}	Adaptive Harnessing Damping Coefficient [Ns/m]	R External Electrical Load Resistance [kΩ]
c_h	Damping Factor [Ns^2/m^2]	Re Reynolds Number
$c_{harness}$	Harnessing Damping Coefficient [Ns/m]	RAO Response Amplitude Operator
$c_{structure}$	Structural Damping Coefficient [Ns/m]	Ref Reference
c_{total}	Total System Damping Coefficient [Ns/m]	S_{cs} Area of Cross-Section [mm 2]
$c_{virtual}$	Linear Viscous Damping [Ns/m]	S Transverse spacing between Two Staggered Cylinders [mm]
C_A	Inviscid-Fluid (Ideal) Added Mass Coefficient in Quiescent Water	SG Soft Galloping
C_y	Nonlinear Galloping Force Coefficient	SS Strong Suppression
CEC	Current Energy Converters	T_{osc} Period of Oscillation [sec]
CFD	Computational Fluid Dynamics	T Center-to-center Spacing between Two Staggered Cylinders [mm]
CPFD	Cyber-Physical Fluid Dynamics	TrSL Transition in Shear Layer
d	Diameter of Rod [mm]	U Flow Velocity [m/s]
D	Diameter of Cylinder [mm]	$U^* = \frac{U}{f_{n,water} D}$ Reduced Velocity
$f_{n,water} = \frac{1}{2\pi} \sqrt{\frac{K}{m_{osc}+m_a}}$	Natural Frequency in Water [Hz]	URANS Unsteady Reynolds Average Navier-Stokes
$f_{n,vac} = \frac{1}{2\pi} \sqrt{\frac{K}{m_{osc}}}$	Natural Frequency in Vacuum [Hz]	Vck System Virtual Damper-Spring System
f_{osc}	Dominant Oscillating Frequency of Cylinder [Hz]	VIPEH Vortex Induced Piezoelectric Energy Harvester
$f^* = \frac{f_{osc}}{f_{n,vac}}$	Ratio of Oscillating Frequency of Cylinder's and Natural Frequency	VIV Vortex Induced Vibration
$F_{damping}$	Harnessing Damping Force [N]	VIVACE Vortex Induced Vibration for Aquatic Clean Energy
F_{fluid}	Fluid Force [N]	VIVEC VIV-based Energy Converter
$F_{restoring-force}$	Restoring Force [N]	V_{rms}^2 Square of the root mean square oscillation velocities
FIV	Flow Induced Vibration	W Width of Rectangular Cylinder in the Streamwise Direction [m]
FIO	Flow Induced Oscillation	WS1 Weak Suppression 1
FSI	Fluid-Structure Interaction	WS2 Weak Suppression 2
G	Fixed Distance between the Magnet and Plate [m]	X Maximum In-flow Spacing of Four-cylinder Arrays [mm]
GPEH	Galloping-Based Piezoelectric Energy Harvester	Y Maximum Transverse Spacing of Four-cylinder Arrays [mm]
H	Height of Rectangular Cylinder in the Vertical Direction [m]	y Displacement of the Cylinder [m]
$H' = k + p$	Roughness Height [mm]	\dot{y} Velocity of the Cylinder [m/s]
HG1	Hard Galloping 1	\ddot{y} Acceleration of the Cylinder [m/s 2]
HG2	Hard Galloping 2	y_0 Transition Location of Nonlinear piecewise restoring force [m]
HBM	Harmonic Balance Method	η_{mech} Mechanical Efficiency [%]
k	Grit's Average Height [mm]	η_M Maximum Efficiency [%]
K	Spring Stiffness [N/m]	$\eta_{harness}$ Power Harnessed Efficiency [%]
$K_{cubic,n}$	Cubic Nonlinear Term in Restoring Force [N/m 3]	ζ Mechanical Damping Ratio
$K_{virtual}$	Virtual Spring Stiffness [N/m]	ζ_m Electromagnetic Damping Ratio
L	Downstream Distance between Two Tandem Cylinders [mm]	$\zeta_{total} = \zeta_{structure} + \zeta_{harness}$ Total System Damping Ratio
L_c	Length of Coil [mm]	$\zeta_{harness} = \frac{c_{harness}}{2\sqrt{K(m_{osc}+m_a)}}$ Harnessing Damping Ratio
L_{en}	Length of Oscillating Cylinder [mm]	$\zeta_{structure} = \frac{c_{structure}}{2\sqrt{K(m_{osc}+m_a)}}$ Structural Damping Ratio
L_{sp}	Length of Splitter-Plate [mm]	ρ Density of Fluid [kg/m 3]
LTFSW Channel	Low Turbulence Free Surface Water Channel	$\sigma = W/H$ Cross-Sectional Aspect Ratio
m_a	Added Mass [kg]	θ_0 Orientation Angle of the Oscillator with Respect to the Flow Direction [°]
m_d	Mass of Liquid Displaced by Cylinder [kg]	δ Base Angle of Equilateral Triangular [°]
m_{osc}	Oscillating Mass [kg]	α Attack angle [°]
$m^* = m_{osc}/m_d$	Mass Ratio	β Triangle Vertex Angle [°]
$m^*\zeta$	Mass-Damping Coefficient [kg]	α_{PTC} Placement Angle of Roughness Strips [°]
M	Mass of Oscillator [kg]	θ_{sac} Strip Area Coverage [°]
MHK	Marine Hydrokinetic	θ Circumferential Location [°]
MRELab	Marine Renewable Energy Laboratory	Δx Horizontal Distance between Two Magnets [mm]
N	Number of Cylinders	Δy Vertical Distance between Two Magnets [mm]
p	Stack Height of Roughness Strip [mm]	ω_{osc} Angular Oscillation Frequency [rad/s]
P_{ele}	Electric Power Per Length of Cylinder [W/m]	γ Flow Incidence Angle of Multiple Oscillator Arrangement [°]
$P_{Fluid} = 0.5\rho U^3 (2A_{max} + D)L_{en}$ Power in Fluid through the Area Swept		

Previous research [14] confirmed that the nonlinear oscillator can efficiently obtain or convert energy from a wider vibration spectrum, which overcomes following limitation, for instance, frequency turning, narrow bandwidth, and low efficiency.

According to considerable amount of studies, for a VIV Converter, the upper branch is where mostly the energy is extracted. The nonlinear cubic stiffness oscillator will expend the VIV upper branch, resulting in expanding the bandwidth of the harnessed of the oscillator [15]. Some Refs. [16,17] introduced nonlinear hardening stiffness by a cantilever beam with two additional plates, so that improve the performance of harnessed energy for FIV Converter. In recent years, many studies [7, 18–20] have been conducted, observing that the shifting in synchronization branches of VIV higher flow velocities when stiffness increases.

Besides that, in order to achieve a further increase of the harnessed power, nonlinear displacement-depending spring (piecewise and adaptive piecewise stiffness) are investigated [12,21,22]. Nonlinear damping, such as velocity-dependent adaptive damping is also studied [23]. Generally, higher power conversion can be achieved by correctly introducing the nonlinearities in oscillator [24].

The purpose of this paper is to provide a comprehensive review of ALT energy converter technologies which are based on flow-induced vibrations; emphasis is placed on the nonlinear aspects of the oscillator. The harnessed power from FIV of a linear mechanical oscillator is explored in Section 2, in order to make a comparison with nonlinear oscillators in Sections 3–8. Section 3 provides the energy conversion of the results from geometric changes in the cross-section. The enhancing harnessed power of passive control, in terms of adjusting the parameters of the power take-off system (PTO), is presented in Section 4. Section 5 gives an overview of the nonlinear stiffness (position-based) effect on the harnessed power. Converters with multiple oscillators and cylinder interactions are presented in Section 6. Converters with multiple mechanically-linked oscillators are studied in Section 7. Section 8 gives an overview of the nonlinear adaptive damping (velocity-based) effect on the harnessed power. Conclusions are summarized at the end.

2. Hydrodynamic nonlinearity IN FIO

Flow-induced oscillations are highly nonlinear fluid-structure interaction phenomena due to the hydrodynamic excitation. The two FIO phenomena driving ALT converters are VIV and galloping. As is well known, those driving mechanisms are highly nonlinear and of completely different nature. In this section, we briefly review these nonlinear phenomena and the harnessed hydrokinetic energy using a linear mechanical oscillator. These results will serve as a basis for

comparison of nonlinear oscillators and assessment of their performance in Sections 3–8.

2.1. Vortex induced vibrations

Vortex induced vibration was first recorded in 1504 by Leonardo da Vinci. Further, the first mathematical formulation [1] was established by Strouhal in 1878. Due to lock-in of vortex shedding to the cylinder oscillation, the VIV synchronization range covers a broad range of velocities, as shown in Fig. 1. Typical VIV regions mainly consist of the initial branch, the upper branch and the lower branch to de-synchronization. The range of each branch varies depending on the flow regime as defined by Zdravkovich as function of Reynolds (Re) number [26]. Specifically, in the TrSL2 flow regime (about $2,000 < Re < 20,000$) the VIV branches are shown in Fig. 1(b) by Khalak and Williamson [32]. In the TrSL3 flow regime (about $20,000 < Re < 300,000$), the VIV branches are shown by Raghavan and Bernitsas [74] and are different. The transition between TrSL2 and TrSL3 is shown as a smooth progression by Banerjee [95]. It is a destructive phenomenon and in engineering practice extensive effort is made to suppress it [25]. VIV is a highly scalable phenomenon occurring at all Reynolds numbers (Re) except: (a) $Re < 40$; (b) The Tritton transition range $200 < Re < 400$

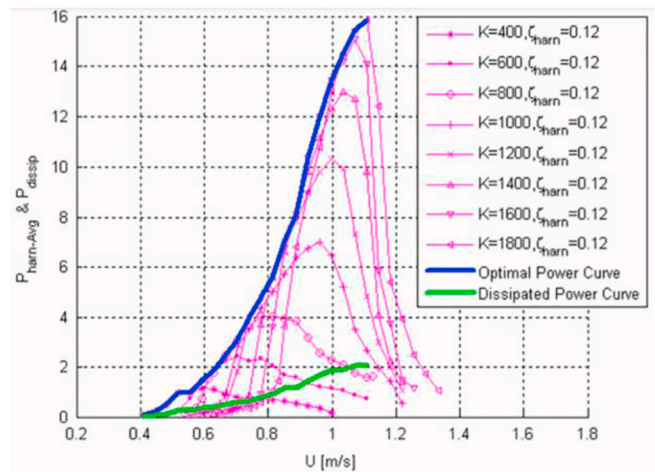
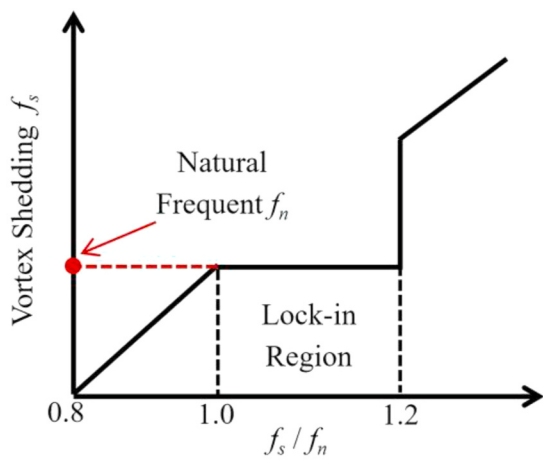
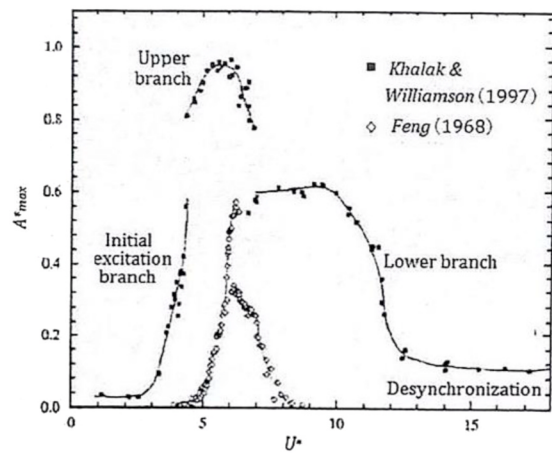


Fig. 2. The variation of average power with flow velocity for different K_{virtual} [19] ($L_{\text{en}} = 914.4 \text{ mm}$; $D = 88.9 \text{ mm}$).



(a)



(b)

Fig. 1. Schematic: (a) Lock-in Region. (b) Typical VIV regions.

where the flow inside vortices becomes turbulent; (c) The critical flow regime where the boundary layer transitions from laminar to turbulent (Fig. 2).

There are some comprehensive review books and papers for the subjects as vortex induced vibration [2–5], flow around cylinders [26], suppression of VIV [25], Fluid Structure Interaction (FSI) [27], mapping of turbulence stimulation to FIO [8], enhancement of energy harnessing based on FIO [6,9]. The above references provide new researchers with comprehensive information on VIV and galloping, and facilitate the publication of FIV/O studies.

2.2. Galloping

Galloping is a motion perpendicular to the flow, besides that, is also an aero/hydro-elastic instability, which has the characteristics of low frequency and large amplitude. Galloping, which can be observed to have fundamentally different properties than VIV, is another form of FIO. It is different from the VIV that the galloping has not the lock-in region and cannot be self-limiting. For the above reason, unless being constrained by the restoring springs, or structural configuration, or any combination of those, galloping, induced by the shear layer instability, will continue to force the oscillator traveling in one direction until elasticity reverses its direction. Amplitude will increase as the flow velocity increases until structural failure.

2.3. Mass-ratio and spring stiffness effect on FIO

In this section, linear mechanical oscillators introduced to explore FIO phenomena [28–30] by changing the oscillating mass m_{osc} and spring (elastically support the oscillator) stiffness K are reviewed. Changing the value of m_{osc} or K can directly change the natural frequency $f_{n,water}$ of the oscillator in water. It is well known that $f_{n,water}$ is a very important parameter in designing any CEC to reach optimal performance. Its mathematical expression can be written as:

$$f_{n,water} = \frac{1}{2\pi} \sqrt{\frac{K}{m_{osc} + C_A m_d}} \quad (1)$$

$$m_d = \frac{\pi}{4} \rho D^2 L_{en} \quad (2)$$

where L_{en} , C_A and m_d are, respectively, the length of the oscillating cylinder, the inviscid-fluid (ideal) added mass coefficient in quiescent water, and the mass of the liquid displaced by the cylinder. Where ρ and D are the density of fluid and diameter of cylinder, respectively. For a circular cylinder $C_A = 1$. $f_{n,water}$ affects the FIO synchronization range in each VIV and galloping range of oscillation. It also affects the amplitude and frequency response of the oscillator. Therefore, it is meaningful to analyze the effects of m_{osc} and K on FIO response for a linear oscillator. In addition, the impact of m_{osc} and K have been studied experimentally for several decades - since the 1950's - and have been recently explained [29] (Section 2.4).

Given the controversy surrounding the importance or not of the ideal added mass C_A [3,4,6], it is preferable to use the vacuum natural frequency of the oscillator, thus, ignoring the ideal C_A , and the value of m_d . The expression for $f_{n,vac}$ is:

$$f_{n,vac} = \frac{1}{2\pi} \sqrt{\frac{K}{m_{osc}}} \quad (3)$$

As shown in Section 2.4 [29], the dominant response frequency f_{osc} , being established the relationship with $f_{n,vac}$, can be nondimensionalized as

$$f^* = \frac{f_{osc}}{f_{n,vac}} \quad (4)$$

The spring stiffness is a much easier variable to implement compared

to the other variables, especially for the virtual spring stiffness, $K_{virtual}$ [18,19,30].

In 2011, the controller-emulated damper-spring system [18] was implemented by introducing a controller to set the values of K [19]. This enabled systematic experimental study for the performance of hydro-kinetic harvested power of the VIVACE converter at $40,000 < Re < 120,000$ ($0.4 < U < 1.1$ m/s) in the Low Turbulence Free Surface Water (LTFSW) channel in the Marine Renewable Energy Laboratory (MRE-Lab) of the University of Michigan. The variation range of K was 400 N/m $< K < 1,800$ N/m, and it was set by the computer controller after extensive calibration. The results showed that the maximum amplitude observed was 1.78D at $K = 1,200$ N/m. Moreover, the variation of synchronization range was small in terms of reduced velocity. This is due to the reason that increasing the spring stiffness will directly enhance its corresponding restoring force acting on the cylinder, making VIV synchronization range move to higher flow velocities. Fig. 2 shows that, the maximum average power increases with increasing K . Additionally, the optimal power envelope was obtained for the first time. The maximum harnessed power was 15.85W at $U = 1.11$ m/s when $K = 1,800$ N/m. The power density was 98.2W/m³ by combining oscillators in the form of an array.

In order to maximize the power efficiency based on the forced vibration experiments [31], the transverse VIV of a cylinder was investigated [10]. The authors analyzed the variation of energy efficiency with mechanical damping ζ and mass ratio m^* defined as the ratio of oscillating mass to the mass of the displaced liquid. The results showed that the maximum efficiency (η_M) is mainly dependent on the mass-damping coefficient ($m^*\zeta$, in Fig. 3). As $m^*\zeta$ increases, the corresponding distribution curve of η_M has a convex shape and reaches maximum value at the optimal $m^*\zeta$. It could be found that the reduced velocity range of power harvesting was primarily affected by the mass ratio rather than damping. In addition, setting the mass-damping coefficient as the variable to explore the VIV characteristics of a circular cylinder was studied [32].

In 2014, the effects of mass ratio, damping ratio, mass-damping parameter ($m^*\zeta$) and natural frequency of the circular cylinder on the energy harvesting efficiency were investigated [33] based on utilizing a numerical method of fluid-structure interaction. It should be noted that the energy harvesting was realized by a cylinder's transverse VIV. The results showed that increasing m^* was followed by an increase of maximum efficiency. It was accompanied however, by a reduction of the velocity range over which energy can be efficiently harvested. The results also showed that the maximum values of efficiency occurred at

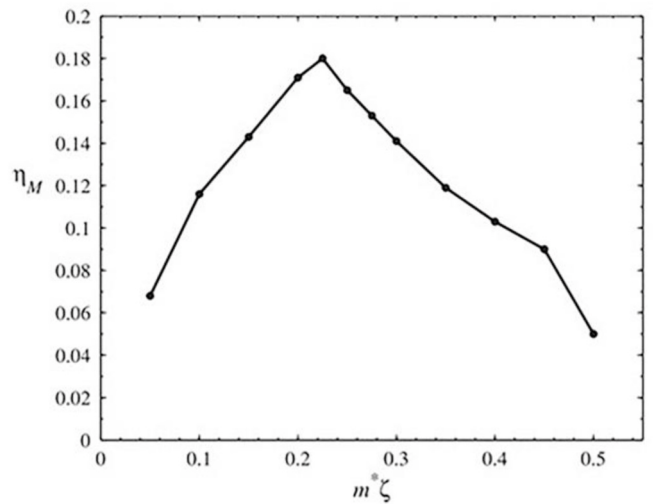


Fig. 3. The variation of the maximum energy efficiency with the mass-damping ($D = 20$ mm, $f_{n,water} = 2$ Hz) [10].

$m^*\zeta = 0.24$. With increasing of $f_{n,vac}$, realized by increasing K , the synchronization region shifted to higher velocity, and the velocity range of energy harvesting narrowed down. This was consistent with [19].

The impact of mass ratio m^* and spring stiffness K on the energy harvesting and power conversion efficiency was investigated [30] by conducting the experiments in the LTFSW channel of University of Michigan. The adjustment of spring stiffness and damping ratio was accomplished by an embedded computer-controlled of the second generation of the virtual spring-damping system (Vck) [28], as shown in Fig. 4. The difference between these two studies [30,33] is that the former also explores use of passive turbulence control by applying selective local roughness to the cylinder. That controls the gap between the VIV and galloping regions, thus, resulting in the Response Amplitude Operator (RAO) of the VIVACE Converter continuous and open-ended. In addition, in the VIV upper branch and galloping regions, harvested power increases when mass ratio m^* increases from 1.007 to 1.685. Results confirmed that the lowest achieved onset speed of VIV at which some power was harvested was 0.3946 m/s, which is much lower than that of turbines used in hydrokinetic energy harvesting. This research was further expanded in 2017 [34].

Since 2002 [35], it was thought that response and range of synchronization for VIV increase with decreasing m^* . This is correct for $K = 0\text{N/m}$ but the relation between range of synchronization and parameters (K, m^*, ζ) is more complex as explained in Ref. [29] based on derived explicit expressions.

2.4. Eigen-relation at the fluid-structure interface

In 2019, the research carried out consistent dimensional analysis of the governing equations of a one-degree of freedom FIO and revealed a first-order relation that has to hold for VIV and galloping to occur [29]. The “first-order relation” in this paper refers to that all the fluid-induced vibrations (including VIV and galloping) are related to their own natural

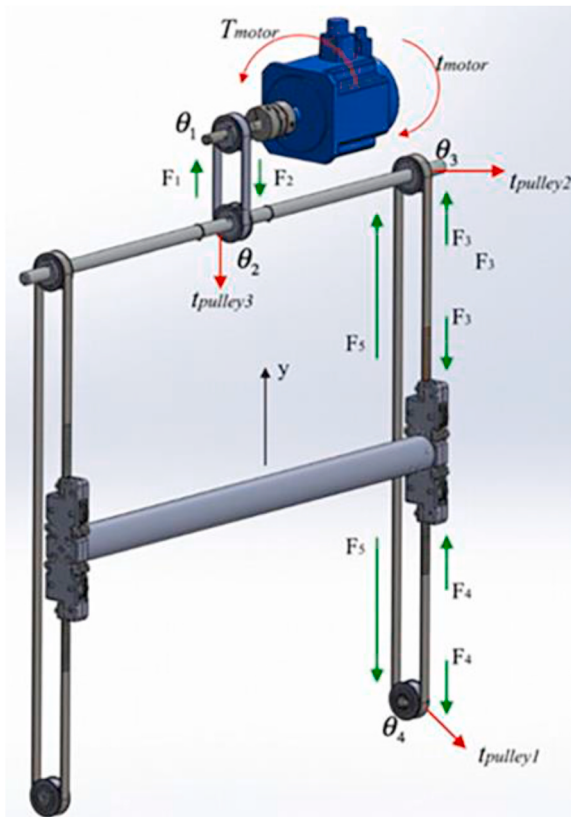


Fig. 4. Schematic of the Vck model in the MRELabs [28].

frequencies, to the Reynolds number. Detailed analysis can be found in reference [29]. Analogous to the wave dispersive equation, when the frequency of oscillation is selected the oscillator properties are defined by the eigen (characteristic) relation:

$$\frac{m_A}{m_{osc}} = \frac{C_A}{m^*} = \frac{1}{f^{*2} - 1} \quad (5)$$

Thus, the ratio of the added mass coefficient C_A to the mass ratio m^* is defined as a function only of the real Strouhal number f^* (Eq. (5)). The properties of the oscillator are independent of Reynolds number. Then the amplitude of oscillation is defined based on the energy transfer process, besides that, is a function of Re only. This was revealed by non-dimensionalizing the first order oscillator equation not by the stagnation pressure force as done traditionally since 1738 but by the spring force dictated by the fluid structure interaction. Following Eq. (5), explicit equations were derived for the first order forces, their coefficients and their phases. Agreement with 10-year data collected in the MRELabs was remarkable establishing the validity of the equations. Based on the derived relations, facts established by experiments on VIV and galloping for over 70 years and new important observations were readily explained including but not limited to: (1) Identifying the governing dimensionless parameters as the generic Strouhal number and the Reynolds number. (2) Defining the effects of mass-ratio, damping-ratio, and reduced velocity. (3) Clarifying important roles of Reynolds, Strouhal, and stagnation pressure in FIO. (4) Revealing the cause of expansion/contraction of the VIV synchronization range. (5) Explaining the change of slope in the oscillating frequency vs. corresponding slope of the Strouhal frequency for a stationary-cylinder in steady uniform flow. (6) Clarifying the notion of perpetual VIV. (7) Showing the impact of vortices for VIV and galloping. (8) Identifying the indirect and direct vortex effects.

In Subsection 2.3, the mass damping parameter is used as the dominant parameter of VIV. The mass-damping parameter was introduced in 1955 but it is a heuristic parameter; not a consistently derived one. In this Subsection 2.4, we limit our review to the effect of mass and spring constants which have a major impact on the range of synchronization, the real added mass as opposed to the theoretical in quiescent water, the slope of the frequency of oscillation, and f^* as the most important parameter rather than the heuristic mass-damping parameter $m^*\zeta$, and more.

Fig. 5-a shows the relationship between C_A and f^* by setting m^* (predicted by Eq. (5)) as a variable parameter. Increasing m^* in the range of 0.1–100, it can be observed that the variable curve pivots around the point ($C_A = 0; f^* = 1$), and the closer the mass ratio m^* is to 100, the closer the corresponding curve is to line $f^* = 1$ and the higher is the slope of the corresponding curve. This observation indicated that increasing the mass ratio is followed by a decrease of the VIV range projected on the f^* -axis, meaning that, for lower m^* , a small change in C_A (represents a small change for $f_{n,vac}$) will result in a significant expansion of the synchronization range of VIV. Fig. 5-a though represents a partial picture of the dependence of the synchronization range on m^* . Fig. 5-b reveals the rest of this dependence based on experimental data which match perfectly the theory. Specifically, as m^* decreases from 1.890 to 1.007, the synchronization region shifts to lower f^* , thus, compressing the synchronization range. This is the case because increasing m^* will decrease the natural frequency in vacuo $f_{n,vac}$, which represents the denominator of f^* . On the other hand the curves pivot around $f^* = 1$ (added mass is zero) expanding the range.

Fig. 6 shows comparison between the theoretical eigen-relation and experiments. It plots C_A/m^* vs. f^* for 20 combinations of m^* and K ($m^* = 1.007, 1.340, 1.685, 1.890; K = 400, 500, 600, 700, 800 \text{ N/m}$). Results confirmed that the lower m^* and higher K result in the higher $f_{n,vac}$ (Eq. (3)), which makes the VIV synchronization region shift toward to low f^* . Similarly, the high m^* and low K will push the synchronization region to the high f^* and low C_A/m^* . Additionally, for both the results of eigen-

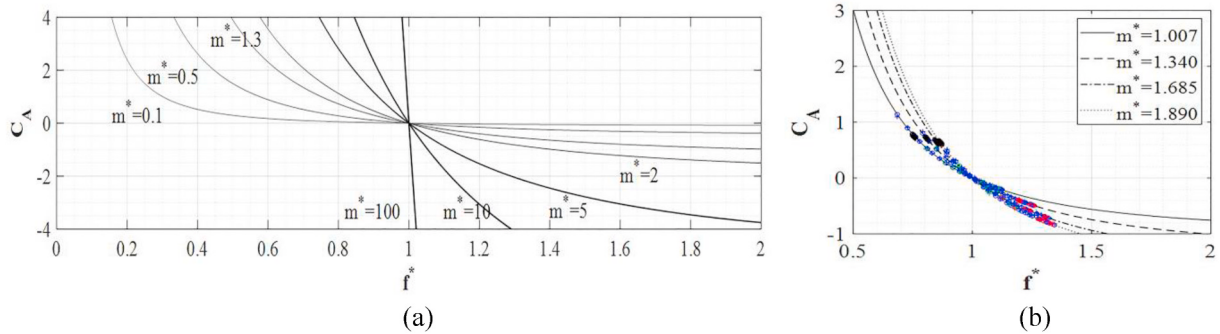


Fig. 5. The relationship between the C_A and f^* by setting m^* as a variable parameter: (a) $m^* = 0.1\text{--}100$. (b) $K = 400\text{N/m}$ [29].

relation (Eq. (5)) and experiments, decreasing K will broaden the VIV synchronization range. Fig. 6 also shows, for too large K or too small m^* , the VIV synchronization region will be shifted toward the left side of point ($f^* = 1$) and will not reach up to $f^* = 1$, indicating that the smaller synchronization region is generated. The critical mass-ratio was also analyzed [29] by comparing to experimental measurements for $K = 0\text{N/m}$ [35]. The conclusion was that the observation in Ref. [35] is valid but it is due to the low K value not to the low m^* value. The actual m^* effect is the opposite, suppressing the range of synchronization rather than expanding it. The actual critical coordinate point is for $C_A/m^* = -1$, $f^* = \infty$, moreover, the oscillating frequency follows the Strouhal frequency of vortex shedding of a stationary cylinder [29] because $K = 0\text{N/m}$ and there is no restoring force. Thus, the oscillations become forced by the shedding vortices with zero natural frequency in water.

Based on the above studies, the analysis of the linear oscillator in this section is of pivotal importance for the exploration of nonlinear oscillators in Sections 3–8 because the linear oscillator is the reference point for benchmarking.

3. Oscillator cylinders with noncircular cross-section

Flow past a single smooth circular cylinder does not induce galloping instability. Geometric asymmetry or upstream flow asymmetry may trigger galloping. So it is reasonable to explore different shapes to induce galloping and extend the energy harnessing range past VIV into galloping. Change in the geometry of a cylinder-oscillator placed in an incoming flow causes changes in the location of the stagnation point, boundary layer, flow separation, and shear layers and other flow field characteristics resulting in change of the response phenomenon. Thus, the onset and termination of VIV may be affected, or galloping may occur overtaking VIV completely. Such changes affect hydrokinetic energy harnessing and need to be reviewed systematically. Subsection 3.1 covers oscillators with smooth circular cylinders and Subsection 3.2 covers oscillators with non-circular cylinders.

3.1. Smooth circular cylinder

Circular cylindrical structures are applied widely in all engineering disciplines: offshore, marine, civil, aeronautics, nuclear, mechanical, etc. They are easy to fabricate, are equally strong in all directions of loading, and are not prone to galloping due to their rotational symmetry. Accordingly, they have been studied extensively for VIV suppression. Being simple to fabricate, a circular cylinder is regarded as the primary body in a Current Energy Converter, easy to excite in VIV and harvest hydrokinetic energy. In energy harvesting, the oscillating amplitude and the synchronization range are considered as two vital elements [29]. The latter makes CECs more robust to changes of the in-flow velocity. The VIV synchronization region initiates as vortex shedding frequency approaches from below the natural frequency of the oscillator in quiescent water [29]. Results show that the wider is the synchronization

range achieved, the better is the performance of the CEC [29]. Up to now, many scholars have used circular cylinders in CEC oscillators to utilize the VIV characteristics of wide range of high amplitude-response favoring power harvesting, by reasonably changing the mass ratio, damping ratio, Reynolds number, external electrical load resistance R , or other parameters for the experimental or model equipment [6]. According to the principle of power extraction, energy-harvesting devices can be divided into these two categories: piezoelectric and electromagnetic [36–38].

In recent years, based on [39], many scholars explored and extensively analyzed the power acquisition characteristic of piezoelectric ALT energy-converter [40–46]. Referring to Fig. 7, under the action of incoming flow, a rigid cylinder is excited to produce the transverse VIV, which induces a deformation of piezoelectric material on the cantilever beam, resulting in the generation of electricity [36].

In 2012, some scholars harvested energy from the transverse VIV (produced by the lift force) of a rigid cylinder by adding a piezoelectric device, which can convert VIV mechanical energy to electrical energy [20]. Based on [39], a velocity term was introduced to couple the lift force to the oscillatory motion. The lift force model was a modified van der Pol equation. It should be noted that, following the recent derivation of the eigen-relation at the fluid-structure interface for VIV and galloping and the related force expressions, modeling first order modeling is available [29]. To determine the coupling effect between the transverse oscillation and the voltage harvested, the coupling model was developed using the Gauss Flux Theorem. Results confirmed that increasing the load resistance causes a marked increase of the flow velocity required to initiate the VIV synchronization region. The results showed that using nonlinear analysis, the hysteresis phenomenon (which was reflected in a rapid decline of the harvested power) can be found in some load resistance cases.

Following [20], a piezoelectric energy harvester including a transverse VIV circular oscillator with length $L_{en} = 203\text{ mm}$ was numerically investigated [40]. The difference is that the velocity term was replaced by the base acceleration term. Also, a nonlinear distributed-parameter model, which includes a reduced-order model, was realized by the Galerkin method. The emphasis of this nonlinear analysis for power harvesting was on the incoming wind velocity, load resistance, and the base acceleration. The results showed that, as the incoming wind velocity changes in the range of synchronization, the power harvesting develops an obvious increment compared with that of the pre- and post-synchronization regime. The results also showed that increasing base acceleration is accompanied by a weakening phenomenon for the effect of the VIV.

In 2014, using the same numerical method and same physical values of test-parameters as [40], a further investigation was conducted to analyze the performance of power harvesting and synchronization region with parameters: electric load resistance, length of the piezoelectric sheet, velocity of incoming flow, and the oscillating mass of the circular cylinder CEC with length $L_{en} = 203\text{ mm}$ [41]. It should be pointed out

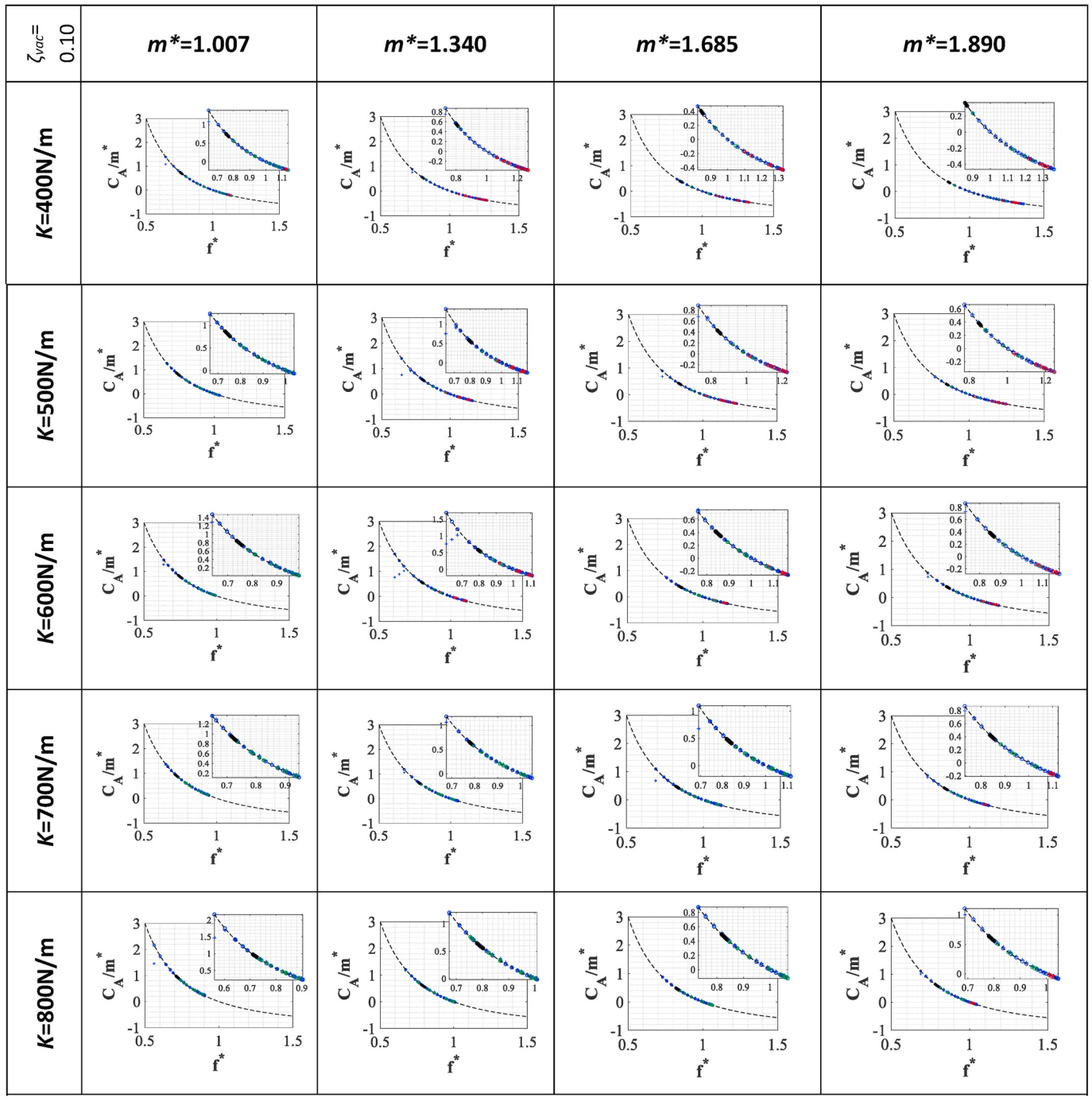


Fig. 6. Relationship between real C_A/m^* and f^* for different combinations of m^* and K : (a) — Theory expressed by eq. (5). (b) oooo Reconstructed based on theory and measured f^* . (c) +++++ Measured experimentally [29] (Cylinder's diameter of $D = 88.9$ mm, total damping ratio in vacuo $\zeta_{vac}=0.06$).

that only the appropriate selection of the above four influencing parameters improved the performance of this VIV energy harvester, while all other admissible solutions resulted in low efficiency. Moreover, the authors demonstrated how the Galerkin method using the five-mode approximation is introduced to this nonlinear oscillator research. Additionally, the maximum output power obtained by experiment [42] was 0.1 mW when the incoming flow velocity was equal to 1.192 m/s.

Relative research team also investigated piezoelectric energy harvesting for a cylindrical oscillator by employing a numerical simulation method with a parallel computational fluid dynamics (CFD) code [43]. The mass ratio, spring stiffness, damping ratio, and diameter of the cylinder were selected as 149.1, 579 N/m, 0.0012 and 1.6 mm,

respectively. It should be emphasized that the authors analyzed the effects of R and Re on the vibration displacement, output voltage, and harvested power. Results confirm that the maximum power is 10 μW at $Re \sim 100,000$ when $R = 500$ k Ω . It was shown that increasing R is followed by an increase of energy harvesting in the wider synchronization region. In all selected Re , the output voltage increases as the R increases, however, the increment rate goes down eventually. A similar variation tendency was observed in Ref. [44]. In the synchronization region, power harvesting was obviously higher than that in the regions of pre- and post-synchronization. The optimal load resistance used to obtain the maximum harvested power was about 104 k Ω . As expected, the optimum value of R results in reduced displacement as R introduces added

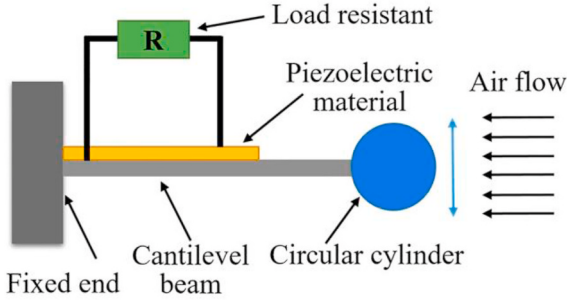


Fig. 7. Schematic of piezoelectric energy harvester.

damping for energy harnessing.

Fig. 8 shows a vortex-induced piezoelectric energy harvester (VIPEH) [45], which can be used to convert the incoming flow energy into electric energy. Therein, VIPEH in the form of a cantilever beam consist of a piezoelectric ceramic transducer (PZT) and a circular cylinder with $L_{en} = 60$ mm. Under the different combinations of the cylinder diameter D and mass M (i.e.: configuration I: $D = 20$ mm and $M = 21$ g; configuration II: $D = 20$ mm and $M = 54$ g; configuration III: $D = 12.8$ mm and $M = 21$ g), the variations of output power with the load resistance R and flow velocity U were analyzed. The results showed that, in each of the three combinations, the optimal value of R was around 100–150 k Ω , which can maximize the output power. Selecting an optimal resistance $R = 150$ k Ω as a fixed value and using the water velocity as a parameter, it was shown that changing the mode from Configuration III to Configuration I, the maximum output power increased and the corresponding optimal velocity shifted towards higher values. The maximum harvested power for VIPEH was 84.49 μ W at $U = 0.35$ m/s.

Different from the studies of VIV piezoelectric energy harvesters above, a novel method by changing the cylindrical installation with a cantilever beam was investigated experimentally [46]. Fig. 9 shows the placement orientation (including the bottom, top, horizontal, vertical) of the circular oscillators, of course, shows the relative position between the cylinder orientation and the incoming wind velocity. Four oscillating cylinders all have the length of 120 mm and diameter of 30 mm. The way of installation of the cantilever beam can notably affect the synchronization region, output voltage, and harvested power. Fig. 10 shows, in the vertical position (Case 4), it can convert greater power

(around 170 μ W at $U = 3.6$ m/s) and produce wider synchronization region (2.2–4.4 m/s) than that of the other three cases owing to its high natural frequency (12.2Hz) and low damping ratio (0.0109) based on a free vibration test. Furthermore, the corresponding velocities of highest power harvesting are diverse for these four cases, especially for the fourth case. To obtain a better energy output, the load resistance should also be considered besides the installation way of oscillator. There are two obvious reasons - both hydrodynamic - why Case 4 is a better CEC than the other three cases: (a) Only in Case 4 the entire cylinder length oscillates with the same amplitude A providing maximum oscillation and thus converting maximum hydrodynamic energy to mechanical in the oscillator. The local amplitude of oscillation over diameter ratio (A/D) remains the same resulting in similar wake patterns and vortex shedding along the cylinder. (b) In the other three Cases 1–3, A/D may be very low at the cylinder base resulting in inertia dominated excitation with no fully developed vortices. As the oscillating amplitude increases towards the tip of the oscillator, A/D may exceed the maximum amplitude of VIV synchronization in the specific flow regime (most likely TrSL2) [29]. This results in termination of lock-in and partial length of the cylinder providing flow resistance rather than supporting the VIV excitation force. VIV in shear flows has been studied in Ref. [47].

As can be observed, the energy conversion can be realized by introducing a piezoelectric or piezo-magnet-elastic transducer. Nevertheless, the following studies are focused on using an electromagnetic device to convert the hydrokinetic power to the required electrical power.

Firstly, for an oscillator with spring stiffness and damping (as shown in Fig. 11), in order to better describe the effect of structural parameters (i.e., spring stiffness, damping ratio, mass ratio and so on) on the harnessed power $P_{harness}$ and power efficiency $\eta_{harness}$, the following mathematical formulas of oscillating oscillator are introduced and analyzed:

Setting the flow direction and cylinder's vibration direction as the x-direction and y-direction, respectively, the motion equation of an oscillating cylinder is:

$$m_{osc}\ddot{y} + c_{total}\dot{y} + Ky = F_{Fluid} \quad (6)$$

where m_{osc} consists of the oscillating mass of the structure; K represents the spring stiffness acting on the oscillator; F_{Fluid} represents the lift force which is stimulated by the incoming flow; c_{total} is the total damping coefficient, which can be expressed as:

$$c_{total} = c_{structure} + c_{harness} \quad (7)$$

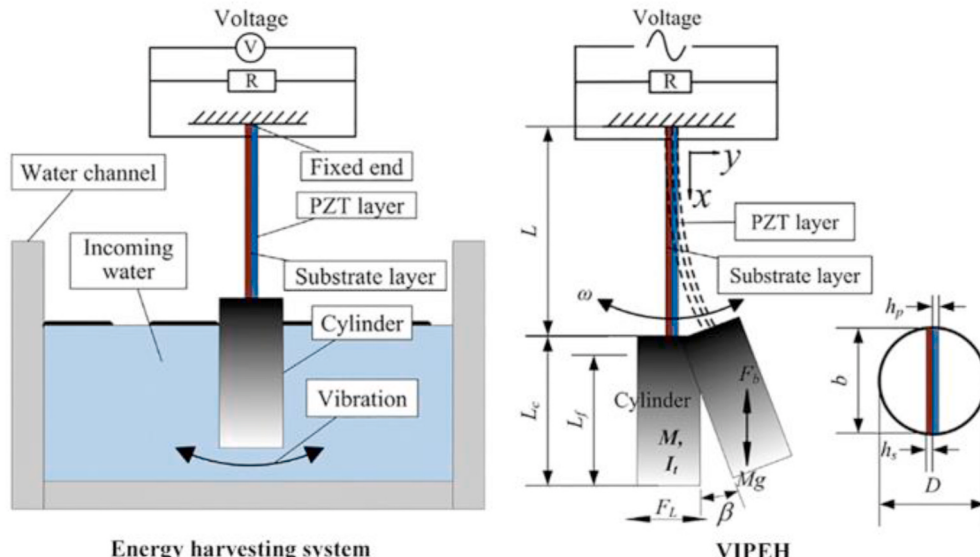


Fig. 8. Schematic of piezoelectric energy harvesting device [45].

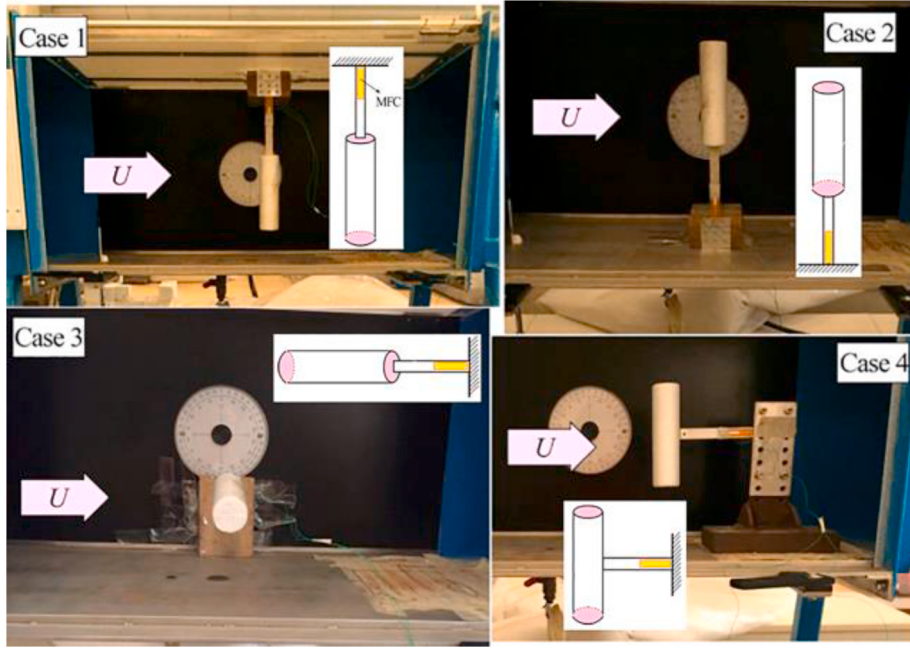


Fig. 9. Different configurations for VIV energy harvester [46] ($L_{en} = 120$ mm; $D = 30$ mm).

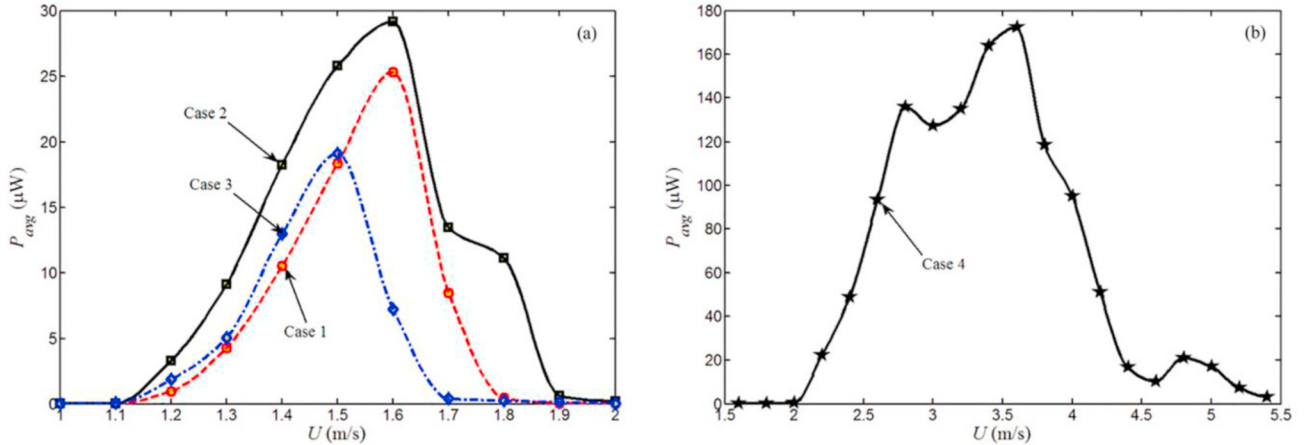


Fig. 10. Power harvesting by four different installation configurations [46] ($L_{en} = 120$ mm; $D = 30$ mm).

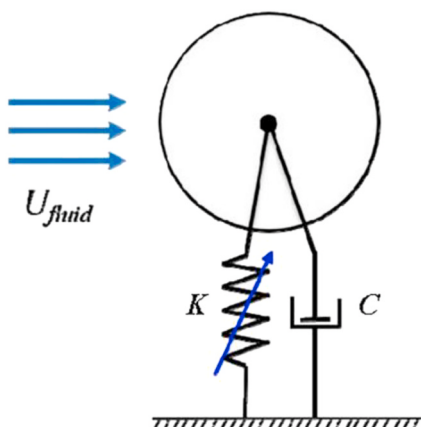


Fig. 11. Oscillator configuration.

The structural damping $c_{structure}$ represents the energy lost due to friction during the oscillation of the device. Additionally, it should be pointed out that adding harnessing damping coefficient $c_{harness}$ is implemented by the V_{ck} system [28]. In more detail, $\zeta_{structure}$ and $\zeta_{harness}$ can be respectively expressed as:

$$\zeta_{structure} = \frac{c_{structure}}{2\sqrt{(m_{osc} + m_a)K}} \quad (8)$$

$$\zeta_{harness} = \frac{c_{harness}}{2\sqrt{(m_{osc} + m_a)K}} \quad (9)$$

where m_a is the added mass. The harnessed power is:

$$P_{harness} = 8\pi^3(m_{osc} + m_a)\zeta_{harness}(A f_{osc})^2 f_{n,water} \quad (10)$$

where A is the oscillating amplitude, and f_{osc} represents the oscillating frequency. The power of flow fluid can be expressed as:

$$P_{Fluid} = \frac{1}{2}\rho U^3(2A_{max} + D)L_{en} \quad (11)$$

where A_{max} shows the maximum amplitude, ρ represents the fluid-density, L_{en} is the length of the cylinder. The Betz Limit [48] represents the theoretical maximum value of power that can be extracted from the flowing fluid. Therefore, the converter efficiency can be defined as:

$$\eta_{harness} (\%) = \frac{P_{harness}}{P_{Fluid} \times \text{BetzLimit}} \times 100\% \quad (12)$$

Electromagnetic methods for harvesting energy from oscillatory motion have been known since Nikolai Tesla's invention in the early 1900's. Extended work in Sweden was done to introduce energy harvesting from waves using the motion of buoys [49]. Recently, a similar electromagnetic method has been introduced to harvest electrical energy from VIV by numerically using a spectral-element solver [50]. In Fig. 12, the principle of energy harvesting can be clearly shown. A circular cylinder with a magnet fixed on its axis produces a transverse motion under the action of the incoming flow, inducing the electricity harvested in the coil. The motion path of the cylindrical oscillator is collinear with the axis of the coil, and a damping repulsive force was induced by the electricity in the coil. The authors investigated the effect of electromagnetic damping ratio (ζ_m), radius (a), and length (L_c) of the coil and the mass ratio (m^*) of cylinder on the power harvesting. The results showed that the maximum electric power per length of cylinder ($P_{ele} = 0.13\text{W/m}$ at $Re = 150$ for $a = 0.6$, $L_c = 0.6$, $m^* = 2$) can be observed at an optimal damping ratio $\zeta_m = 0.14$. Additionally, increasing the values of a or L_c induces an increase in the optimal damping ratio.

In 2016, an experiment was conducted to analyzed the mechanical efficiency (η_{mech}) of the VIV-based Energy Converter (VIVEC) under the impact of mass ratio m^* , damping ratio ζ , and Re [51]. As shown in

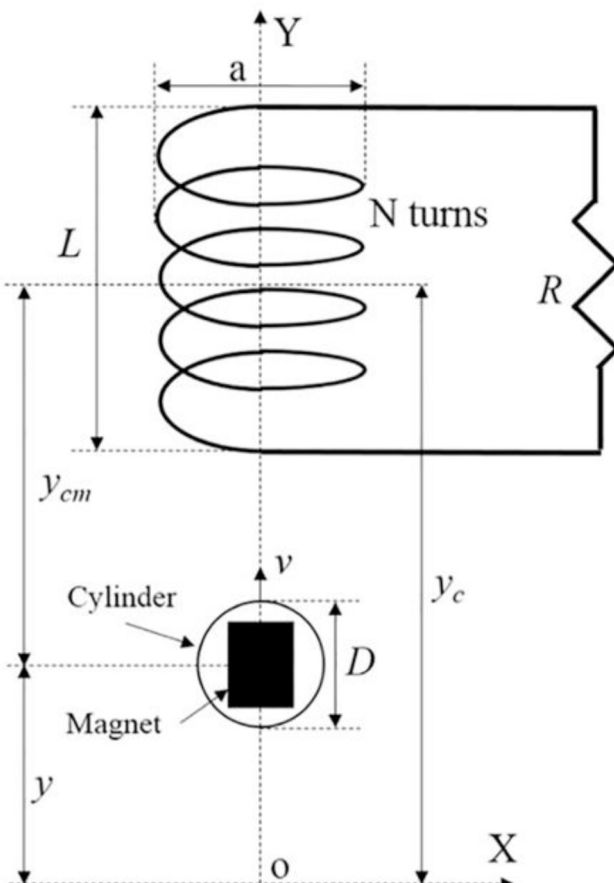


Fig. 12. Schematic of cylinder-magnet assembly [50].

Fig. 13, the energy harvesting was realized by the electromagnetic principle. The maximum value of η_{mech} is around 90%; and when considering the time dependence, the average value is around 50%. It can be found that when the mass-damping coefficient $m^*\zeta$ is 0.05, 0.097, and 0.166, the mechanical efficiency of VIVEC is 52%, 39%, and 30%, respectively.

In 2018, Ref. [52] explored the VIV power harvesting of a cylinder by introducing an eddy-current-based damping mechanism. The cylinder has the mass ratio of 3.0, diameter of 30 mm and length of 615 mm. The principle of the power extraction is that, lift force stimulated by the incoming flow will force the oscillator into the transverse VIV phenomenon. That causes the attached magnet to move parallel to the copper plate, which results in the eddy currents created in the copper plate. In Fig. 14, there is a fixed distance (G) between the magnet and plate. More details on the design and operation of this experimental apparatus can be found in Ref. [53]. It is necessary to point out that the pivotal research parameter is damping, which comes from the reactive force of the magnetic field of the plate according to Lenz's law. As expected, with the increasing of damping, the width of the synchronization region decreases. Moreover, as damping increases, the maximum average extracted power (P_m)_{max} has an upward trend followed by a downward trend. For a given flow velocity, small increase in damping harnesses more fluid-kinetic energy while excessive damping suppresses FIOs. The flow velocity is the most important parameter in hydrokinetic power harnessing as fluid power is proportional to velocity cube.

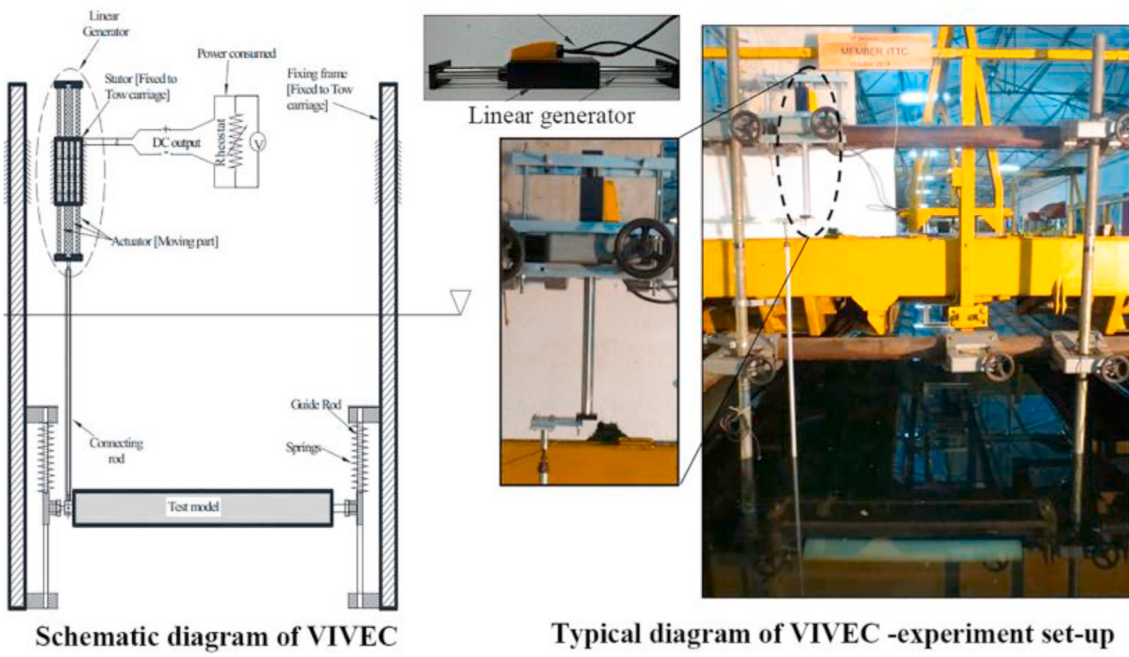
3.2. Non-circular cylinder oscillators

Compared to the circular cylinder, the non-circular cylinder can induce a more complex flow-induced vibration. In low-velocity flows, the lift due to the alternating vortex wake cannot cause the bluff cylindrical body to oscillate/vibrate. However, when flow velocity reaches up to a critical value, shear layers induce instability making the damping in the transverse direction negative and then, resulting in galloping. The vibration direction of the galloping is also perpendicular to the flow. Compared to VIV, galloping has the characteristics of large amplitude and low frequency, does not induce the frequency lock-in phenomenon, and does not depend on the form of the vortex wake [21]. As the flow velocity increases, galloping becomes more intense and destructive. Galloping is stimulated by the geometric asymmetry of a non-circular cylinder [54]. It may also be induced by upstream flow asymmetry; e.g. that encountered by a body in the wake of another body, stationary or moving. The relative onset of VIV vs. galloping is still under investigation in Ref. [55]. Specifically, large-size turbulence stimulation initiates galloping much earlier but not sooner than VIV. The earliest onset of galloping was achieved simultaneously with VIV, which initiates near the natural oscillation frequency of the cylinder in quiescent water. That is to say, the hydrodynamic mechanisms inducing the two FIO phenomena coexist. Typically, VIV achieves higher efficiency and galloping achieves higher power harvesting.

Most of the research conducted focuses on the details of the shape, the angle of edges, and the impact of shapes on the harnessed power and efficiency of an ALT current energy converter. Circular-cylinder oscillators are not prone to galloping like prismatic or non-circular oscillators. In the latter, typically, VIV initiates at much lower velocities than galloping. In previous research, it was concluded that non-circular cylinders and prisms can reach galloping where amplitude response is not self-limited as in VIV [30,56]. Based on these reasons, a considerable number of scholars have focused on improving the power harvesting and its efficiency by using prismatic oscillators with square, rectangular, or triangular cross-sections.

3.2.1. Square and rectangular shapes

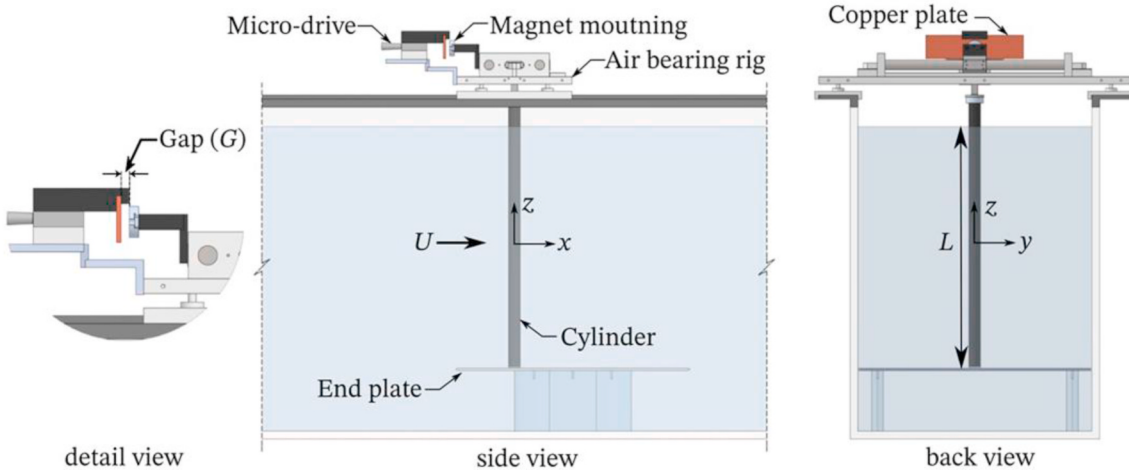
Several research teams analyzed the effect of external load resistance R or Re (which represents the flow velocities) on the power harnessed and efficiency of square oscillator [57–60]. They mainly used



Schematic diagram of VIVEC

Typical diagram of VIVEC -experiment set-up

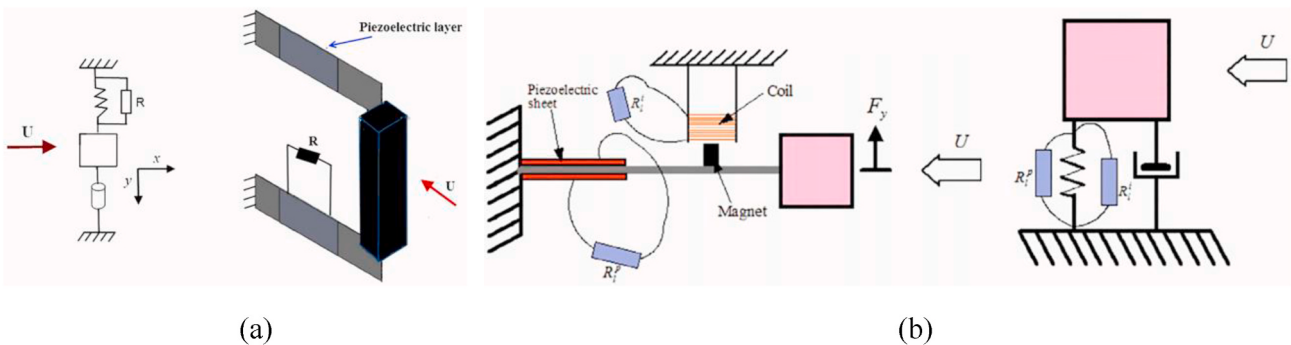
Fig. 13. Schematic of elastically mounted cylindrical arrangement [51].

Fig. 14. Schematic diagram of the VIV experimental set-up for hydrokinetic energy harnessing [52] ($L_{en} = 615$ mm; $D = 30$ mm; $m^* = 3.0$).

piezoelectric or electromagnetic transducers to produce power from steady flow. These four papers are reviewed next.

In 2012, a numerical method was adopted to investigate energy

harvesting using the transverse galloping of a square-prism oscillator by choosing the appropriate values of Re and electric load resistance [57]. A quasi-steady approximation was utilized to simulate the aerodynamic

Fig. 15. Schematic of flow-kinetic energy harvester under transverse galloping in Refs. [57,60]: (a) piezo-aeroelastic ($D = 15$ mm; $m = 0.44$ kg). (b) hybrid piezoelectric-inductive ($D = 30$ mm; $m = 0.44$ kg).

force. Further, the piezoelectric transducer was added to obtain energy from the mechanical oscillation, as shown in Fig. 15-a. Moreover, a case of forced oscillations with nonlinear force, which consists of the cubic term and higher order terms such as fifth and seventh order terms, were applied in their research. The results showed that the energy harvested depends on both the Reynolds number Re and the electric load resistant R . Higher Re results in higher harvested power. In the TrSL3 (Transition in Shear Layer) flow regime, this is expected according to the VIV measurements by Bernitsas et al. (2006), where the amplitude response is enhanced with increasing Reynolds in the VIV upper branch [5]. Further, the harvested power rises initially and then falls with increasing electric load resistance, particularly at high Re , corresponding to incoming flow velocity of 2 m/s–15 m/s (side length $D = 15$ mm; mass of square oscillator $m = 0.44$ kg). The optimal power harvesting per unit length occurs when the value of electric load resistance is around 100 k Ω . The corresponding incoming wind velocity is about 15 m/s. This is also expected as too low damping results in low energy harnessing and too high damping suppresses FIO resulting again in low energy output. The optimal power would be in between those two extremes.

Two similar cases [58,59] were investigated to realize power harvesting from galloping of an oscillator with different cross-sectional shapes. Observations for square cross-section were similar to those in Ref. [57].

As shown in Fig. 15-b, the team of Javed built and tested a hybrid piezoelectric and electromagnetic energy harvester [60]. The oscillator uses a square prism (side length of $D = 30$ mm and mass of $m = 0.44$ kg), which can undergo transverse galloping. The authors applied the nonlinear quasi-steady approximation to simulate aerodynamic force as modeled in Ref. [61]. Authors analyzed the impact of the external load resistance for the initial galloping velocity and the optimal power harvesting of the hybrid energy harvester. They concluded that the output power of a piezoelectric transducer can reach two peak values corresponding to two optimal external load resistance values. Nevertheless, the hybrid energy harvester, which is affected by the shunt damping of the additional resistance, has a lower level of energy harvesting and a higher value of initial galloping velocity than that of the classical piezoelectric or electromagnetic energy harvesters. At incoming flow of $U = 15$ m/s, the maximum power per unit length of cylinder for a hybrid harvester was 0.785W.

In [62], the electromagnetic transducer was utilized to harness the energy based on the transverse galloping of a square oscillator. This research has added a nonlinear model (which includes a distributed parameter) to produce the aerodynamics of the square-prism oscillator. The external parameters (i.e.: external load resistance, coil internal

resistance, the position of the magnet and electromagnetic coupling coefficient) have been selected to investigate the initial galloping speed and the energy harvesting. The results showed, energy harvesting increases as increase of the distance between the fixed wall and the selected magnet and the electromagnetic coupling coefficient. However, the harvested energy showed the downtown trend with the increasing of the coil internal resistance. The maximum energy harvesting has a relationship with external load resistance that changes with the coil internal resistance, the position of the magnet, and the electromagnetic coupling coefficient.

The impact of mass ratio or damping ratio for power harnessing and efficiency of a square oscillator was investigated [63,64].

The team of Zhang numerically investigated the electromagnetic energy harvesting and its efficiency for a square cylinder (Fig. 16-a) by changing the mass ratio m^* from 1.0 to 4.0 and selecting the damping ratio ζ from 0.0158 to 0.800 [63]. The side length and spring stiffness of square are, respectively, selected as $D = 90$ mm and $K = 1,063$ N/m. The numerical flow velocity is 0.2–3.0 m/s ($15,500 < Re < 232,000$). Moreover, the numerical method was verified to be correct by comparing results to previous experimental results and was used to simulate the FIV response. With the damping ratio increases in the range of $\zeta_{total} \leq 0.6$, the oscillation amplitude decreases, nevertheless, the power harvesting and its efficiency increases. The harnessed power reached up to 143W when the $\zeta_{total} = 0.6$. Results indicated that the initial galloping velocity decreased as mass ratio increased in the range of $1.0 < m^* < 4.0$, resulting in a narrow velocity range for VIV. Results confirmed that the oscillation frequency and power harvesting decreased as the mass ratio increased, showing the similar conclusions as [64].

In recent years, as shown in Fig. 16-b, many scholars used rectangular prismatic oscillators as a variation of a square prism to explore the possibility of increasing the harvested energy.

In 2018, a rectangular cylinder was tested to analyze the influence of the cross-sectional aspect ratio (σ) for hydrokinetic power harvesting or corresponding efficiency [65] using the same numerical electromagnetic simulation model and method as [63]. The aspect ratio can be expressed as:

$$\sigma = \frac{W}{H} \quad (13)$$

As shown in Fig. 16-b, where W is the width in the streamwise direction; H is the height in the vertical direction. The length, mass ratio, total damping coefficient, spring stiffness of oscillator are $L_{en} = 1,000$ mm, $m^* = 1.725$; $c_{total} = 30$ N/m and $K = 1,063$ N/m, respectively. The

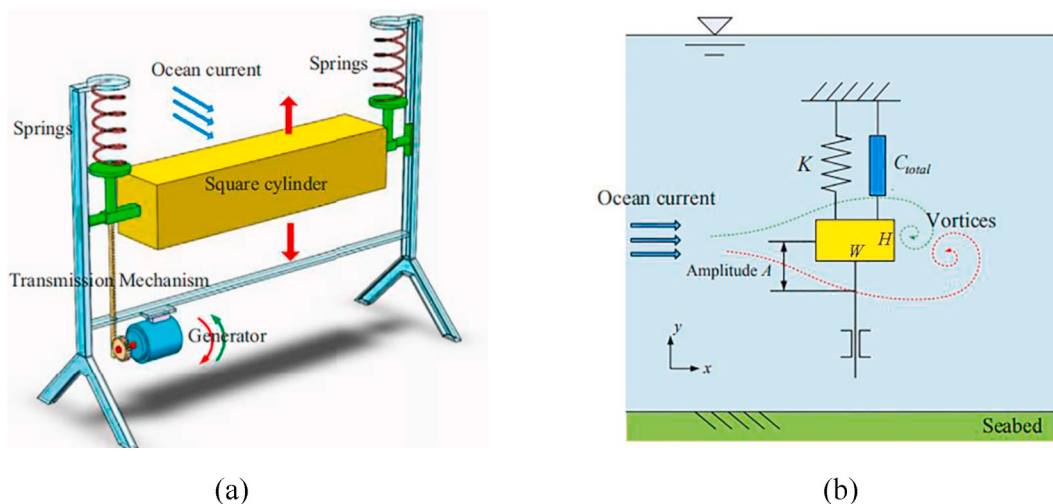


Fig. 16. Schematic of hydrokinetic energy harvester in Refs. [63,65]: (a) Square oscillator ($D = 90$ mm; $m^* = 1.0\text{--}4.0$; $K = 1,063$ N/m; $\zeta = 0.0158\text{--}0.8$). (b) Rectangular oscillator ($L_{en} = 1,000$ mm; $m^* = 1.725$; $c_{total} = 30$ N/m; area of cross-section $S_{cs} = 7,900$ mm 2).

aspect ratio σ of the rectangular cross-section varied from 1/6 to 2.0. The incoming water velocity varied from 0.1 to 2.5 m/s ($7500 < Re < 187,500$). The paper concluded that higher aspect ratio results in lower power harvesting and efficiency. An important conclusion is that, FIO (including VIV and galloping) disappeared completely past aspect ratio of $\sigma = 2.0$. Fig. 17-a shows that the optimal aspect ratio is 1/6 ($W = 0.036293$ m; $H = 0.217758$ m; area of cross-section $S_{cs} = 7,900 \text{ mm}^2$), which produced the maximum harvested power ($P_{max} = 315.9 \text{ W}$ at $U = 2.5 \text{ m/s}$). Additionally, the curve has a rising tendency with increasing flow velocity. Fig. 17-b shows, the maximum efficiency (reaching up to 15.5%) occurs at the aspect ratio $\sigma = 1/4$ ($W = 0.044450$ m; $H = 0.177800$ m).

Another similar research, which changed the aspect ratio of the rectangular oscillator in the range of $0.2 \leq \sigma \leq 0.5$ (as expressed in Eq. (13)), was experimentally investigated in Ref. [66]. This research analyzed the transverse FIV responses as $2 \leq U^* \leq 16$. The reduced velocity U^* can be expressed as:

$$U^* = \frac{U}{f_{n,water} D} \quad (14)$$

Authors used the oscillating response such as frequency or amplitude to indirectly analyze the energy harvesting of the transverse oscillation of the rectangular cylinder. Results confirmed, as aspect ratio increases, the initial reduced velocity of VIV synchronization region increases, nevertheless, the normalized amplitude decreases. Particularly, in the region of galloping, the amplitude curve exhibits a linear rise with increase in the reduced velocity in the range $2.0 \leq U^* \leq 4.0$. Nevertheless, when $U^* = 5.0$, the amplitude reached zero in the galloping region.

The above articles mainly focused on the effects of mass ratio, damping ratio, and cross-sectional aspect ratio of the rectangular oscillators. In the following, more parameters were considered. In particular, the orientation angle (θ_0) of the square or rectangular oscillator with respect to the flow direction was added to investigate the electromagnetic energy harvesting from the transverse galloping (Fig. 18) [67]. Following preliminary testing, a square section with orientation $\theta_0 = 0^\circ$ and 10° and a 2/3 rectangular section (with the long side in the flow direction) with orientation $\theta_0 = 2^\circ$ were selected for further testing. Results confirmed that, for the square section, the case of $\theta_0 = 10^\circ$ results in higher power efficiency than that of the $\theta_0 = 0^\circ$ due to lower onset velocity of the transverse galloping. The power harvesting efficiency was small, with its maximum value reaching only 0.02% in the case of rectangular cross-section at $\theta_0 = 2^\circ$. It is a novel approach to realize

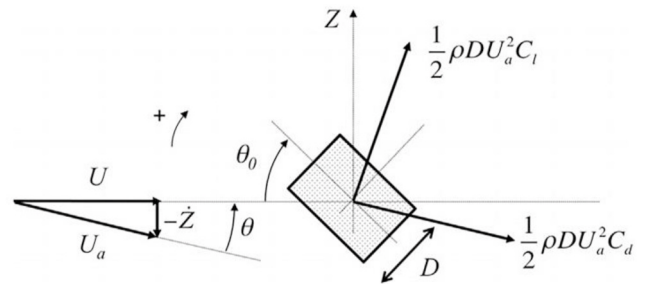


Fig. 18. Schematic of transverse galloping for a square cylinder with an orientation angle [67].

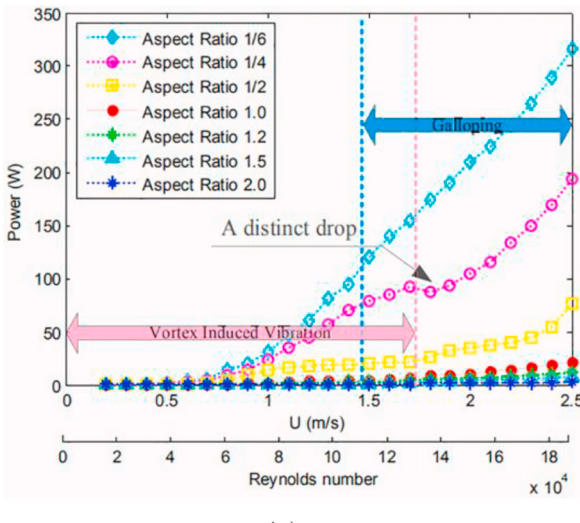
power harvesting from transverse galloping of a square prismatic oscillator and should further investigated by selecting the appropriate parameters such as load resistance or orientation angle of the cross-section. Prior to researching in that direction though, it may be advisable to question the use of one-sided biased asymmetry. It obviously results in uneven transverse force from the two sides of the prism. Thus, the shear layer on the side that drives the instability will be different in the two half-cycles of a full oscillation.

Additionally, another study also used square and rectangular prismatic oscillators to investigate the FIV responses [68]. Authors tested the square cross-section with orientation angle of $\theta_0 = 0^\circ$, 22.5° , and 45° , and the rectangle with orientation of $\theta_0 = 0^\circ$, 45° , and 90° . The amplitude and frequency responses of the different angles of the oscillator were analyzed. The results showed that the different angles have different FIV responses of the square or rectangular oscillators.

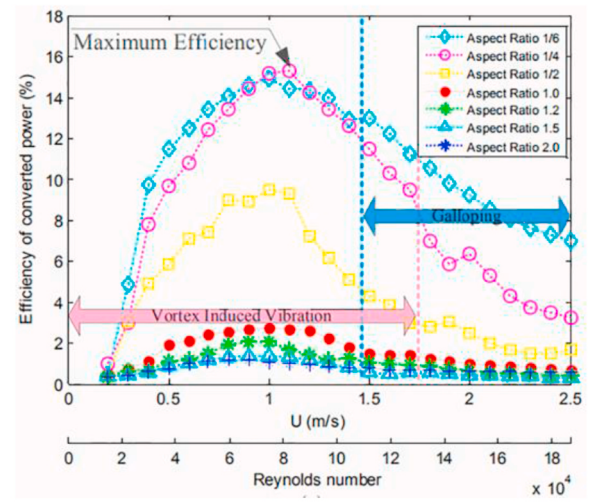
In addition, many scholars performed various researches to analyze the vibration mechanism (VIV and galloping) of the square and rectangular oscillators and flow state around them. However, power harvesting, especially changing the mass ratio, cross-sectional aspect ratio or the orientation angle of the oscillators, has not been studied widely. Therefore, future research focus on these important parameters to investigate better performance of power harnessing and its efficiency of square and rectangular prismatic oscillators.

3.2.2. Trilateral shape

The number of publications on triangular-prism oscillators for power harvesting is small compared to papers on square-prism oscillators. Nevertheless, as investigated by a considerable number of scholars,



(a)



(b)

Fig. 17. Power harvested and efficiency vs. water velocity and Re for various values of the cross-sectional aspect ratio: (a) Power harvested. (b) Power efficiency [65] ($L_{en} = 1,000 \text{ mm}$; $m^* = 1.725$; $c_{total} = 30$; $K = 1,063 \text{ N/m}$; area of cross-section $S_{cs} = 7,900 \text{ mm}^2$).

triangular prisms have been demonstrated to develop strong FIV and have a wider range of flow speed for power harnessing. Particularly, in the galloping region, a triangular-prism oscillator achieves larger amplitude, and its value will increase when incoming flow velocity increases. Therefore, a triangular prism can be regarded as an effective oscillator to realize energy harvesting.

Firstly, the effect of electrical load resistance or incoming flow velocity on the energy harvesting and harvested voltage of an equilateral triangular prismatic oscillator was explored in Refs. [69,70]. Authors mainly used the piezoelectric transducers to produce power. Their papers are reviewed next.

As shown in Fig. 19, the research team studied harvesting electric power from transverse galloping by a prototype device with a triangular oscillator (length of $L_{en} = 251$ mm; side length of $D = 40$ mm) at $0 < U < 14$ mph ($0 < U < 6.26$ m/s) [69]. The prototype has the same compositions as the piezo-aeroelastic energy harvester [57]. The authors tested the output power of the prototype by its controlling electrical load resistance and incoming wind velocity. In Fig. 20, the output power showed a rise initially followed by a drop with increasing of load resistance. The output power reached up to 53 mW as the load resistance reached 37 k Ω , and increased as the wind velocity increased from 8.2 to 11.6 mph.

Being similar to the research on square oscillator [57], another study used a piezoelectric energy converter to convert the mechanical energy of an equilateral triangular prism's transverse galloping to electric energy (Fig. 21) [70]. The effectiveness of the energy harvester was validated through a coupled nonlinear distributed-parameter model with a linear or nonlinear torsional spring. It was found that the analytical results of the nonlinear spring case matched well with previous experimental data. Their nonlinear analysis focused on the effects of incoming airflow velocity or electrical load resistance for the variation tendency of oscillation displacement, output power and voltage harvesting. The values of those three outputs increased with increasing airflow velocity. Increasing the load resistance was accompanied by the increase for voltage; however, it was followed by a decrease of the corresponding voltage increment. Furthermore, the optimal load resistance, leading to maximum output power, was 37 k Ω , which is directly linked to the harnessed damping of the converter. The authors observed that the optimal resistance (i.e., damping ratio) develops when the minimum oscillation displacement is achieved prior to full suppression due to high damping.

Refs. [58,59] replaced the equilateral triangular section with an isosceles triangle with two different base angles, namely $\delta = 30^\circ$ and 53° . It can be observed that the function of changing the value of

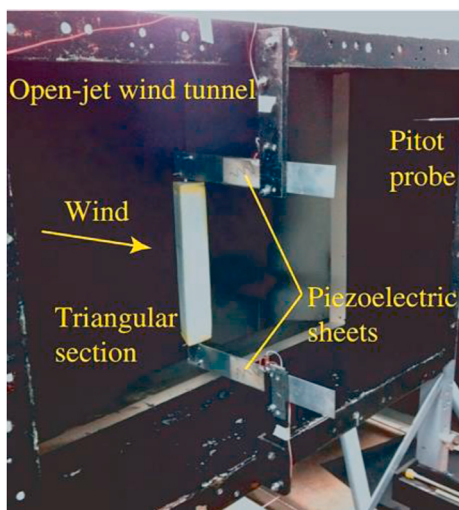


Fig. 19. Prototype galloping device [69].

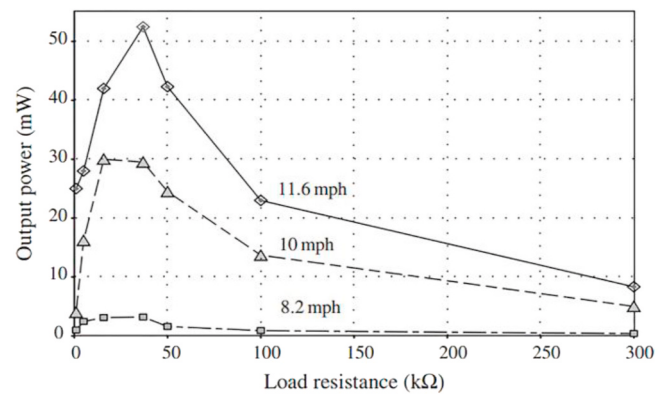


Fig. 20. Output power of the piezoelectric transducer varies versus the load resistance [69] ($L_{en} = 251$ mm; $D = 40$ mm).

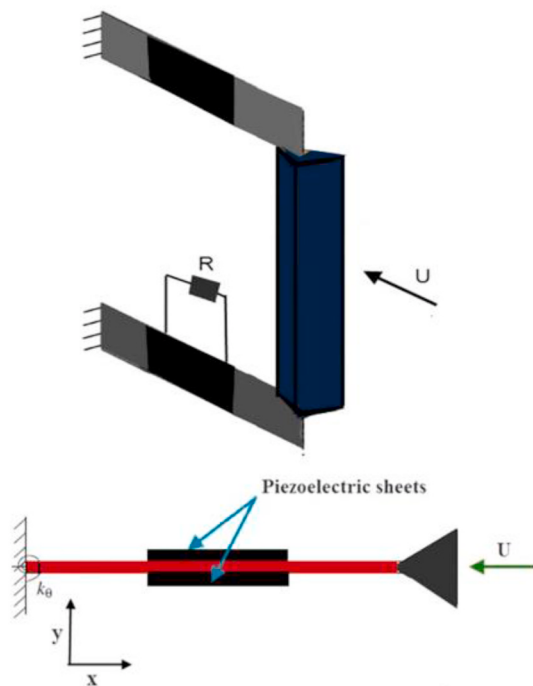


Fig. 21. Schematic of the piezoaeroelastic energy harvester with triangular oscillator [70].

electrical load resistance or flow velocity for the corresponding oscillation displacement or harvested power were similar to Ref. [70].

Secondly, the impact of mass ratio, damping ratio, or stiffness for energy harnessing and harvested efficiency of a triangular prismatic oscillator were explored under the principle of ALT [71–73]. Their research papers are reviewed next.

Some experiments, designed in 2016, were conducted to analyze the impact of the damping ratio of the equilateral triangular oscillator on the electromagnetically harvested power and its efficiency at $0 \leq Re \leq 129,000$ [71]. This equilateral triangular prismatic oscillator was elastically mounted in the recirculating water channel of Tianjin University (Fig. 22), and was constrained in the y-direction because of FIV. In addition, the side length of cross-section and total length for this triangular oscillator were $D = 100$ mm and $L_{en} = 900$ mm, respectively. Under the fixed values of mass ratio of 4.25 and spring stiffness of 1,228 N/m, the selected damping ratio ζ_{total} varied from 0.089 to 0.335. In general, as ζ_{total} increases, the amplitude decreases. Moreover, the initial galloping velocity increases. Analogously, in the galloping region,

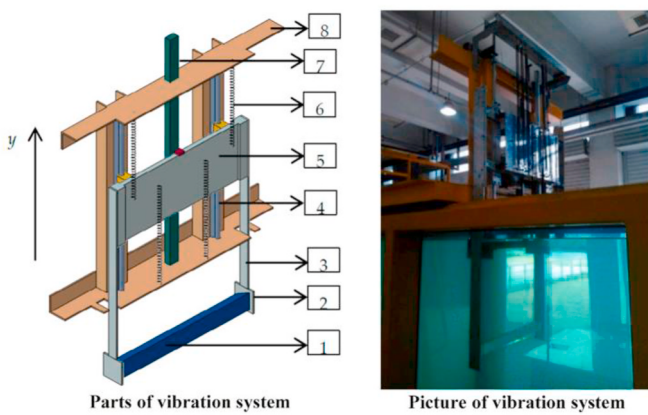


Fig. 22. Vibration system with an equilateral triangular prism [71] ($L_{en} = 900$ mm; $D = 100$ mm).

increasing the damping ratio will improve power harvesting and its corresponding efficiency. The maximum harvested power and efficiency were 53.56 mW ($\zeta_{total} = 0.284$; $U = 1.47$ m/s) and 40.44% ($\zeta_{total} = 0.284$; $U = 1.27$ m/s), respectively. Nevertheless, as damping ratio reaching up to 0.335, the galloping disappears. It should be noted that the initial water velocity of energy harnessing is 0.61 m/s.

The same experimental device, as mentioned above [71], was used to explore the influence of system damping and mass on power harvesting and its efficiency [72]. It appears that the results coincide with the research by Ref. [71], i.e., the oscillation amplitude decreases with increasing damping coefficients. Results confirmed that for mass = 36.71 kg ($m^* = 9.42$), the mode of vibration was soft galloping; as the mass increased from 40.61 kg ($m^* = 10.42$) to 44.44 kg ($m^* = 11.40$), the vibration mode gradually changed from critical galloping to hard galloping.

Using the same experimental equipment as [71], the same research group investigated the FIV phenomenon of an equilateral triangular prismatic oscillator with $D = 60$ mm and $L_{en} = 500$ mm at $0 < U < 1.6$ m/s ($0 < Re < 82,000$) [73]. A fixed value of mass ratio $m^* = 4.21$ and a series of system stiffness values varying from 300 to 800 N/m were tested. Results confirmed that, in galloping, increasing the stiffness is followed by a decrease in amplitude ratio, and as the spring stiffness reaches up to 800 N/m, galloping dissipates. Results confirmed that the amplitude increases as reduced velocity increases. This phenomenon agrees with the conclusion by Refs. [5,74], where this increase and thus dependence on Reynolds were first measured in the TrSL3 flow regime. It also can be found that the maximum amplitude ratio reaches 3.17 as U is around 1.6 m/s. In the galloping region, the frequency ratio maintains at 0.65. The results above indicated that, in the appropriate range of spring stiffness, this equilateral triangular oscillator has large oscillation amplitude and steady frequency in the infinite velocity range, which indirectly demonstrates its reliability for power harvesting.

Different from the papers just mentioned above, the studies of [75–77] investigated the effects of vertex shedding angle and attack angle on power harvesting, oscillation amplitude, and displacement of triangular prismatic oscillator. The major conclusions reached are summarized next.

A galloping-based piezoelectric energy harvester (GPEH) [75] with an isosceles triangular prismatic oscillator was tested to calculate the performance of power harvesting by Computational Fluid Dynamics [75]. An aero-electro-mechanical coupled model was numerically embedded into the GPEH. The validity of this model was verified by the GPEH prototype. The impact of the triangle vertex angle (β) and electro-mechanical strength (electromechanical coupling on the GPEH's behavior) on onset wind velocity, output power, and oscillation displacement was investigated [75]. Sixteen vertex angle values were selected varying from 10° to 160° in equal intervals. They concluded

that for weak electro-mechanical strength, the optimal vertex angle β_m is 130° ; for strong electro-mechanical strength, the β_m is related to the load resistance. Making a comprehensive analysis between the initial wind velocity and harvested energy, results confirmed that for load resistance is 120 k Ω , $\beta_m = 130^\circ$; for load resistance beyond 400 k Ω , $\beta_m = 100^\circ$.

In [58], isosceles triangular-prismatic oscillators with two different cases of vertex angles (120° , 74°) were employed to analyze the differences of energy harvesting between them. The results concluded that, the higher vertex angle oscillator can realize the larger oscillation displacement, higher harvested voltage, and higher output power than that of the lower one in the same condition. Moreover, the former has a lower onset-speed in galloping than that of the 74° oscillator. The same conclusion was obtained in Ref. [59].

It should be noted that the downstream direction is the incoming flow direction facing the triangular baseline. The corresponding reverse flow direction is the incoming flow direction facing the vertex angle, as shown in Fig. 23. The configuration tested in Refs. [69–75] is the downstream one. It should be noted that the reverse configuration, where the vertex points into the incoming flow, is not expected to generate any transverse force due to the lack of afterbody [6].

In 2005, one research team analyzed the galloping instability of the isosceles triangular-prismatic oscillator measured in a wind tunnel [76]. Six vertex angles were tested varying from 10° to 60° in an increment of 10° , and the values of attack angle changed from 0° to 180° . The influences of vertex angle and attack angle on the galloping stability of triangular oscillator have been investigated by Ref. [77]. However, the selected values of vertex angles changed from 10° to 90° in equal intervals of 10° .

Owing to the excellent performance of triangular prism placed in the flowing fluid, considerable number of scholars focused their attention on the power harvesting and flow state of such CECs. For example, the performance of energy harvesting of triangular-prismatic oscillators can be investigated by controlling the incoming flow velocity, external load resistance, mass ratio, damping ratio, stiffness, vertex angle, and attack angle of oscillator. Based on these research results, we can further explore the better performance of the power harvesting and its efficiency of triangular-prismatic oscillators.

The properties and important measurements of all these studies regarding energy extraction via transverse VIV or galloping for smooth circular cylinder and non-circular cylinder (square, rectangular or triangular oscillator) are tabulated in Table 1. From the parameters in Table 1, it can be further demonstrated that the non-circular oscillator can induce galloping and can harvest higher power than that of the smooth circular cylinder, which can undergo only VIV, not galloping. It should be noted that, according to engineering practice, the electromagnetic power-take-off system is more suitable for large size

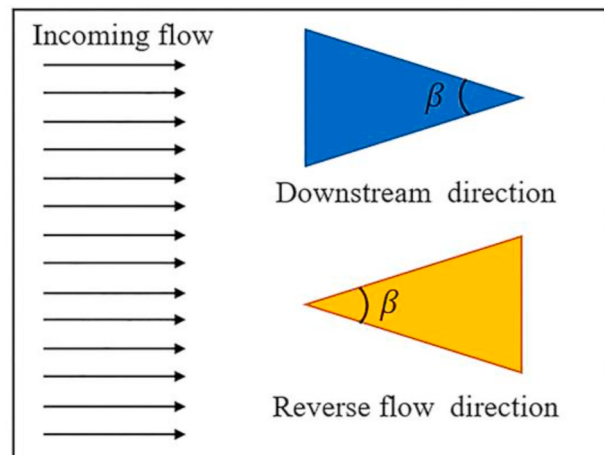


Fig. 23. Schematic of the relative positioning of a triangle in a uniform flow.

Table 1

Brief review of studies regarding energy extraction for smooth circular cylinder and non-circular cylinder.

Ref.	Method	Principle	Cross section	FIV	D(mm)	m^*/m	$K(\text{N/m})$	ζ	$P_{\max}(\text{W/m})$
[43]	2D CFD (Water)	Piezoelectric	Circular	VIV	1.6(dia.)	149.1	579	0.0012	1.0×10^{-5}
[45]	Exp. (Water)	Piezoelectric	Circular	VIV	20(dia.)	1.114	—	0.0750	1.41×10^{-3}
[46]	Exp. (Air)	Piezoelectric	Circular	VIV	30(dia.)	—	—	0.0109	1.42×10^{-3}
[57]	Modelling	Piezoelectric	Square	galloping	15(side)	0.44 kg	—	0.0013	1.7
[60]	Modelling	Hybrid	Square	galloping	30(side)	0.44 kg	—	0.0013	0.7850
[62]	Modelling	Piezoelectric	Square	galloping	30(side)	0.015 kg	—	0.0069	6×10^{-4}
[63]	2D CFD (Water)	Electromagnetic	Square	VIV, galloping	90(side)	1.0–4.0	1063	0.6000	143
[65]	2D CFD (Water)	Electromagnetic	Rectangle	VIV, galloping	218	1.725	1063	—	315.9
[69]	Exp. (Water)	Piezoelectric	Triangle	galloping	40(side)	—	—	—	0.21
[71]	Exp. (Water)	Electromagnetic	Triangle	VIV, galloping	100(side)	4.25	1228	0.2840	59.51

equipment, while a piezoelectric PTO is suitable for tiny amounts of power conversion. The summary in Table 1 supports this conclusion. It should be pointed out that the harnessed power in Table 1 represents the maximum power per unit length of prism.

3.3. Cylinders with other cross-sections

The studies reviewed in Sections 3.1 and 3.2 were mainly focused on the FIO and energy harvesting of oscillators with circular, square, rectangular, or triangular cross-section of a cylinder or prism. Based on the above analysis, in this section, a comparison of FIO response and power harvested is further conducted for other cross-section oscillators. Results of these studies regarding energy extraction via transverse VIV or galloping for different cross-section oscillator are tabulated in Table 2. Detail analysis for these papers found in the literature follows.

Experimentally, the power output and voltage harvested of five different cross-section oscillators in galloping were investigated in the range $0 < U < 8 \text{ m/s}$ [78]. These five oscillators include square, rectangle (two cases), triangle, and D-shape cross-section of the cylinder/prism which have the same length of $L_{en} = 150 \text{ mm}$ and same windward area of $S_{cs} = 6,000 \text{ mm}^2$, as shown in Fig. 24. The configuration and dimensions of these five kind of cross-sections are shown in Fig. 24-c. It should be noted that the power conversion was realized by a piezoelectric transducer with external load resistance. The experimental data were measured using a laboratory prototype device (Fig. 24-b). Fig. 25 shows that the optimal load resistance was $105 \text{ k}\Omega$. Results showed that the maximum power (8.4 mW) among all cross-sections was produced by this square oscillator at $U = 8 \text{ m/s}$. Moreover, the extremely low output power was observed in the cases of the rectangle ($40 \times 26.7 \text{ mm}$), triangle, and D-shape cross-sections. Results confirmed that the lowest initial air flow-velocity for power harnessing was $U = 2.5 \text{ m/s}$, which is smaller than that of the results obtained by previous studies (4 m/s in Ref. [79]; 3.576 m/s in Ref. [80]).

Numerically, the FIO response and hydrokinetic power of four kinds of oscillators with different shape of cross-section were explored by using a 2-D Unsteady Reynolds Average Navier-Stokes (URANS) method at $10,000 \leq Re \leq 130,000$ [56]. Fig. 26 shows, a PTC-cylinder (Passive Turbulence Control; Diameter of 88.9 mm), square cylinder, a quasi-trapezoid I (The long and short edges in flow-direction are $1.0D$

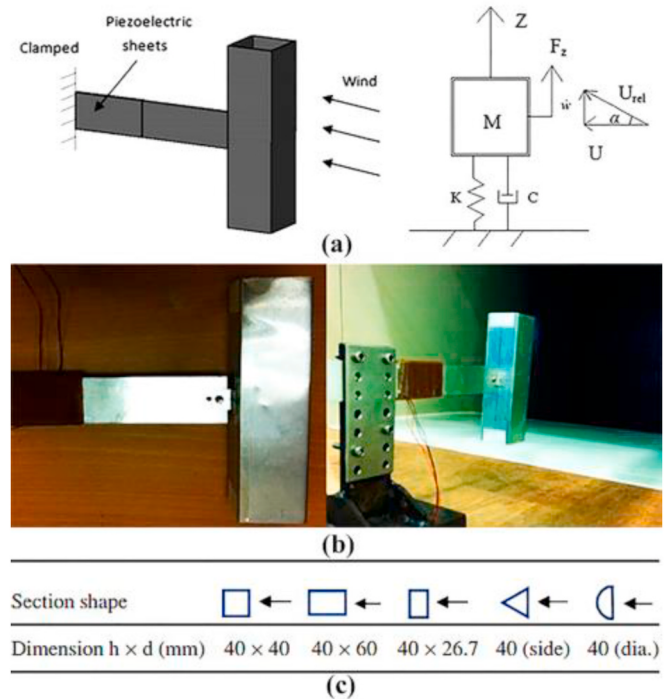


Fig. 24. Piezoelectric energy harvester with different cross-section oscillator [78].

and $0.5D$; The long edge faces the incoming wind; The two edges in the oscillating-direction both are $0.25D$), and a triangular prism were selected in this study. The spring stiffness and harnessing damping ratio were selected as $K = 1,750 \text{ N/m}$ and $\zeta_{\text{harness}} = 0.04$, respectively, for all cases. The results indicated that the maximum power harvesting of PTC-cylinder and quasi-trapezoid I were 25.67 W and 24.45 W , respectively. As shown in Fig. 27, the variation trend of energy efficiency increases initially and decreases later. The peak efficiency value (η_{harness})_{max} occurred at $Re = 60,000$ for all section cases except the triangular prism. The two maximum efficiencies are respectively 45.7% and 37.9% , which can be respectively found in quasi-trapezoid I and PTC-cylinder. According to above analysis for power characteristics, the authors found that the PTC-cylinder and quasi-trapezoid I are the two optimal oscillators.

[81] numerically investigated the oscillation amplitude and the performance of harnessed power for five different cross-section tandem oscillators; including triangular prism, pentagon prism, square prism, circular cylinder, and Cir-Tria cylinder, as shown in Fig. 28. It was demonstrated that the Cir-Tria oscillator becomes the optimal case to harvest more energy and obtain higher amplitude than that of the other cases, corresponding to maximum energy efficiency 26.5% and $(A/D)_{\text{max}} = 1.17$. On the contrary, the square oscillator developed the

Table 2

Brief review of energy extraction for different optimal cross-section oscillator.

Ref.	Method	Principle	Optimal cross-section	$P_{\max}(\text{W})$	$\eta_{\max}(\%)$
[78]	Exp. (Air)	Piezoelectric	Square	8.4×10^{-3}	—
[56]	2D CFD (Water)	Electromagnetic	quasi-trapezoid I	24.45	45.7%
[81]	2D CFD (Water)	Electromagnetic	Cir-Triangle	0.26	26.5%
[82]	Exp. (Water)	Electromagnetic	Circular	—	80%
[83]	Exp. (water)	Piezoelectric	Semi-cylinder	4.14×10^{-3}	—

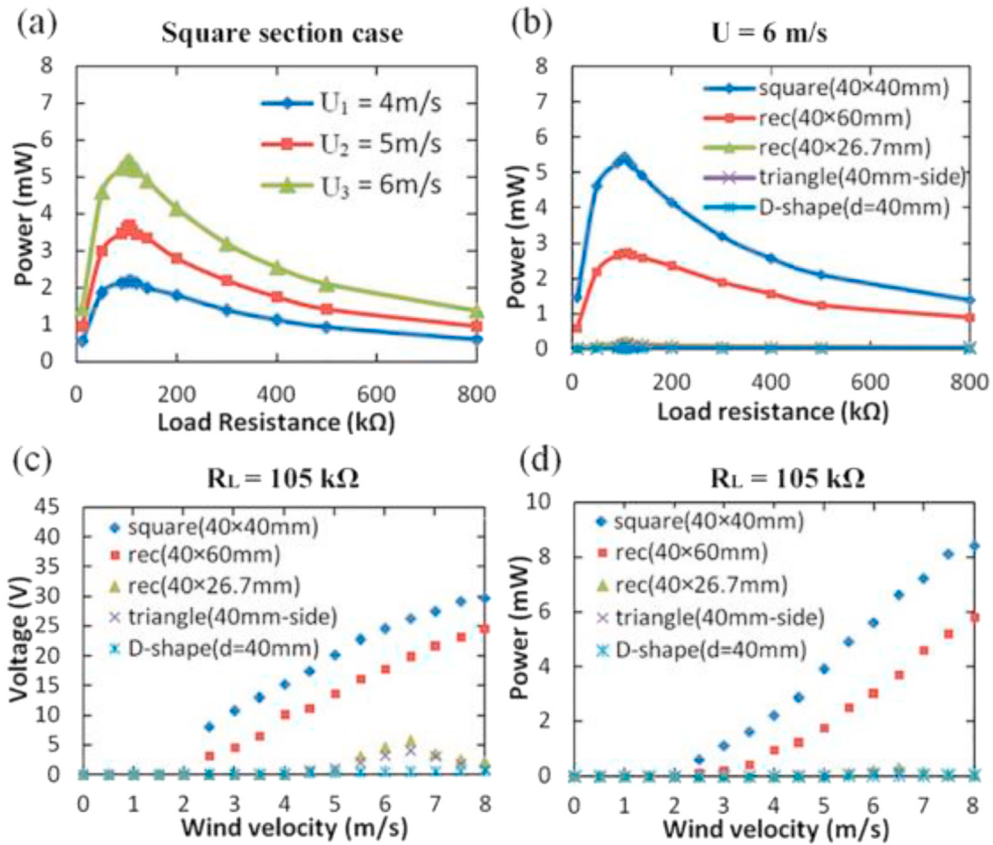


Fig. 25. Measurements of power and voltage [78] ($L_{en} = 150$ mm).

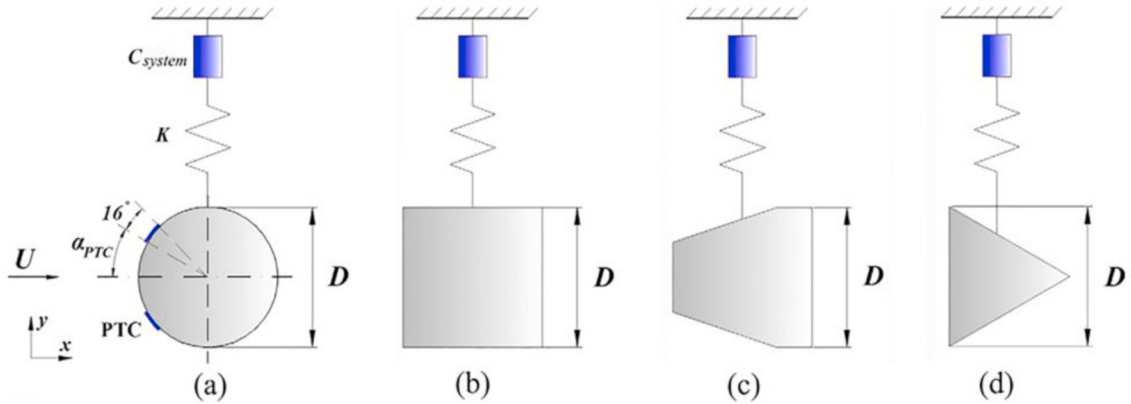


Fig. 26. Schematics of oscillator models: (a) PTC-cylinder; (b) square cylinder; (c) quasi-trapezoid; (d) triangular prism [56].

minimum amplitude ratio $A/D = 0.7$ and vibration frequency. Therefore, the power harvesting and its efficiency of a square prism case were the lowest.

According to previous studies of variables by Ref. [57], another similar study used the same numerical model and method to convert the oscillator's transverse galloping to electrical energy through a piezoelectric device [58]. The difference between these two studies is that the former only studied square, however, the latter has four different kinds of cross-section oscillators, including square prism, isosceles-triangle prism ($\delta = 30^\circ$), D-section prism, and isosceles triangle prism ($\delta = 53^\circ$). The D-section oscillator and isosceles triangle oscillator ($\delta = 30^\circ$) respectively, have the highest and lowest initial galloping speed. The isosceles triangle oscillator ($\delta = 30^\circ$) was proven to be the optimal power harvesting oscillator at lower velocity conditions. Nevertheless, at a

higher velocity, the best one was the square oscillator. Similar results, measured by the same method, can be found in Ref. [59].

Similarly, to the above studies, four different cross-section prisms were tested to analyze the corresponding FIO characteristics and power conversion efficiency, given by Eq. (12). The experimental equipment and the transverse oscillation prisms can be seen in Fig. 29. It was shown that the maximum amplitude ratio of triangular prism, right square prism, circular cylinder, and diamond square prism was around 1.8, 1.2, 1–1.2 and 0.4–0.5, respectively. The maximum value of efficiency of these oscillators was 57%, 1.8%, 80%, 6%, respectively. Results confirmed that circular cylinder and regular triangle prism both have higher vibration stability than those of the other two cross-sections. Therefore, it can be clearly found that the optimal oscillators are the circular cylinder and regular triangular prism due to their high power

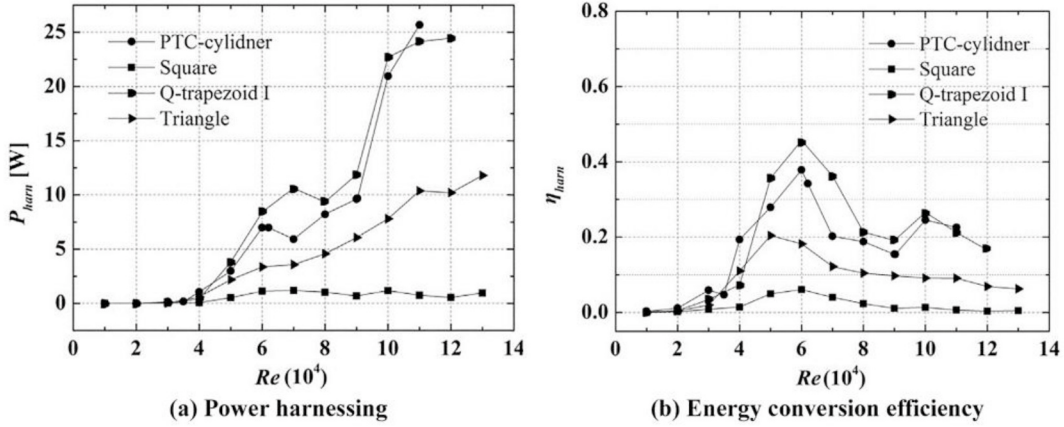


Fig. 27. The diagram of power harnessing and energy conversion efficiency [56] ($D = 88.9$ mm; $K = 1,750$ N/m; $\zeta_{\text{harness}} = 0.04$; $Re = 10,000\text{--}130,000$).

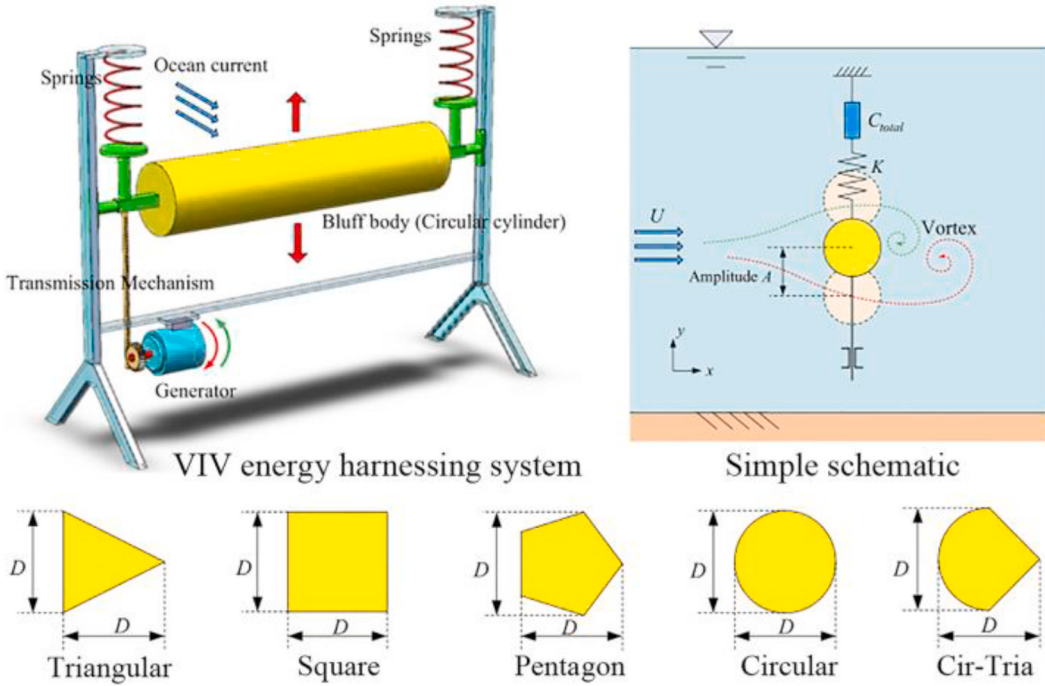


Fig. 28. Schematics of a VIV energy harnessing system with different cross-section prisms/cylinders [81] ($m^* = 0.93$, $K = 76.5$ N/m, $D = 32$ mm).

conversion efficiency and excellent vibrational stability (steady oscillatory behavior).

A piezoelectric energy harvester with three kinds of cylinder/prism, which have different cross-section [83] i.e. cylinder, triangular-prism ($\beta = 80^\circ$) and semi-cylinder, have been tested to harvest the hydrodynamic energy from low velocity flow (0.2–0.54 m/s) by combining the experimental and numerical methods, as shown in Fig. 30. In particular, this cylinder is subjected to the VIV force simulated by the modified van der Pol model. In galloping, the other two oscillators were subjected to lift force modeled by the quasi-steady hypothesis [61]. The nonlinear galloping force coefficient (C_g) can be expressed as:

$$C_g = \lambda_1 \tan \alpha + \lambda_3 (\tan \alpha)^3 \quad (15)$$

where α is the attack angle; λ_1 and λ_3 are the linear term and cubic term coefficients, respectively, selected as in Ref. [84]. Results indicated that the coefficient ratio λ_1/λ_3 and power harvested are positively correlated. That is to say, increasing of λ_1/λ_3 is followed by increase of the harvested power. As a result, the galloping energy harvester has a better

performance than that of the VIV ones. Besides that, the semi-circular prism is proved to be the optimal energy harvester due to the phenomenon that it has the minimum initial power velocity (0.3 m/s) and has the maximum power (4.14 mW) in the cases of these three oscillators.

To determine the differences in FIO and power harnessing between the different cross-section oscillators, a comprehensive comparison has been conducted in this section. In addition, a comparison of power extraction realized by transverse VIV or galloping for different cross-section oscillators is listed in Table 2. Combined with the analysis in Section 3.3, it can be observed from Table 2 that the optimal section will change with the variation of the set parameters. The following conclusions can be drawn:

- (a) In general, in air, in the experimental work reviewed, non-circular cylinders typically do not undergo galloping. Galloping and VIV both occur when testing in water. In real life of course, when Reynolds numbers are higher VIV and galloping occur in air as well.

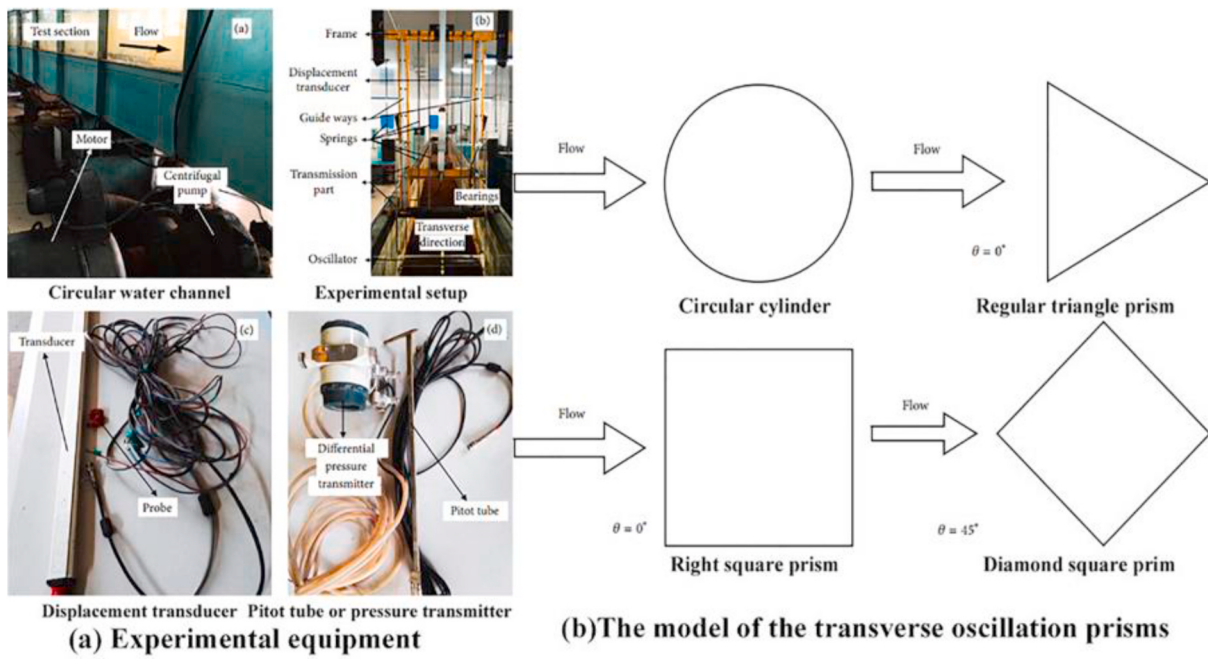


Fig. 29. The experimental equipment and the model of the transverse oscillation prisms in Ref. [82].

- (b) The electromagnetic power-take-off (PTO) system is more suitable for converter in water, while a piezoelectric PTO is suitable for tiny amounts of power conversion in air.
- (c) In rectangular prisms, the cross-sectional aspect ratio plays an important role in harnessed power. It is defined as the ratio of the inflow side to the transverse side. Specifically, as the aspect ratio decreases (staying above 1 though), the power increases especially at high flow velocity.
- (d) In the triangular-prism shape, the direction of the cylinder plays an important role. When the vertex points downstream, the oscillator is subjected to lift (transverse force) due to the presence of the after-body. When the vertex points into the flow, the transverse pressure change caused by either the VIV or the galloping mechanism cannot induce lift as there is no afterbody to take the pressure.
- (e) Another important factor in the triangular prism is the vertex angle. The optimal angle depends on the Reynolds number and damping ratio.
- (f) Other shapes such as hollow square, diamond quasi-trapezoid prisms/cylinder were studied both experimentally and numerically as well.

4. Passive turbulence control OF FIO energy converter

As discussed in Section 3, the two FIO phenomena occur as the selected cylinder is placed transversely to the incoming flow, and FIO response is enhanced or suppressed by introducing additional changes to the cross-section. In the effort to harness more hydrokinetic energy, the fluid-structure interaction is enhanced. That can be achieved using control in two different ways: (a) Apply passive control; or (b) apply active control. Among them, the passive control method does not require external energy input; it can change the flow separation point, the shear layer turbulence level, the vortex roll up, and the shear layer instability that leads to galloping. In this section, the variation of FIO and the corresponding energy generated due to passive turbulence stimulation is studied. Changing the surface roughness of the cylinder oscillator alters its boundary layer and shear layer characteristics, thus influencing its pressure distribution on the cylinder, in turn, changing the lift and drag hydrodynamic force, changing the vibration characteristics of the

passively controlled cylinder compared to the smooth cylinder. The studies on turbulence stimulation are reviewed in this section and results are summarized in Table 3.

The idea of utilizing selectively distributed surface roughness of the cylinder to suppress or enhance the two FIO phenomena was first proposed by Bernitsas and Raghavan et al. in several experimental studies [85,86]. From Ref. [85], it can be concluded that the lift force and oscillation amplitude of the oscillator reflect the ability of energy harvesting of the energy converter. In addition, broadening the range of FIO synchronization regions can enhance the power-harvesting stability of the energy converter. Placing the roughness strip in the range of 57°–80° (Figs. 31 and 32) from the upstream stagnation point can generate the increase of the synchronization range and the amplitude ratio A/D. In VIV testing in the TrSL3 flow regime, A/D has reached 1.9 [5] and in the galloping region it is only limited by the converter frame [63]. The results also indicated that the onset velocity of the synchronization region can be reduced by fixing the roughness strip at the appropriate position of the cylinder. The VIV suppression of a cylinder using two cases of roughness distribution was studied [86], as shown in Fig. 31. Results confirmed that distributing roughness appropriately can realize reduction of the FIO synchronization region and decrease of the vibration amplitude, showing that FIO and energy harvesting can be suppressed.

In 2011, a selectively distributed surface roughness, called passive turbulence control (PTC), was attached on a smooth cylinder to analyze the FIV response and power-harvesting potential of the cylindrical oscillator [7,87]. Fig. 32 shows that, two surface roughness strips (PTC) with same characteristics are fixed parallelly and symmetrically on both sides of the stagnation line of the cylinder. The design parameters of PTC include placement angle (α_{PTC}), strip area coverage (θ_{sac}) and roughness height (H'). Among them, the roughness height can be expressed as:

$$H' = k + p \quad (16)$$

where k represents the grit's average height; and p is a stack height which consists of the height of the backup paper regarded as an important element and the height of the double-sided tape regarded as a tool to fix the sandpaper on the cylinder. It should be mentioned that the roughness strips influence the flow separation points and stimulate the boundary layer resulting in the higher strength of shedding vortex and higher stability of altering lift force, increasing the potential for energy

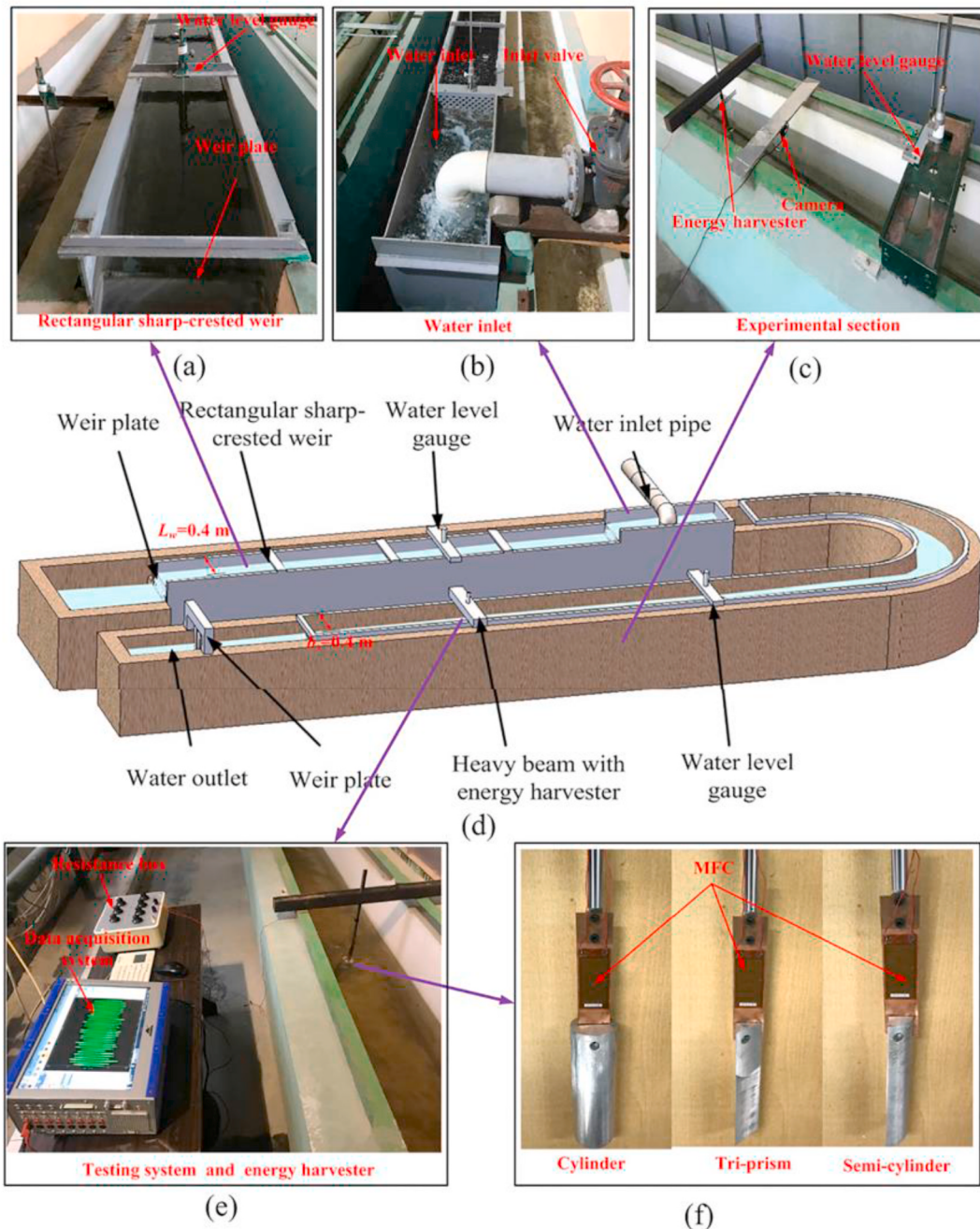


Fig. 30. Experimental setup for hydrokinetic energy harvesting [83] ($L_{en} = 160$ mm; streamwise projection diameter of oscillator $D = 50$ mm; mass of the bluff body $m = 0.324$ kg).

Table 3

Comparison of power harvesting by using FIO for different appendages on the oscillator cylinders.

Ref.	Method	Appendage	Re	$D(\text{mm})$	$P_{max}(\text{W/m})$	$\eta_{max}(\%)$
[30]	Exp. (Water)	PTC	30,000–120,000	88.9	22.35	44
[94]	Exp. (Water)	PTC	30,000–110,000	88.9	25.74	28
[94]	2D CFD (Water)	PTC	30,000–110,000	88.9	22.92	37
[96]	Exp. (Water)	Tripping wires	2900–22,000	25	0.15	12.47
[103]	Exp. (Wind)	Cylindrical rods	$0 < U < 7$ m/s	48	3×10^{-4}	–
[105]	2D CFD (Water)	Fin-shaped strips	30,480–152,400	101.6	66	20
[106]	Exp. (Wind)	Fins	$0 < U < 7$ m/s	24	1.67×10^{-4}	–
[112]	2D CFD (Water)	Impellers	30,512–488,567	305	283.27	47.1
[113]	2D CFD (Water)	pentagram impeller	14,000–80,000	38.1	16.07	26.3

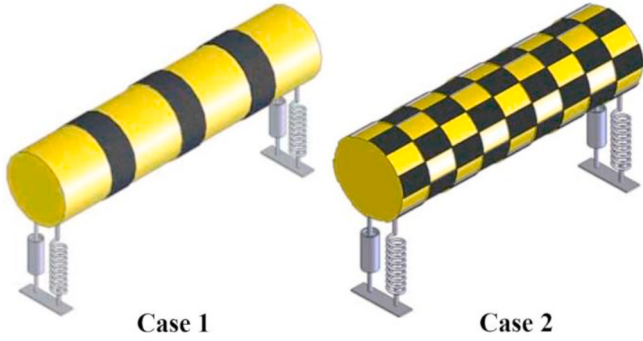


Fig. 31. Two cases of roughness distribution to reduce/suppress VIV [86].

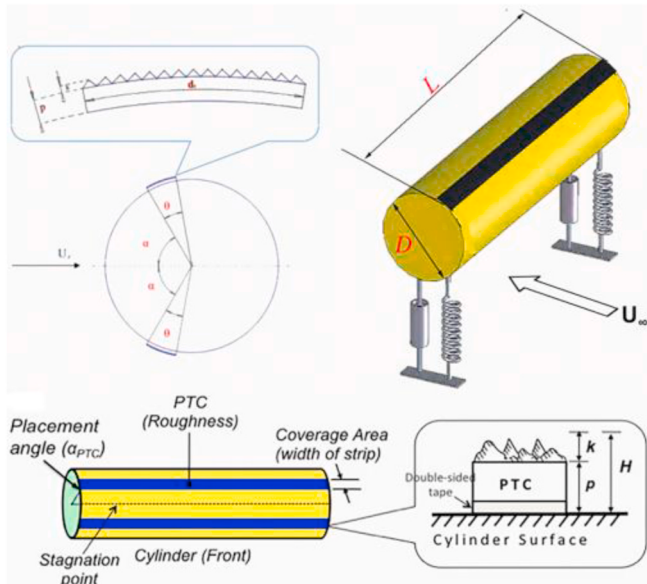


Fig. 32. Schematic of passive turbulence control (PTC) [7].

harvesting. It should be emphasized that the selected PTC height has the same order of magnitude as the formed thickness of the boundary layer formed on the cylinder surface [7]. PTC is mainly used in the VIVACE Converter in the LTFSW Channel of the MRELab of the University of Michigan, as shown in Fig. 33, for the purpose of expanding the



Fig. 33. VIVACE Converter in the LTFSW Channel of the MRELab [55,94]: (a) Lab module; (b) Schematic diagram.

synchronization region of VIV and enhancing the power-conversion efficiency from the incoming flow.

Galloping can increase the oscillation amplitude and enhance the performance of energy conversion. However, galloping can only be induced by the PTC-cylinder not the smooth circular cylindrical oscillator. Therefore, higher energy harvesting can be obtained by attaching passive turbulence control on the smooth cylinder. Nevertheless, the increased amplitude of oscillation results in reduction of the efficiency of a CEC, like VIVACE [6], as can be easily surmised from Eqs. (11) and (12) since the amplitude of oscillation appears on the denominator of the efficiency calculation. Accordingly, such converters generate two different local optima: one located in the VIV region, however, another located in the galloping region. Besides that, both the power and efficiency lines exhibit two local optima. However, the optima of power and efficiency represent different designs. Further, the global power optimum occurs at the high velocity in galloping (Fig. 34). On the contrary, the global efficiency optimum occurs at the initial stage of VIV upper branch (Fig. 35).

The FIO response of a cylinder with PTC for all its four parameters was studied to enhance the energy conversion efficiency at $3 \times 10^4 \leq Re \leq 1.2 \times 10^5$ [7]. Results confirmed that choosing the proper PTC can be beneficial to energy harnessing. It was verified that the influence of strip

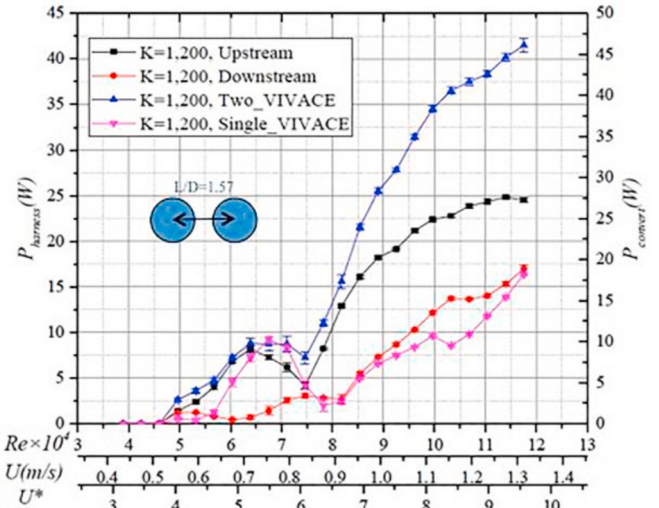
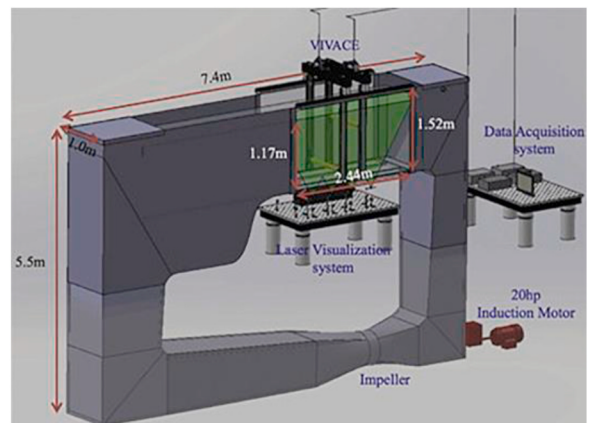


Fig. 34. Experimental power output from a two-cylinder VIVACE device showing the VIV and galloping local optima [34].



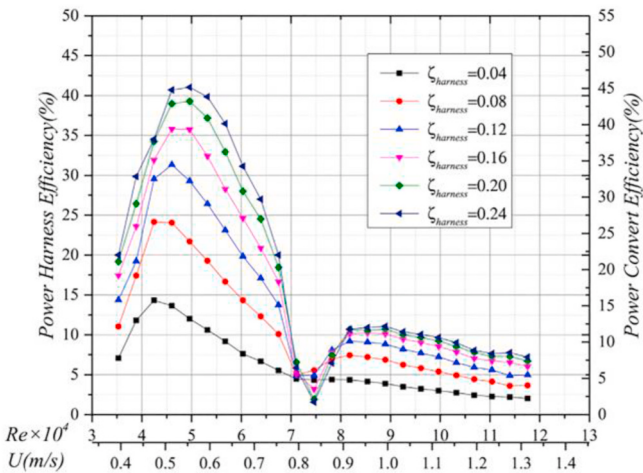


Fig. 35. Experimental power efficiency for a two-cylinder VIVACE device showing the VIV and galloping local optima [30].

area coverage and roughness height on VIV and galloping is small. Park et al. studied the sensitivity to zone covering by varying the location and width of the turbulence stimulation strips and revealed the hierarchy of zone dominance [8]. In other words, when more than one zone is covered, the dominant zone is Strong Suppression and followed by Galloping. Combining with other studies [88,89], the optimal coverage angle of the strip area was identified to be 16° in terms of the FIO. It was also verified that, in the range of $10^\circ \leq \alpha_{\text{PTC}} \leq 80^\circ$, the width of synchronization region can be expanded or contracted with the variation of α_{PTC} .

In 2011, an experiment was conducted to analyzed the power harvesting from the FIO of a PTC-cylinder parametrically in the TrSL3 regime [90]. Fig. 36 shows, a PTC-cylinder was elastically supported by a pair of real springs and was constrained to oscillate in the perpendicular direction corresponding to an incoming flow. The independent variables were the placement location and the surface roughness of the PTC (Fig. 32). Compared to the smooth cylinder, a wider synchronization region can be found in the rough cylinder case because of the early onset of galloping. Thus, the increase in power harvesting of the rough cylinder was 300% than the power of the smooth one. The cylinder was

tested with a smooth strip and was found to have similar power-harvesting characteristics as the cylinder with rough strip in terms of synchronization range and FIO regions. Most important, however, is the fact that the smooth-strip cylinder performed better in terms of amplitude response in all hydrodynamic ranges. That is, the sandpaper roughness did not help in the generation of stronger vortices or reducing the formation length. Both of these characteristics result in higher lift coefficient in VIV because the shed vortices become stronger and shed closer to the cylinder's after-body. This was the case because their tests were conducted in the TrSL3 flow regime where the shear layers are already fully turbulent and surface roughness could not enhance vortex strength more. On the contrary, it increased the skin friction, which reduced the amplitude. This increase was very small as the skin friction is equal to only about 5% of the normal pressure force on a cylinder.

In 2012, Ref. [91] presented a mapping relation between the placement angle of PTC and FIO response based on a large number of parametric experiments for two roughness configurations (regarded as commercial grade sandpaper, i.e., P180 and P60, in Fig. 37). It was found that a simple and effective FIO amplifier or suppressor can be designed by attaching the PTC on a different placement position of the cylinder. Starting from the front stagnation line, six zones of placement angle with different effect were identified: weak suppression 1 (WS1), hard galloping 1 (HG1), soft galloping (SG), hard galloping 2 (HG2), strong suppression (SS), and weak suppression 2 (WS2) [91]. The value of this discovery is that, in most studies [8,9,88,92,93] on suppressing VIV or increasing energy conversion, the PTC position was selected by referring to the “PTC-to-FIM Map”, PTC map for short (Fig. 37).

In 2013, the impact of PTC coverage width, PTC configuration and PTC multi-zone covering for the FIO response of the cylinder were investigated experimentally [8]. Furthermore, similar study explored the amplitude and frequency of the PTC-cylinder with the incoming flow speed for two roughness configurations (commercial grades P180 and P60) and three different identified zones (namely SG1, HG1, and HG2) [9]. As expected, the velocity range of FIO of a circular cylinder with PTC dramatically increased compared with the smooth cylinder, for the reason, due to earlier onset of galloping. This increased the energy conversion produced by the current energy converter in the LTFSW channel. As mentioned earlier in this Section though, the power efficiency is higher in VIV than in galloping.

Ref. [94] applied CFD with 2D-URANS to simulate the power harnessing for a rigid cylinder with the PTC ($\alpha_{\text{PTC}} = 20^\circ$; $\theta_{\text{pac}} = 16^\circ$; $H' = 0.847$ mm) in FIO in the range $3 \times 10^4 < Re < 1.1 \times 10^5$. The numerical simulation was implemented by utilizing a finite-volume discretization method based on OpenFOAM. Additionally, the results were verified by the same experiment conducted in the LTFSW channel. Four characteristic ranges including the VIV initial or upper branches, VIV-galloping transition, galloping region were readily identified in the tested speed range. It can be observed (Fig. 38) that power harvesting can be

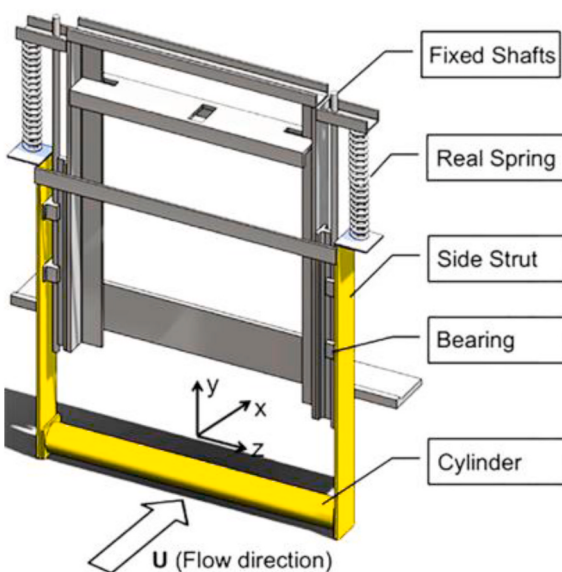


Fig. 36. A simple schematic of motion mechanism [90] ($D = 88.9$ mm; $L_{\text{en}} = 914.4$ mm; $m^* = 1.72$; $K = 775$ N/m; $\zeta_{\text{total}} = 0.103$).

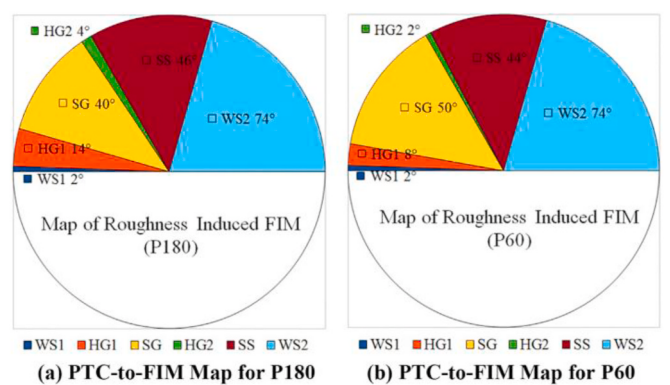


Fig. 37. Map of FIO induced by selectively located roughness [91].

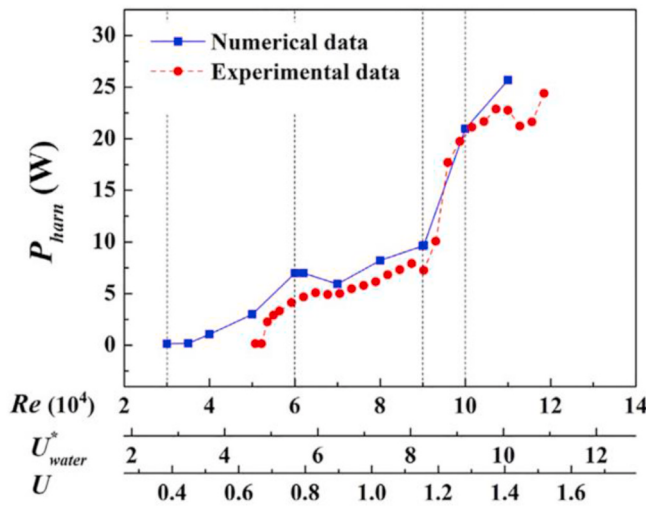


Fig. 38. Hydrokinetic power harvested by a single cylinder VIVACE device with PTC [94] ($L_{en} = 914.4$ mm; $D = 88.9$ mm; $m^* = 1.896$; $K = 1,600$ N/m; $\zeta_{harness} = 0.04$).

produced continuously in the entire synchronization range and increase with increasing of the incoming flow speed. The maximum harnessed power for numerical simulation and experiment was 20.96 W ($Re = 100,000$) and 23.54 W ($Re = 101,536$), respectively. The maximum power efficiency for numerical simulation was 37% ($Re = 60,000$), as shown in Fig. 39.

The effect of cylindrical surface protrusions on the performance of energy harvesting was experimentally investigated at $3000 < Re < 30,000$ (in TrSL2) [95]. Fig. 40 shows the surface protrusions in the form of smooth or rough strips fixed on the smooth cylinder. Results confirmed that the installation position of strips is of pivotal importance for the FIV response, and the optimal circumference location is around $\alpha_{PTC} = 60^\circ$. Compared to the smooth oscillator, the transverse oscillation can be induced and enhanced by the rough oscillator. Being different from the previous research in TrSL3 [90], the research [95] in TrSL2 shows, the large smooth strip case can produce stronger galloping and obtain higher energy-harnessing potential than that of the rough strips cases. Fig. 41 shows that V_{rms}^2 for the strip-cylinder has higher value in high Reynolds numbers comparing with a smooth cylinder, especially for the smooth strip, where V_{rms}^2 represents the power harvesting.

Evidently, the passive control method above is a method that

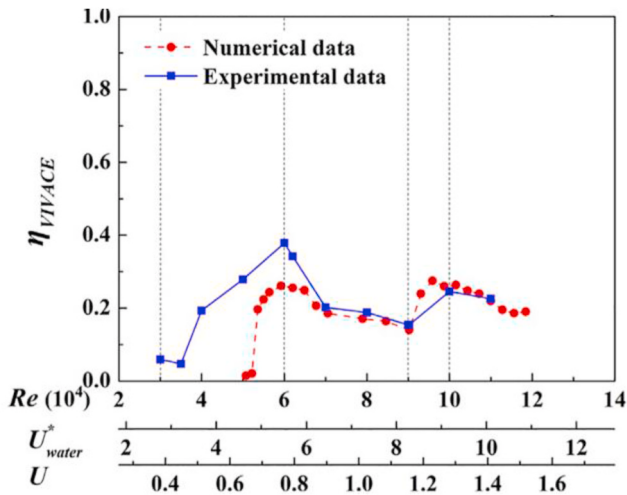


Fig. 39. Power efficiency of a single cylinder VIVACE Converter with PTC [94] ($L_{en} = 914.4$ mm; $D = 88.9$ mm; $m^* = 1.896$; $K = 1,600$ N/m; $\zeta_{harness} = 0.04$).

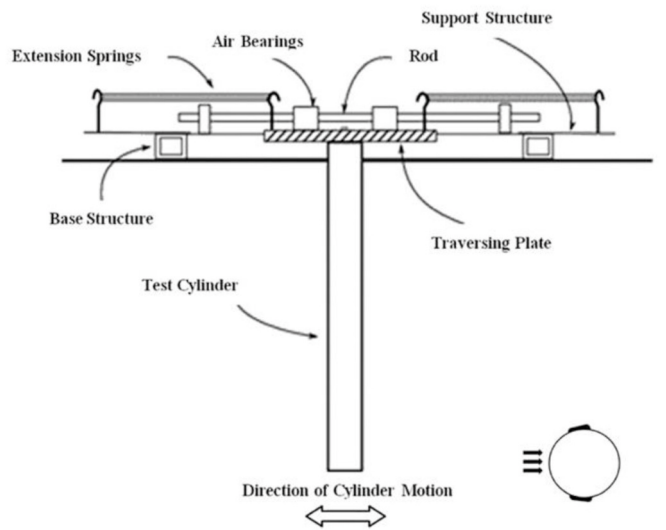


Fig. 40. Schematic of the experiment set-up [95] ($L_{en} = 508$ mm; $D = 48.26$ mm).

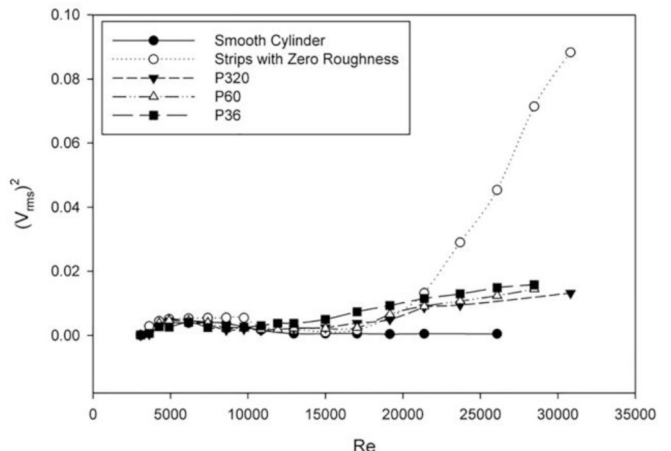


Fig. 41. The variation of $(V_{rms})^2$ with Re for different cases [95] ($L_{en} = 508$ mm; $D = 48.26$ mm).

attaches a PTC on a rigid smooth circular cylinder. Consequently, the PTC-cylinder can broaden the velocity range of energy acquisition by inducing onset of galloping before the end of original VIV region. Besides that, there are many effective passive-control appendages such as small-size tripping wires/rods, fin-shaped strips, splitter plates, free-to-rotate impeller, etc., which are reviewed in the following analysis. The FIV characteristics and energy harvesting efficiency of the energy converter were detailedly analyzed by selecting the appropriate research parameters such as the circumferential locations (θ), shape of the tripping rod, and the length of the splitter and so on. The relevant studies can be found as follows:

In 2013, the team of Quadrante added a pair of tripping wires facing the incoming-flow side of a cylinder to analyze the potential impact of position angle of symmetric tripping wires on the cylinder's oscillation amplitude and power harvesting efficiency [96]. The selected Reynolds number was $2900 < Re < 22,000$ ($2 < U^* < 12$). Based on [97], the VIV energy harvesting can be realized by utilizing the leverage principle. Using the same position angles (with respect to the stagnation line) of tripping wires as [98], the authors selected two angles, namely 60° and 75° . As they hypothesized, adding the tripping wires increases the oscillation amplitude and broadens the VIV synchronization region. The maximum electric power generation and maximum power efficiency

were 0.07 W (for the case of 60° at $U^* = 12$) and 12.47% (for the case of 75° at $U^* = 6.5$), respectively. It was notable that, for the case of 75° , the increment of maximum power efficiency was higher than 300% compared to the smooth cylinder in VIV upper branch.

Other studies on attaching symmetric tripping wires on a circular cylinder were done [99–102]. These studies investigated the flow characteristics, fluctuating flow forces, and FIV performance under the effects of the circumferential positions and other important parameters.

In 2014, the FIO characteristics of a rigid cylinder were investigated experimentally by analyzing indirectly the vibration amplitude and frequency [102]. It was found that introducing the tripping wires can obviously alter the FIO response. For the cases of $\theta = 60^\circ$ and 75° , the cylinder developed a wider range of synchronization region. It also resulted in an increase of the maximum amplitude by 52% comparing with the smooth cylinder case. For $\theta = 120^\circ$, there was no vortex shedding behind the cylinder, resulting in suppression of FIO.

By mounting two small-diameter cylindrical rods on the surface of a plain cylinder ($L_{en} = 240$ mm), Ref. [103] explored the effects of circumferential location θ and diameter ratio (d/D , the d is the diameter of rod) on the piezoelectric energy harvesting (Fig. 42). The incoming wind velocity U was varied from 0 m/s to 7 m/s. It is worth pointing out that the energy harvesting was realized based on the cylinder's FIO in a wind tunnel. In the VIV region, $\theta = 75^\circ$ can produce more energy than that of the other cases. In the case of $\theta = 60^\circ$, the output voltage increases as wind speed increases, inducing galloping rather than being limited to the VIV region. Therefore, $\theta = 60^\circ$ is an optimal angle that can obtain higher energy harvesting than that of the other cases (especially for the plain cylinder) due to the early onset of galloping. Additionally, the results showed that increasing d/D is accompanied by positive influence on piezoelectric power harvesting. Consequently, selecting the appropriate values of θ and d/D can improve the harvester's performance and expand the range of power harvesting. It can be observed that the maximum harvested power of $72 \mu\text{W}$ occurs at $\theta = 60^\circ$ and $d/D = 20\%$ when wind velocity is around 6 m/s.

As is well known, the hydrokinetic instability can be caused by a non-circular cross-section cylinder, and the unstable amplitude response will increase with increasing incoming flow velocity. Therefore, we selected some typical studies which have the non-circular cross-section appendages to investigate their effect on power harvesting.

In addition to considering the impact of circumference location of small-diameter rods on the piezoelectric power harvesting from the cylinder's FIO, the rod-shape is also considered as an important parameter in Ref. [104] in the range $0 < U < 8$ m/s. As shown in Fig. 43, three different cross-sections of rods - circular, triangular and square - are installed symmetrically on the incoming flow side of a cylinder. Results showed that the case of circumferential location $\theta = 60^\circ$ has greater output voltage than that of the other cases (including the plain cylinder) in galloping. Besides that, the variation of output voltage with

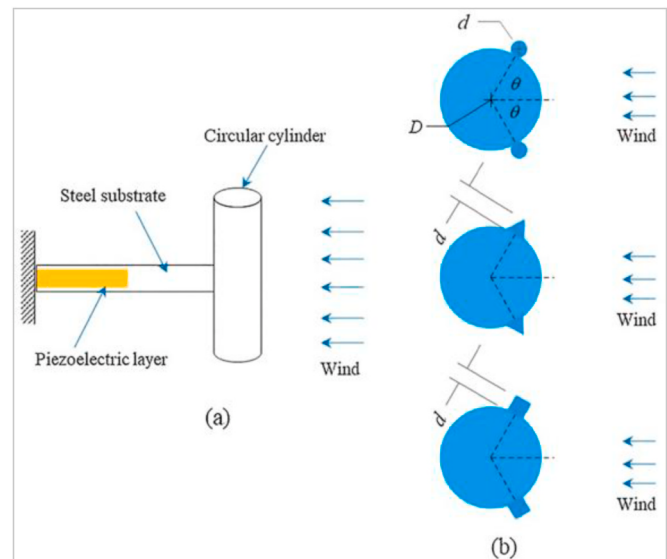


Fig. 43. Schematic of the energy harvester with different types of rods in Ref. [104] ($L_{en} = 240$ mm; $D = 48$ mm).

the incoming flow velocity for three different cross-section rods is similar. In addition, fixing the triangular rods on the cylindrical oscillator results in the highest harnessed power in these three rod-shaped cases. Therefore, the cylinder connecting the triangular rod at $\theta = 60^\circ$ can produce the highest output voltage (around 19 V at $U = 8$ m/s) in the tests.

A numerical simulation was used to study the power harvesting from the FIO of a cylinder with two same, symmetric and parallel fin-shaped strips by utilizing a fluid-structure interaction method at $30,480 \leq Re \leq 152,400$ [105], as shown in Fig. 44. The most crucial point is that the authors analyzed the energy harvesting and power efficiency under the impact of the circumferential location θ of strips. Results showed that for $\theta = 20^\circ$ or 45° and $\theta = 0^\circ$ or 60° , the form of FIO are, respectively, the HG1 and the HG2 as defined in Fig. 37. Galloping disappeared when θ reached up to 90° and the FIO was suppressed when α increased up to 120° . For $\theta = 90^\circ$ or 120° , a narrow wake was formed owing to the reason that the boundary layer's separation point was shifted to the sharp corner of strips. Results confirmed that the maximum power can reach up to more than 66W/m at $Re = 152,400$ and the maximum efficiency is around 20% at $Re = 80,000$ when $\theta = 20^\circ$. Besides that, the maximum power efficiency can be found at VIV upper branch and near the initial galloping consistent with the model tests in Figs. 34 and 35. The authors tested the total power density of a series of oscillator arrays, then, obtained the maximum power density (441.11W/m^3). The results

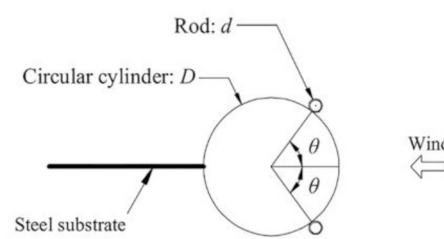
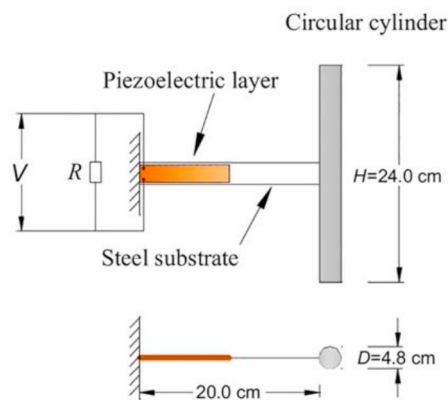


Fig. 42. Schematic of the piezoelectric energy harvester and rod attachment configuration in Ref. [103] ($L_{en} = 240$ mm; $D = 48$ mm).

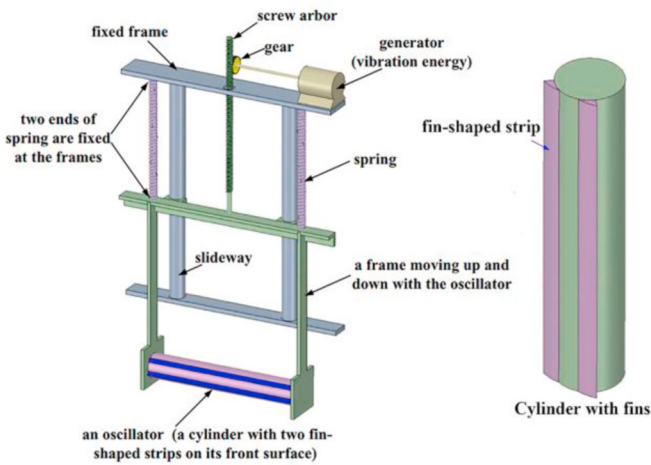


Fig. 44. Diagram of the energy harvester with a fin-shaped strip [105] ($D = 101.6$ mm; $m^* = 1.40$; $K = 1102.489$ N/m; $\zeta_{\text{harness}} = 0.075$).

indicated that these fins-shaped strips can harvest more power than that of the smooth cylinder. The power they harvested is comparable to the power harvested with up to four cylinders in tandem as calculated by Ref. [11] to be around $602\text{W}/\text{m}^3$. Notably, efficiency reached 88% of the Betz limit when four cylinders were used in tandem.

In further studies, by carrying out experiments in the same wind channel as [103], Ref. [106] analyzed the piezoelectric energy harvesting from the transverse galloping of a square oscillator (total length of $L_{\text{en}} = 240$ mm; side length of 24 mm) with fixed fins at its four corners in the range $0 < U < 7$ m/s. As shown in Fig. 45, the authors considered three configurations which include four corner fins, leading-edge fins, and trailing-edge fins, and compared their power-harvesting results to that of a plain square prism. It should be mentioned that this idea comes from Ref. [107]. The results verified that the effect of fin's location on the onset galloping speed is inappreciable. As shown in Fig. 46, all selected configurations can enhance the performance of an energy converter to different degrees except for the trailing-edge case. The results showed that the optimal configuration is the case in which two fins were installed at the leading-edge, which produces the maximum output voltage (14V at $U = 7$ m/s) and power-improvement ratio. Among them, the maximum improvement ratio reached up to 2.5 times corresponding to the plain square when the wind velocity is around 2 m/s.

On the basis of the above studies for the wind-energy-harvester, in Ref. [108], authors introduced two pieces of thin splitter plates and fixed them on the leeward side of a circular cylinder at $0 < U < 7$ m/s. The authors explored the effect of splitter-plate length ($L_{\text{sp}} = 0.25D - 2.00D$) on the piezoelectric energy harvesting of a cylindrical oscillator in a wind tunnel (Fig. 47). It was verified that a cylinder without attached

splitter plate can harvest relatively low energy in a narrow VIV region. However, selecting an appropriate splitter length can harvest energy beyond the VIV region (by inducing galloping) and can increase the output voltage as wind velocity increases. Additionally, the optimal value ($L_{\text{sp}} = 0.65D$) can be observed in Fig. 48, which can induce a higher output voltage than that of the other cases. Nevertheless, when L_{sp} is higher than $1.25D$, the output voltage obviously decreased.

In [109], authors used the same passive control method as [108] to explore the transverse galloping performance of the cylindrical oscillator in a water tunnel at $1500 \leq Re \leq 16,000$. Besides splitter length, plate porosity was also considered as an interference parameter. As shown in Fig. 49, the study can fall into three categories: solid splitter plates with length of $0.5D$ and $1.0D$; slotted splitter plates with length of $1.0D$. The results showed that compared to the plain cylinder, the cases of solid splitter plates can convert more hydrodynamic power into the oscillator's motion. Furthermore, in the case of slotted splitter plates, lower energy can be harvested than in the case of solid plates. Adding the slots induces an increase for drag force, however, results in a decrease of pressure difference. The other research involving the splitter plate can be found in Ref. [110].

The passive control methods of energy harvesting above mainly focused on adding fixed appendages on an FIO-based CEC. However, in some research, the passive appendage is a free-to-rotate impeller which has a rotation shaft that is collinear to the cylindrical axis. It should be noted that the rotation of impeller does not require external energy input, but is caused by the flow field. As reviewed next, the energy harvesting can be greatly improved by combining the vibration of the cylindrical oscillator and the rotation of the impeller considered as a turbine.

In 2016 [111], numerically analyzed the VIV characteristics of a cylinder with a free-to-rotate dartlike overlay. Results indicated that utilizing this dartlike overlay is conducive to harvesting energy at higher incoming flow velocity. Based on this significant-conclusion, in 2017, a new passive-control energy harvester that can satisfy both vibration reduction and energy acquisition was presented in Ref. [112]. The authors installed some free-to-rotate impellers on a bare circular marine riser (called combination cylinder) and used a numerical method to study the power harvesting and VIV characteristics of the harvester at $30,512 < Re < 488,567$, as shown in Fig. 50. Being analogous to the bare cylinder, the variation of amplitude with incoming flow velocity for the combination cylinder first rises and later decreases. However, the onset velocity of the synchronization region of this combination cylinder is higher compared to the bare cylinder. It was found that the variation of power harvesting with the flow velocity shows an exponential increase, and the maximum power harvesting can increase up to $283.27\text{W}/\text{m}$ at $U^* = 13.13$. Consequently, the phenomenon of low vibration and high energy-harvesting can happen at $U^* \geq 9.85$.

In [113], authors numerically studied the hydrokinetic power

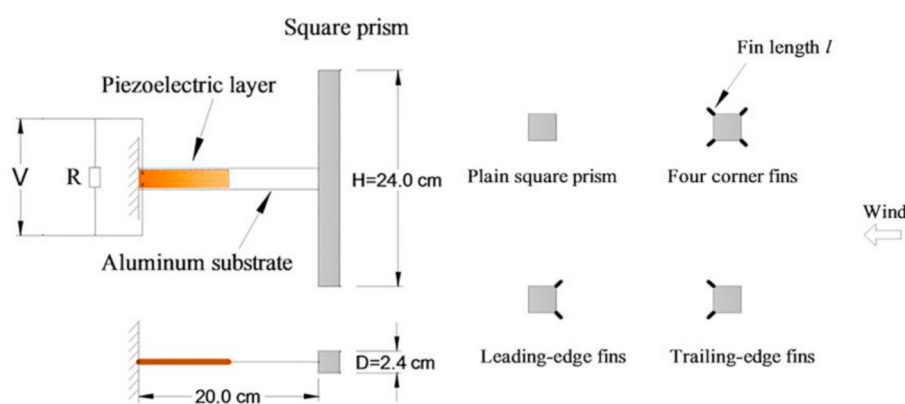


Fig. 45. Schematic of the piezoelectric energy harvester and different fin configurations in Ref. [106] ($L_{\text{en}} = 240$ mm; $D = 24$ mm).

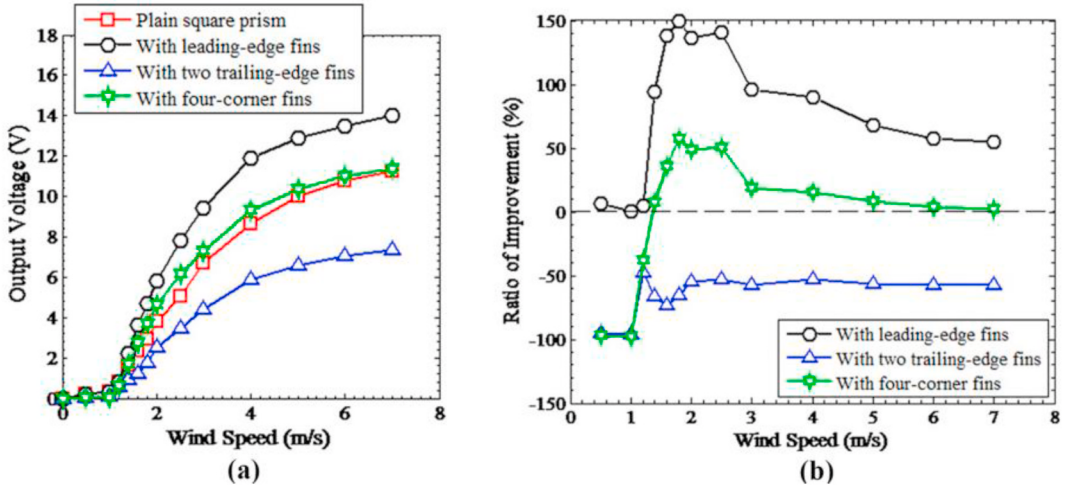


Fig. 46. Power harvesting performance vs. wind speed: (a) Output voltage of four configurations; (b) Ratio of power-harvesting improvement of three configurations [106].

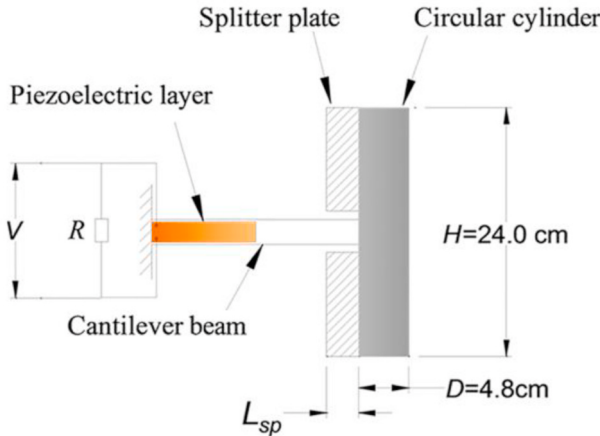


Fig. 47. Schematic of the energy harvester with two splitter plates in Ref. [108] ($L_{en} = 240\text{ mm}$; $D = 48\text{ mm}$).

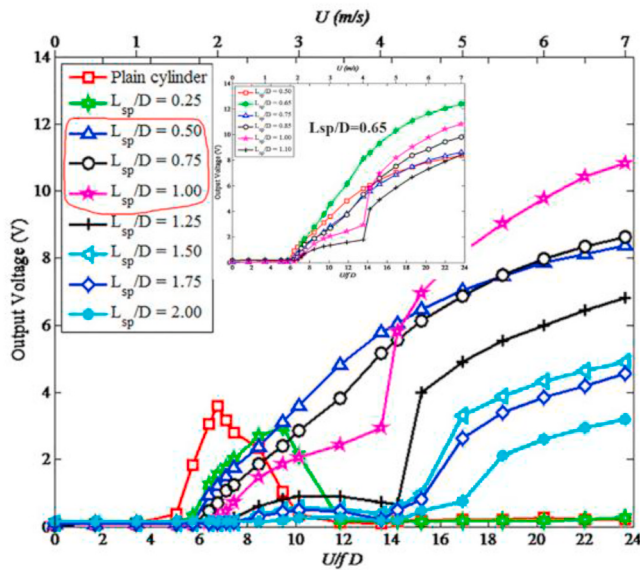


Fig. 48. Output voltage for different normalized length L_{sp}/D [108] ($L_{en} = 240\text{ mm}$; $D = 48\text{ mm}$).

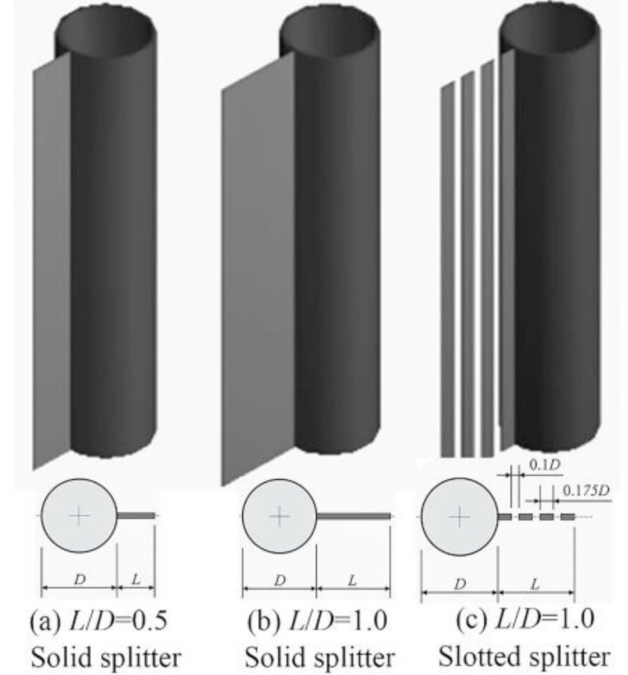


Fig. 49. Geometric parameters of tested devices in Ref. [109] (Wet length of 650 mm; $D = 50\text{ mm}$).

harvesting from the VIV of a bare cylinder with a free-to-rotate pentagram impeller at $14,000 < Re < 80,000$. As shown in Fig. 51, this combination energy harvester has two generators and can obtain energy from the rotation of the impeller. The oscillating amplitude of the energy harvester showed an upward trend as reduced velocity increased. In addition, compared with a bare cylinder, the combination converter has a higher amplitude in in-line vibration direction, however, has a lower value in transverse direction (corresponding to the incoming flow). As might have been expected, at high incoming flow velocity, the power-converting obviously increases due to the hydrodynamic instability induced by introducing the impeller. The results concluded that the average power efficiency for the combination converter reaches around 22.6%, moreover, the total power density of these staggered cylinders ($5D \times 5D$, $D = 38.1\text{ mm}$) can reach up to 885.53W/m^3 ($\zeta_{harness} = 0.031374$).

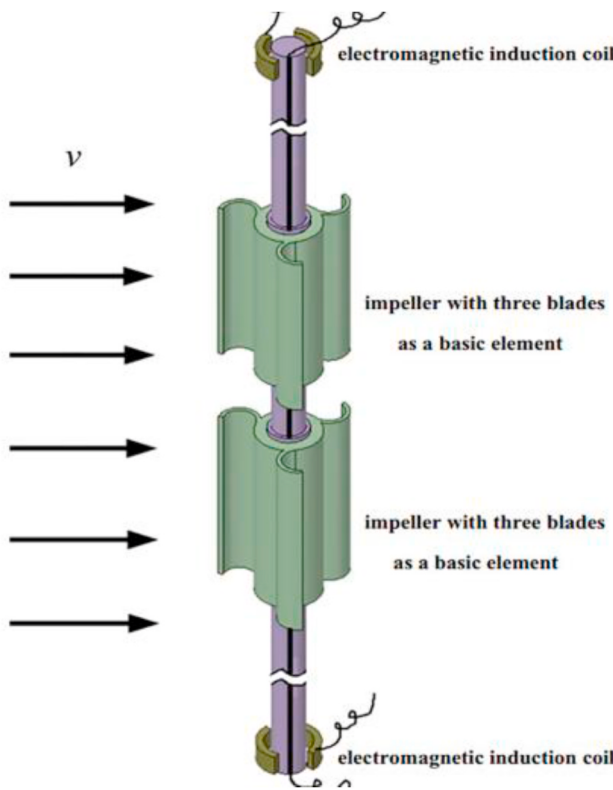


Fig. 50. Marine riser attached by free-to-rotate blades in Ref. [112] (Cylinder: $D = 305$ mm; $m^* = 4.57$; Blades: radius of 0.25D).

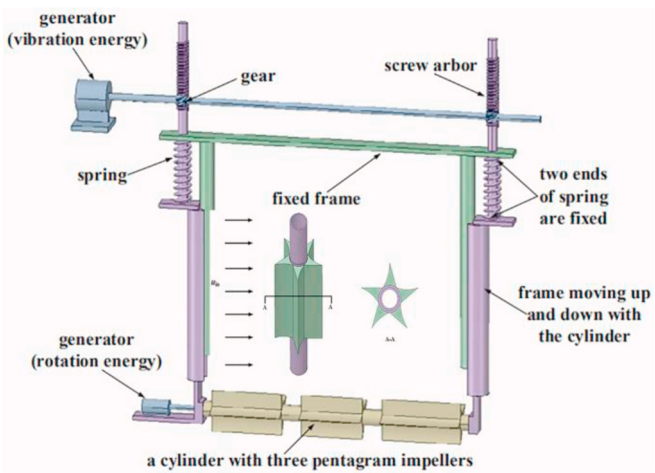


Fig. 51. Schematic of a converter with three pentagram impellers [113] (Cylinder: $D = 38.1$ mm; $K = 34,156.3$ N/m; $\zeta_{\text{structure}} = 0.001456$; Pentagram impeller: height of 9D).

As analyzed above, a bare circular cylinder with appendages, such as PTC, tripping wires, cylindrical rods, fins, or impellers, can harvest more power under certain conditions than that of a smooth cylinder. Specifically, appendages trigger galloping, which results in increased amplitude albeit reduced frequency of oscillation. As shown in Figs. 34 and 35, the efficiency in galloping is significantly reduced compared to VIV. Thus, a converter has two local optimal designs which would become global depending on the space constraint. In a non-active space constraint, optimal power would be beneficial and the CEC would operate in galloping at the maximum available speed. In a limited space, the global optimum would be based on efficiency and the CEC would be

operating at the onset of VIV. A summary of the review in this section, regarding energy extraction via transverse VIV or galloping for different appendages on the oscillator, is presented in Table 3. It should be pointed out that the maximum power in Table 3 represents the power per unit length of cylinder.

Passive turbulence control of FIO and its impact on VIV and galloping, were reviewed in this section. Changing the surface roughness by applying sand-strips, placing different shaped rods or fin-shaped strips results in geometric asymmetry which, in turn, induces galloping. The FIO synchronization range widens and the increase of the maximum amplitude due to merging of the VIV and galloping ranges. A combination of FIV with impellers was also studied. In summary, the cylinder with PTC reaches its highest efficiency of 44% and harnessed power of 25.7W in the experimental study, which exhibits good performance in both single and tandem cylinders. For four cylinders in tandem efficiency reaches 88% of the Betz limit. The fin-shaped strips-cylinder reaches its highest harness power of 66W numerically with corresponding efficiency of 20% at higher velocity. Other parameters, for instance, stiffness, damping, and mass ratio, can be changed systematically to narrow the region between the VIV-galloping transition, thus, overlapping or overtaking the VIV regions in a smooth cylinder converter.

5. Position-based nonlinear stiffness

Recently, so as to improve the harvested power or converted efficiency for oscillation cylinders, a new experimental scheme [12,21,22], has been developed employing nonlinear spring-stiffness based on the oscillator's position. The oscillation direction is transverse to the incoming flow. Selected cylinder has selectively distributed surface roughness as passive turbulence control (Section 4). Obviously, this transverse FIO includes VIV and galloping since there is PTC. Physical experiments were all conducted in the LTFSW Channel of the MRELab of the Michigan University by introducing the VIVACE Converter [5,19]. In Refs. [21,22], authors analyzed the results of the oscillation amplitude, oscillation frequency, harvested power and harvesting efficiency. As mentioned in Section 3.1, the power and efficiency can be expressed by Eqs. (10) and (12), respectively. It should be emphasized that ζ_{harness} is the harnessing damping ratio, which for linear oscillators provides the mechanism only of energy transfer from the external excitation due to the hydrodynamic force to the cylinder motion. The mechanical energy for oscillator is then converted into harvested electrical energy for generator. This feature was realized by the second generation of the virtual spring-damping system (Vck) [28]. Especially, this Vck including the servomotor has been used to simulate the linear viscous damping c_{virtual} or nonlinear spring stiffness or compensate for the nonlinear damping of the system (Fig. 52-a). The position and the velocity of oscillating cylinder are traced by the servomotor's encoder, as shown in Fig. 52-b. The control principle of this Vck system can be found in Fig. 53. More details of the Vck can be found in Ref. [28]. Finally, the equation of motion, which adds the nonlinear stiffness feature, can be written as:

$$m_{\text{osc}}\ddot{y} + c_{\text{virtual}}\dot{y} + F_{\text{restoring-force}}y = F_{\text{Fluid}} \quad (17)$$

where $F_{\text{restoring-force}}$ represents the restoring force, respectively. It should be noted that the restoring force is changed with the displacement variation of a cylinder, which emulates the nonlinear spring characteristics.

In [12], authors conducted experiments to investigate a single cylinder with nonlinear (adaptive piecewise-linear) spring stiffness in the cases of $K_1 = 200$ N/m and $K_2 = 1,000$ N/m at $24,000 < Re < 120,000$ (Fig. 54-a). The mathematical expression for these curves can be written as:

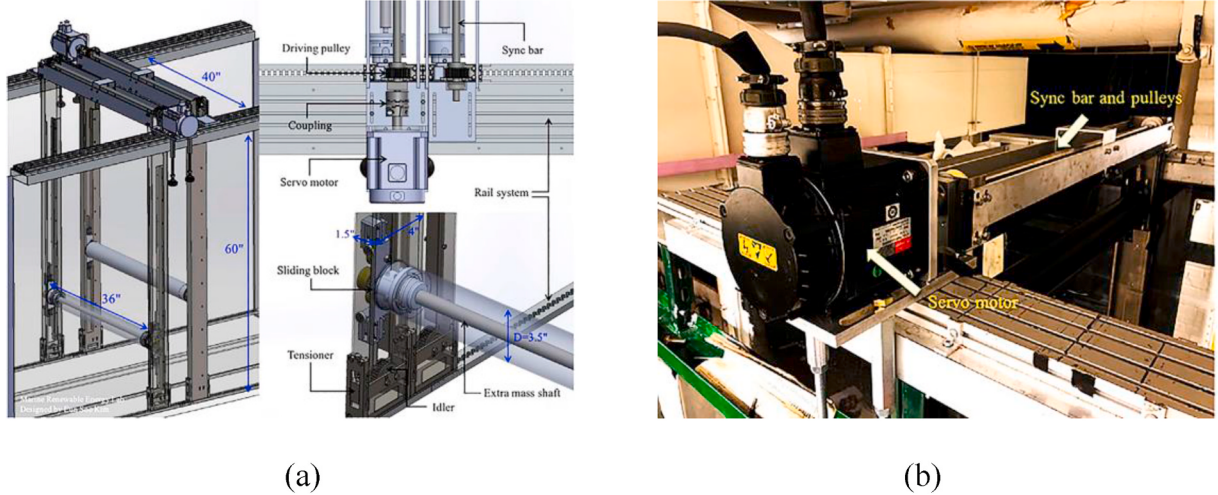


Fig. 52. Installation of a VIVACE Converter and Vck controller: (a) 3D assembly drawing of the device; (b) Picture of the servomotor of the Vck system [22].

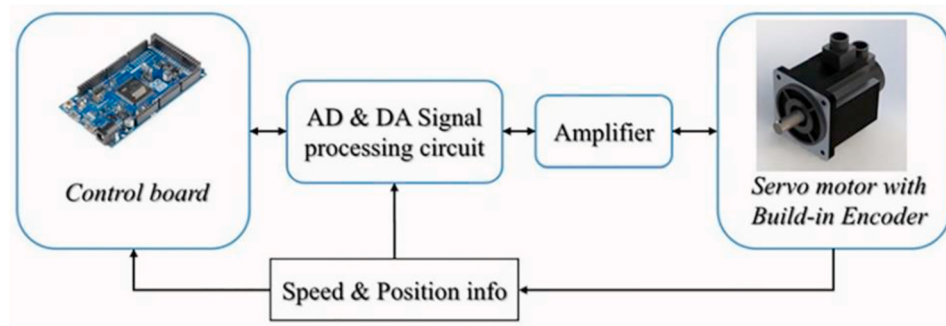


Fig. 53. Schematic of the control principle for the Vck system [22].

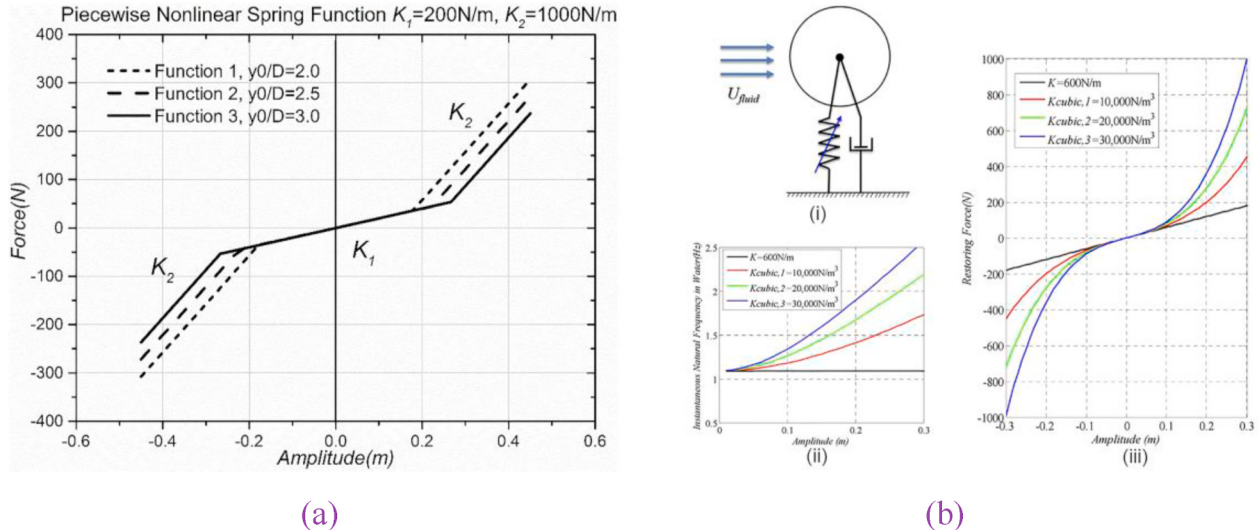


Fig. 54. Diagram of nonlinear stiffness functions: (a) Nonlinear piecewise stiffness functions with $y_0/D = 2.0, 2.5$ and 3.0 , $K_1 = 200 \text{ N/m}$, $K_2 = 1,000 \text{ N/m}$ ($D = 88.9 \text{ mm}$; $L_{en} = 895.223 \text{ mm}$; $m^* = 1.343$; $\zeta_{harness} = 0.13, 0.26, 0.39, 0.53$). (b) Cubic stiffness parameter $K_{cubic,n}$: (i) Physical model of the oscillator. (ii) Restoring force versus amplitude. (iii) Vacuum natural frequency versus amplitude ($D = 88.9 \text{ mm}$; $L_{en} = 895.223 \text{ mm}$; $m^* = 1.343$; $\zeta_{harness} = 0.13, 0.26, 0.39, 0.53$) [12,22].

$$F_{restoring-force} = \begin{cases} K_1 \times y, & \text{if } |y| \leq y_0 \\ K_1 \times y_0 + K_2 \times (y - y_0), & \text{if } |y| > y_0 \end{cases} \quad (18)$$

where K_1 and K_2 are the two spring stiffness values before and after location y_0 , respectively. It was found that the nonlinear energy

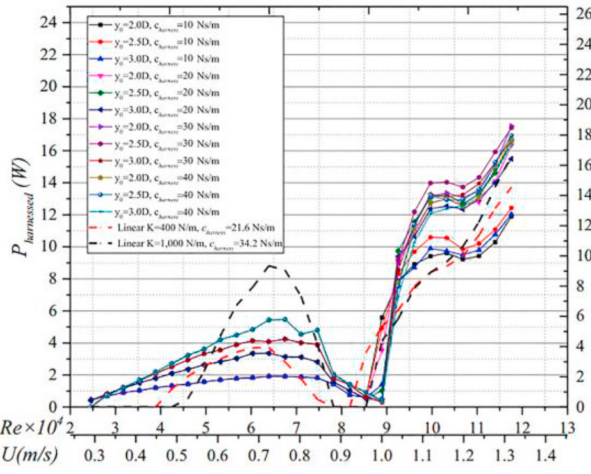
converter can harvest more energy than that of the linear converter in the cases of $y_0/D = 2.0, 2.5$ and 3.0 within a certain flow velocity range. The nonlinear case can harvest energy in the VIV-galloping transition region, indicating that the energy will be harvested across the entire velocity range. The results indicated that the initial velocity (which

drops down to 0.275 m/s) of the FIO in the nonlinear case is lower than that of the linear one, meaning that a broader velocity range of energy harvesting was achieved. In addition, at the onset galloping, this nonlinear oscillator can has efficiency 1.76 times the efficiency of the linear spring oscillator. As flow velocity further increases, the difference narrowed to 1.15 times. Results confirmed that one local optimum of energy harvested occurs in VIV at the end of upper branch and another local optimal value occurs at the maximum permissible velocity in galloping due to facility limitations. As shown in Fig. 55-a, this second local optimal value is also the global optimum and is: $P_{max} = 17.55W$ at $Re = 120,000$ when $y_0/D = 2.0$ and $\zeta_{harness} = 0.39$. On the contrary, as pointed out in Figs. 34 and 35, the local efficiency optima are located at the beginning (rather than the end) of the VIV and galloping ranges and the global optimum is the VIV local optimum rather than the galloping local optimum. However, at VIV region, the harvested power for nonlinear spring converter is lower compared to that of the linear spring converter.

To study the effects of the different values of y_0/D and the different distributions of the nonlinear piecewise stiffness, the case of $y_0/D = 0.5, 1.0, 1.5$ and $K_1 = 1,000 \text{ N/m}$ and $K_2 = 200 \text{ N/m}$ have been considered in Ref. [21] for $24,000 < Re < 120,000$. The experimental data showed a similar result as in their previous work [12]. Further, the nonlinear piecewise spring stiffness can harvest higher hydrodynamic power compared with the linear-spring oscillator. The maximum power of 18.8W occurred at $Re = 120,000$ when $y_0/D = 0.5$ and $\zeta_{harness} = 0.39$. The maximum efficiency was around 23.5% in the VIV region, which is higher than 17.4% achieved by the linear stiffness oscillator ($K = 1,000 \text{ N/m}$; $c_{harness} = 34.2 \text{ N/m}$) at the same velocity. So, in this case a higher peak value of energy harvesting was achieved than that of the previous article in the VIV region and at the end of galloping (Fig. 55-b). In addition, the initial velocity of the FIO becomes larger than that of the previous article due to the fact that the larger value of K_1 requires higher force and, thus, higher flow speed to initiate FIO.

The above analysis [12,21] showed that different values of y_0/D and nonlinear piecewise stiffness will produce different harvested energy. Therefore, this method can be applied to investigate further how to obtain more energy harnessing and achieve higher efficiency. A key factor here is whether the piecewise linear spring is soft and then hard or vice-versa. This provides flexibility to design a CEC according to the flow speed and the topology (space) constraints.

Further, in Ref. [22], authors implemented experimentally a cubic restoring force at $3 \times 10^4 < Re < 1.2 \times 10^5$ for hydrokinetic energy



(a)

acquisition by utilizing FIO of PTC-cylinder (Fig. 54-b). The equations of the spring stiffness curves can be expressed as:

$$F_{restoring-force} = Ky + K_{cubic,n}y^3, n = 1, 2, 3 \quad (19)$$

For the linear term in Eq. (19), a lower value of K (i.e.: 600 N/m) was utilized to lower the initial velocity for energy harvesting. The cubic nonlinear term (i.e.: $K_{cubic,1} = 10,000 \text{ N/m}^3$, $K_{cubic,2} = 20,000 \text{ N/m}^3$, $K_{cubic,3} = 30,000 \text{ N/m}^3$) was helpful in eliminating the gap between VIV and galloping. That gap is defined as a velocity region where hydrokinetic energy cannot be harvested because the onset of galloping is after the end VIV synchronization range. The stronger the nonlinearity, the higher the harvested power in the upper branches of VIV. In Fig. 54-b, for the cubic nonlinear oscillator, increasing the oscillation amplitude is followed by an increase of $f_{n,water}$. Therefore, in galloping, the cubic nonlinearity is beneficial to energy harvesting whether the harnessing damping is high or low. The maximum power of 22W occurs at $Re = 120,000$ when $K_{cubic,3} = 30,000 \text{ N/m}^3$ and $\zeta_{harness} = 0.39$, which is higher

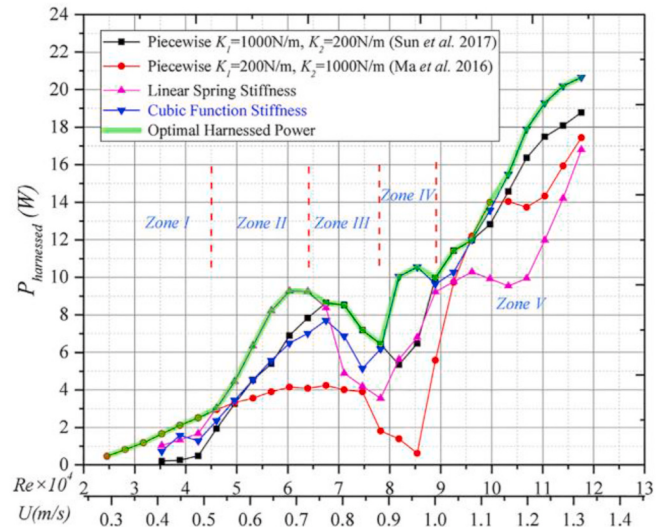
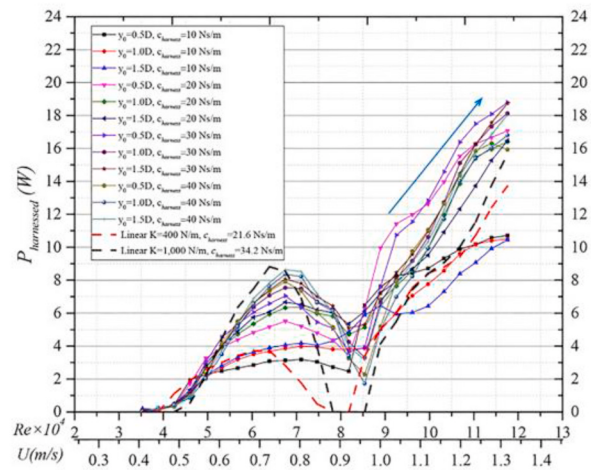


Fig. 56. Power envelope of linear, nonlinear piecewise and nonlinear cubic spring-stiffness for single-cylinder converter [22] ($D = 88.9 \text{ mm}$; $L_{en} = 895.223 \text{ mm}$; $m^* = 1.343$; $\zeta_{harness} = 0.13, 0.26, 0.39, 0.53$).



(b)

Fig. 55. Harvested power with nonlinear piecewise stiffness compared with linear stiffness: (a) Nonlinear piecewise stiffness functions with $y_0/D = 2.0, 2.5$ and 3.0 , $K_1 = 200 \text{ N/m}$, $K_2 = 1,000 \text{ N/m}$ ($D = 88.9 \text{ mm}$; $L_{en} = 895.223 \text{ mm}$; $m^* = 1.343$; $\zeta_{harness} = 0.13, 0.26, 0.39, 0.53$). (b) Nonlinear piecewise stiffness functions with $y_0/D = 0.5, 1.0$ and 1.5 , $K_1 = 1,000 \text{ N/m}$, $K_2 = 200 \text{ N/m}$ ($D = 88.9 \text{ mm}$; $L_{en} = 895.223 \text{ mm}$; $m^* = 1.343$; $\zeta_{harness} = 0.13, 0.26, 0.39, 0.53$) [12,21].

than the linear stiffness ($K = 1,000 \text{ N/m}$; $c_{\text{harness}} = 34.2 \text{ N/m}$) of 15.3W at the same velocity. The maximum efficiency achieved was around 40%, which occurred in the VIV region. Fig. 56 shows that, the harnessed power in the cubic nonlinear cases was compared with that of the linear and piecewise linear cases. Results indicated that, in each velocity range, the overall local optimum is provided by a different model. For example, in galloping, the cubic nonlinear stiffness has a better performance of power harnessing than that of the other stiffness cases.

Fig. 56 presents that in the upper VIV breach, adding the nonlinear stiffness has negative effect on energy harvesting comparing to the linear stiffness case. However, in the transition and galloping regions, the nonlinear piecewise stiffness and cubic nonlinear stiffness can harvest higher energy than that of the linear spring case. Therefore, it is useful to introduce nonlinear stiffness which is adaptive to the position of oscillating cylinder.

Furthermore, based on research on a single-cylinder, the FIO phenomenon of two tandem cylinders which have the same relation between the nonlinear spring force and the oscillation displacement as Eq. (18) (i.e.: $K_1 = 200 \text{ N/m}$; $K_2 = 1,000 \text{ N/m}$; $y_0/D = 2.5$) was investigated experimentally for $24,000 < Re < 120,000$ [114]. It was found that the initial velocity of FIO was 0.33 m/s, which is higher than that of the single oscillator case under the same conditions, nevertheless, lower than the linear stiffness case. In galloping, the results showed that the nonlinear spring case can obtain more power than that of the linear spring case.

Different from the above investigations, a considerable number of scholars proposed to study the harnessed energy by utilizing VIV rather than galloping, as analyzed below.

In 2017 [115], used an upright VIV-based piezoelectric energy harvester to explore its power output and its width of synchronization region by adding a nonlinear magnetic force realized by two magnets with same polarity in range of $0 < U < 6 \text{ m/s}$. Fig. 57 shows, the experimental setup placed in the incoming wind. The two controllable parameters Δx and Δy were, respectively, the horizontal and vertical distance between two magnets. The optimal load resistance was around $500 \text{ k}\Omega$ for harvesting more output power. It was demonstrated that changing Δx and Δy was accompanied by a variation of the oscillator's natural frequency, indicating that the width of synchronization region would change with it. The maximum power of $140 \mu\text{W}$ occurred at $U = 2.5 \text{ m/s}$ when $\Delta x = 10 \text{ mm}$ and $\Delta y = 5 \text{ mm}$. As expected, due to the nonlinear magnetic forces, this energy harvester was proved to harvest higher peak power (increase rate of 29%) and realize wider range of synchronization (increment of 138%) than that of the case without adding the magnets.

To enhance energy harvesting and broaden the synchronization

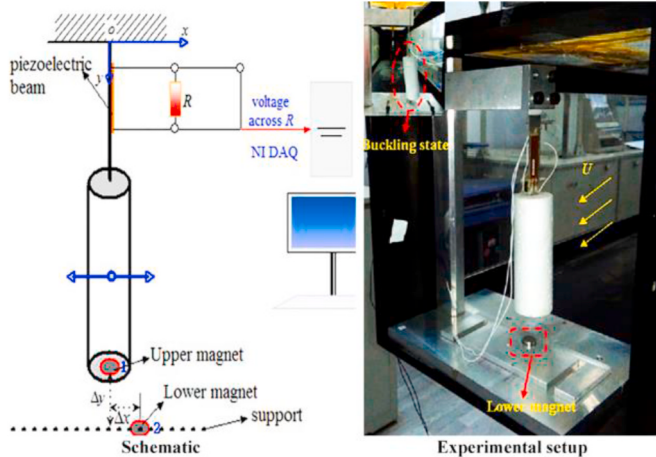


Fig. 57. Schematic of the upright energy harvesting system in Ref. [115] ($L_{\text{en}} = 92 \text{ mm}$; $D = 30 \text{ mm}$; $\Delta x = 0, 10, 20 \text{ mm}$; $\Delta y = 5, 10, 15 \text{ mm}$).

region, a similar research as [115] was investigated by adding nonlinear attractive magnetic forces realized by two pairs of symmetric magnets [116]. Fig. 58 shows the schematic of VIV-based piezo-magneto-elastic energy harvester which was simulated by a distributed-parameter model. In addition, the cylindrical lift force induced by VIV and the nonlinear magnetic forces were modeled simulated by a modified van der Pol equation and a dipole-dipole interaction, respectively. The authors mainly explored the influence of vertical spacing between two magnets or external load resistance for power harvesting performance, coupled frequency and the range of the synchronization regime. The results showed that selecting the appropriate values of vertical spacing and load resistance can improve the performance of the hydrokinetic energy device. Besides that, under the action of the nonlinear magnetic force, the synchronization region is widened and is moved to lower incoming flow velocity.

In [117,118], authors experimentally used a Cyber-Physical Fluid Dynamics Force-Feedback Technique (CPFD) to explore the impact of the nonlinear springs on VIV characteristics of the circular cylinder by adding a nonlinear restoring force at $1000 < Re < 5500$. The results showed that the oscillating amplitude and output power of these nonlinear cases (including cubic and quartic restoring force) continually increased as flow velocity increased. The maximum power was around 5.2 mW at $Re = 5500$ for quartic spring. In addition, the nonlinear case can get a smaller initial vibration velocity than that of the linear standard system, resulting in a broader range of power harvesting velocity, as shown in Fig. 59. As mentioned above, the nonlinear case can develop better performance in energy harvesting than that of the linear case, especially in the high values of Re .

In [119], authors numerically investigated the VIV response of a cylinder elastically supported by the selected cubic nonlinear spring, then, compared the vibration amplitudes and frequencies with the linear spring case. The nonlinear springs can be divided into two categories: softening spring and hardening spring. They observed that, for $60 \leq Re \leq 220$, the softening spring reduces the values of amplitude and frequency in the synchronization region. Additionally, with increasing of the nonlinearity of softening stiffness, the maximum amplitude decreases from 0.6 to 0.51. However, the hardening spring made the amplitude curve shift toward the high Re and enhanced the velocity range of oscillation response. This phenomenon was pronounced with the increase of the nonlinearity of the hardening spring. These conclusions affect energy harvesting.

[16] utilized the VIV system to harvest energy. A nonlinear spring (which is also known as hardening spring in Ref. [120]) was employed to enhance the energy harnessing by widening the range of the resonance region and increasing the oscillation amplitude. Fig. 60 shows the experimental model of the VIV structure, with installed additional short or long plates on the fixed support of the cantilever beams. By selecting the appropriate combination of the plate and cantilever beam, different degrees of the nonlinear spring stiffness can be achieved, including the slight nonlinear spring (close to linear spring), low hardening spring (with an aluminum beam and a short plate), high hardening spring (which has the aluminum beam and long plate) and strong nonlinear spring (which has the aluminum alloy beam and long plate). The results indicated that a hardening spring has better performance of energy harvesting than that of the linear spring.

Some energy harvesting researches involving nonlinear stiffness were realized by using a wake oscillator model, as shown in Fig. 61. The wake oscillator model was proposed in Ref. [121], and modified in Ref. [122].

For exploring vibration characteristics of a VIV energy harvester with nonlinear springs, author in Ref. [17] applied the cases of bi-stable stiffness, hardening stiffness, and their combined nonlinear stiffness to analyze the oscillation amplitude of cylinder and energy harvesting compared to the linear stiffness case. The wake oscillator model was used to numerically investigate energy harvesting. A computer-based force-feedback testing platform, which had same principle as [15,18],

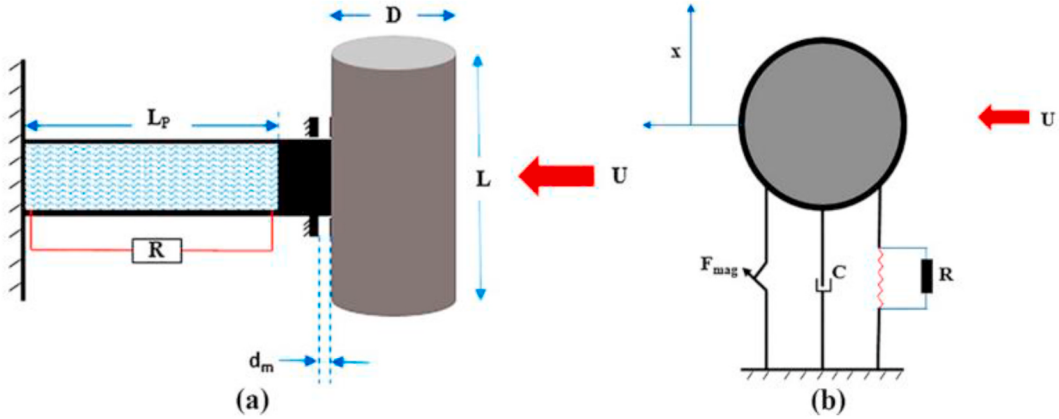


Fig. 58. Schematic of the piezo-magneto-elastic energy harvesting system in Ref. [116]: (a) VIV energy harvester; (b) spring-mass damper piezoelectric energy harvester (Cylinder: $L_{en} = 200$ mm; $D = 50$ mm; $m = 0.05$ kg).

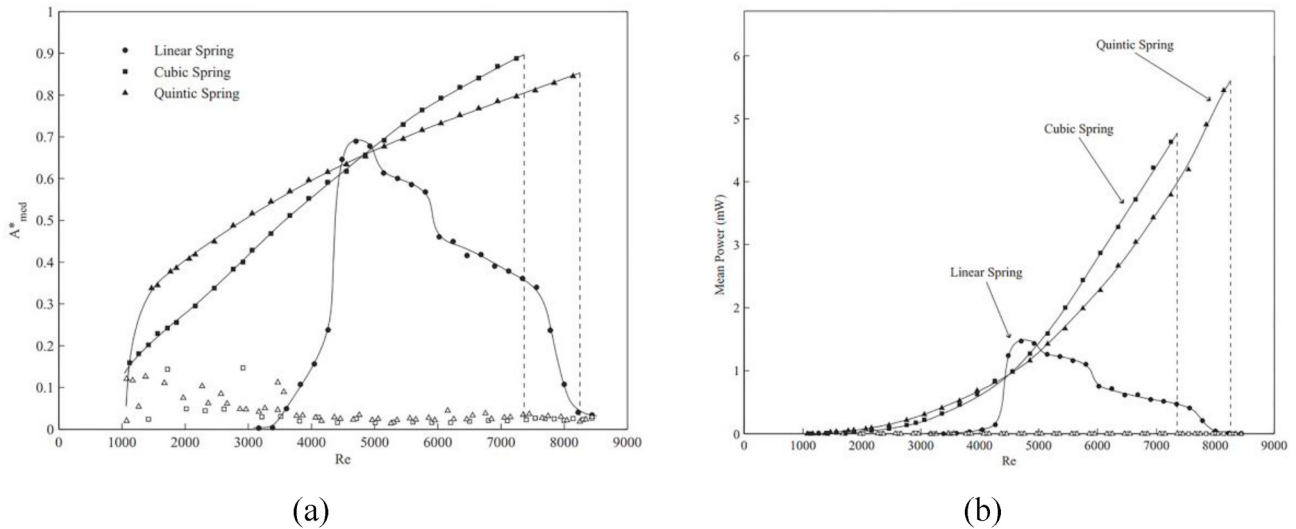


Fig. 59. VIV response using linear, cubic and quartic springs vs. Re : (a) Amplitude response. (b) Mean power output [118] ($m^* = 8.82$; $\zeta = 0.0013$).

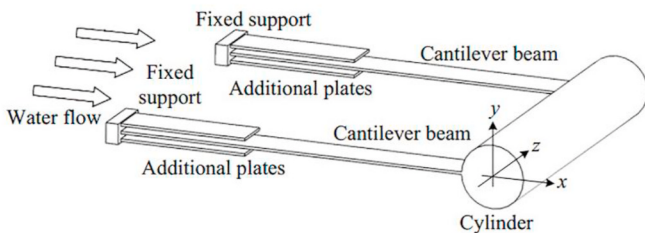


Fig. 60. Schematic of the experimental model of the VIV structure with added hardening spring [16] ($L_{en} = 250$ mm; $D = 50$ mm).

was used to verify the numerical results, as shown in Fig. 61. Fig. 62 shows the different spring mechanisms. It also shows the variation trend for restoring force with the oscillator's displacement (y) for these three stiffness cases. Results showed that the bi-stable stiffness or the piece-wise hardening stiffness have better performance in energy harnessing than that of the linear stiffness. Furthermore, the combined nonlinear stiffness, as expected, can improve the power harvesting in all flow velocities besides the end of resonance region. The detailed description of the bi-stable stiffness can be found in Ref. [123]. In addition, the hardening spring can change the resonance frequency of the energy converter. This phenomenon was modified in Ref. [124].

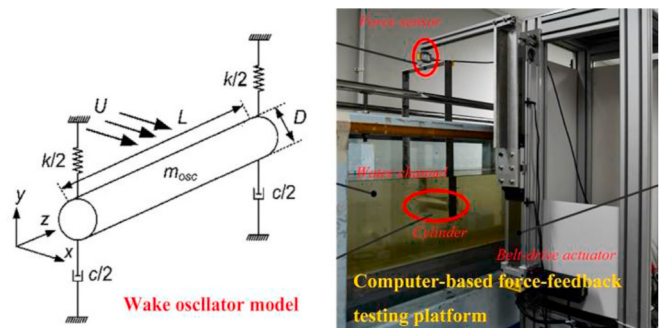


Fig. 61. Schematic of the model and experimental platform in Ref. [17].

To further study the performance of a current energy converter with bi-stable spring stiffness, authors in Ref. [125] improved the value of the bi-stable gap. Results confirmed that, at low flow velocity, the small bi-stable gap of 0.02 can only achieve a small energy increment compared to the linear spring case. However, as bi-stable gap increases to 0.2, the increment of the average energy harvesting clearly increases. At high flow velocity, the power curve declines rapidly due to the appearance of chaotic vibrations. Nevertheless, such vibrations can be weakened when the system damping increases. The same conclusion

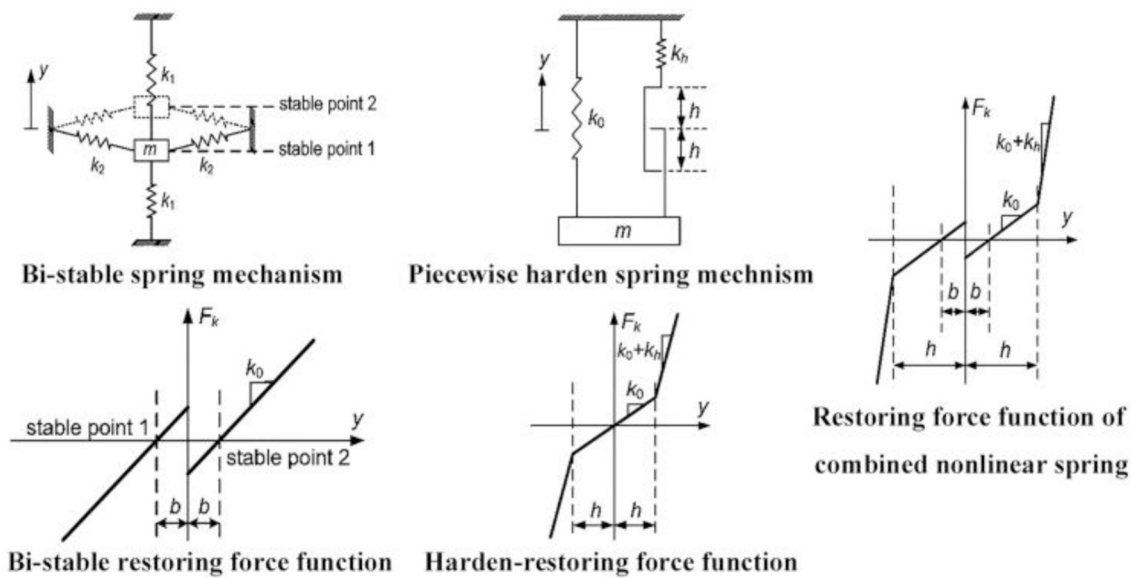


Fig. 62. Spring mechanism and restoring force function in Ref. [17].

Table 4

A comparison of energy extraction for oscillator with position-based nonlinear stiffness.

Ref.	Method	Type	<i>Re</i>	Initial speed(m/s)	<i>D</i> (mm)	<i>P</i> _{max} (W/m)	η_{max} (%)
[12]	Exp. (Water)	Linear	24,000–120,000	0.3946	88.9	15.3	—
[12]	Exp. (Water)	Nonlinear piecewise	24,000–120,000	0.275	88.9	19.6	54
[21]	Exp. (Water)	Nonlinear piecewise	24,000–120,000	0.3946	88.9	21.0	23.5
[22]	Exp. (Water)	Cubic restoring force	30,000–120,000	0.3946	88.9	24.57	40
[114]	Exp. (Water)	Nonlinear piecewise	24,000–120,000	0.33	88.9	18.42	—

was reached in Ref. [126].

A summary of studies regarding energy extraction for oscillator with position-based nonlinear stiffness is presented in Table 4. From Table 4, the nonlinear stiffness reduces the onset power-harvesting velocity and enhances the maximum harvested power compared with that of the linear stiffness under the same experimental conditions, which is consistent with the variation tendency in Fig. 56. It should be emphasized that the maximum power in Table 4 represents the power per unit length of cylinder. Besides that, the maximum power for [114] (listed in Table 4) represents the power averaged between two cylinders.

In closing this Section 5, the following observation can be made. Due to the nature of FIO, the cylinder should have a low stiffness spring so that the VIV onset velocity be low. The fact is that the higher stiffness results in higher value of $f_{n,water}$, and induces higher harvested power in the VIV upper branch. The oscillator design needs to balance the amplitude and frequency to get higher harnessed power and/or efficiency in galloping. In recent research, piecewise (both from hardware and virtual system), cubic restoring force are tested. These studies showed that the piecewise (soft-hard stiffness) oscillator achieves the lowest flow velocity power harnessed and the highest efficiency for single cylinder. The cubic restoring force converter reached higher harnessed power. The most significant achievement of the nonlinear stiffness converter is improvement in the transition region, to which some researchers refer as the bi-stable gap. Therefore, the nonlinear spring stiffness, which is selected based on the position of the oscillator, can produce a better performance than that of the linear converter in the aspects of energy harnessing and corresponding efficiency.

6. Nonlinearity due to synergistic FIO OF multiple cylinders

The studies reviewed in the previous four Sections 2–5 mainly focused on a single cylinder. However, the FIO response and energy

harnessing of multiple cylinders have different characteristics compared to those of the single-cylinder because of the mutual interference between cylinders. Interactions between cylinders are very complex, but can induce nonlinear behavior that enhances the harnessed power dramatically. This complexity arises from the interaction between boundary layers, shear layers, vortices, and cylinders. Understanding these phenomena has provided partial answer to the very important question: “Can multiple oscillators in VIV operate in close formation and not require huge distance between them as in the case of turbines?” Indeed, a positive answer results in a major reduction in the metric of power-density (power-to-volume ratio), which is the Achilles heel of all renewable energy technologies [6,11]. As we will see in this and the next section, the answer is positive and stems its effectiveness in concepts stemming from fish-school kinematics [127].

In order to further explore the effect of multiple cylinders in FIO and harvested power, two subsections are presented below, where some pivotal parameters such as spacing ratio (*L/D*), spring stiffness, and harnessing damping are changed. In addition, the downstream distance between two tandem cylinders was defined as *L*. Sections 6.1 and 6.2 review studies on two-cylinder and three or four cylinders, respectively.

6.1. Two-cylinder configuration

An experimental study of FIV/O for two tandem circular cylinders was investigated for $2.86 \times 10^4 < Re < 1.14 \times 10^5$ [128]. The two cylinders had the same mass ratio and cylinder diameter. The authors selected the spacing ratio *L/D* as the key parameter and tested four values: 1.57, 2.57, 3.57, and 4.57. The results showed that for all spacing cases except *L/D* = 1.57, corresponding FIO response for upstream cylinder, including vibration amplitudes and frequencies, have nearly the same value as an isolated cylinder for reduced velocity less than 12. For all spacing ratios, the effect of upstream cylinder for downstream

one is significant, especially impacting its vibration amplitude. The maximum amplitude of the upstream cylinder and downstream cylinder when $L/D = 1.57$ were, respectively, $1.41D$ and $1.71D$. Both have higher amplitude compared with a single cylinder (around $1.20D$). These results show higher values than those of previous studies [129,130].

In 2013, a 2-D URANS method was employed in Ref. [93] to investigate numerically the FIO characteristics of two rough rigid tandem cylinders in the range $3 \times 10^4 < Re < 1.05 \times 10^5$. These numerical simulations were verified by the corresponding results of experiment which were conducted in the MRELab at the University of Michigan. It was demonstrated that the discrepancies of vibration amplitude and frequency between the 2-D URANS method and experimental method were negligible. The results showed that with increasing Re , the amplitudes of two cylinders increased. Further, the oscillating frequency of the cylinder has close value comparing with its natural frequency in water within the selected velocity range. The amplitude and frequency responses ensure the stability of oscillation, indicating that it is conducive to energy acquisition. On the contrary [131,132], show the effects of PTC and spacing ratio of two tandem cylinders on FIO suppression response at $30,000 < Re < 120,000$.

In [11,92], authors studied two tandem cylinders and enhanced their oscillation using PTC to generate more power than an isolated cylinder. Additionally, another study utilized the wake galloping of a piezoelectric energy harvester with two tandem cylinders to convert the aerodynamic energy to electrical energy for wind velocity lower than 10 m/s , as shown in Fig. 63 [133]. It should be noted that the authors fixed the upstream cylinder on a position, however, induced a transverse oscillation for downstream cylinder on a fixed slide rail. The author analyzed the effect of spacing ratio L/D on the maximum voltage. It was stated that for all spacing ratios, increasing the incoming wind velocity was followed by an increase in maximum voltage. The maximum voltage was around 38 mV at $U = 10\text{ m/s}$ for $L/D = 1.73$. The results showed that the optimal spacing ratio was $L/D = 3.0$.

In 2013, the influence of the spacing ratio of two coupled rigid cylinders with tandem and side-by-side configuration on the FIO was investigated by using numerical simulation at $Re = 150$ (Fig. 64) [134]. The author considered the spacing ratio ($L/D = 1.5, 2, 4$ and 6) as a pivotal parameter. The results showed that the tandem arrangement has wider synchronization region and higher maximum amplitude compared to an isolated cylinder for $L/D = 4.0$ and 6.0 . In particular, as $L/D = 1.5$, the amplitude for two tandem cylinders has lower value than a single cylinder. For side-by-side configuration, the amplitude is much higher than the value of the single cylinder at the cases of $L/D = 1.5$ and 2.0 .

Besides the effect of spacing ratio, different spring stiffness and

harnessing damping were also considered by some scholars as important parameters. The spring stiffness affects the oscillator's natural frequency which is most important in defining the onset of VIV and galloping. Thus, K is considered as a key parameter to investigate the performance of power harvesting. The main studies are reviewed next.

As noted in Chapter 5, as the spacing ratio of two tandem cylinders increases in the range of $1.57\text{--}4.01$, the difference of oscillation response between the upstream cylinder and an isolated single cylinder decreases [114]. It was also found that the hydrokinetic power can be improved by adding nonlinear spring stiffness based on the Vck system. In the VIV-galloping transition region, for $L/D = 2.01, 2.57$ and 4.01 , its power harnessing decreases sharply as flow velocity increases. For $L/D = 1.57$, a similar phenomenon did not occur due to the close distance between the two cylinders in tandem. The experimental results mentioned above, also show that the two tandem circular PTC-cylinders, with the nonlinear piecewise spring stiffness, can harvest more power than that of a CEC with a single linear-stiffness cylinder. The two tandem cylinders can harvest more than 4 times the power compared to the single one.

The hydrokinetic energy conversion and FIO response for two rigid, rough, tandem circular cylinders (Fig. 65) were investigated by changing the spacing ratio ($L/D = 1.57, 2.01$ and 2.57), harnessing damping ratio ($0 < \zeta_{\text{harness}} < 0.24$), and spring stiffness ($400\text{ N/m} \leq K \leq 1,200\text{ N/m}$) [34]. The Reynolds number Re was selected in the range $3 \times 10^4 < Re < 1.2 \times 10^5$. The increase of power harnessing for upstream oscillator can reach up to 100% comparing to the output of a single oscillator. However, for the downstream cylinder, there was no evident change in power harvesting. Therefore, the interaction between two cylinders had positive influence on power harvesting. The research shows that a two-cylinder converter generates 2.6–13.5 times the power of a single one in transition region and galloping. The maxima power efficiency of two tandem cylinders reached 63% in VIV and 23% in galloping (Eq. (12)). In particular, the maximum power harvested occurs at the small spacing and higher stiffness. The higher the harnessing damping was, the higher the galloping onset velocity was. That resulted in the lowest oscillation amplitude, leading to a gap between VIV and galloping. Nevertheless, decreasing spacing was followed by a decrease in gap. As spacing ratio decreased to 1.57 , in spite of high damping, the gap was eliminated. Specifically, the proximity of the cylinders induced hydrodynamic flow asymmetry on top of the geometric asymmetry caused by the OTC resulting stronger galloping able to overcome the high damping.

Following their previous studies, authors in Ref. [135] further explored the vibration amplitude of FIO based on two rough tandem cylinders mounted in the LTFSW channel (Fig. 65). The authors set the same experimental parameters (including L/D , K , and Re) as [34]. The range for harnessing damping ratio selected was $0.02 \leq \zeta_{\text{harness}} \leq 0.26$. For the upstream cylinder, it was found that the initial oscillation velocity increased with the increasing of K ; this was expected as the oscillator natural frequency increases with K . In VIV initial branch and galloping, increasing ζ_{harness} causes a decrease in amplitude for all spacing ratios and spring stiffness values. The results showed that compared with a single cylinder, corresponding maximum amplitude increment of the upstream cylinder can reach up to 30% in VIV and up to 60% in galloping. For the downstream cylinder, the oscillation is complex owing to the action of the wake of upstream cylinder. However, its maximum amplitude increase reached up to 60% with respect to the single cylinder. Therefore, under the selected parameters, the arrangement of these two tandem cylinders can result in more beneficial conditions to harvest more hydrokinetic energy than that of an isolated single cylinder.

Being different from the tandem arrangement, two staggered rough circular cylinders were used to obtain the energy from FIO at $25,000 < Re < 120,000$ in the LTFSW channel [136,137]. Furthermore, the center-to-center spacing ratio in the flow direction was $T/D = 2.57$ and in the transverse direction was $S/D = 1.0$, as shown in Fig. 66. To explore the impact of the oscillators' stiffness or damping for hydrokinetic

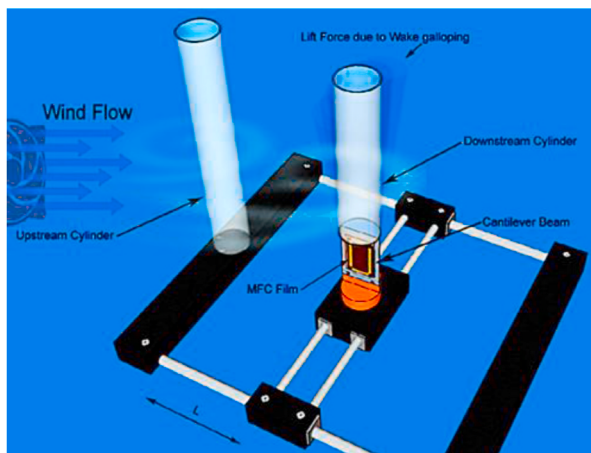


Fig. 63. Schematic diagram of the proposed system [133] (Length of upstream cylinder: $L_{en} = 250\text{ mm}$; Diameter of both cylinders: $D = 30\text{ mm}$).

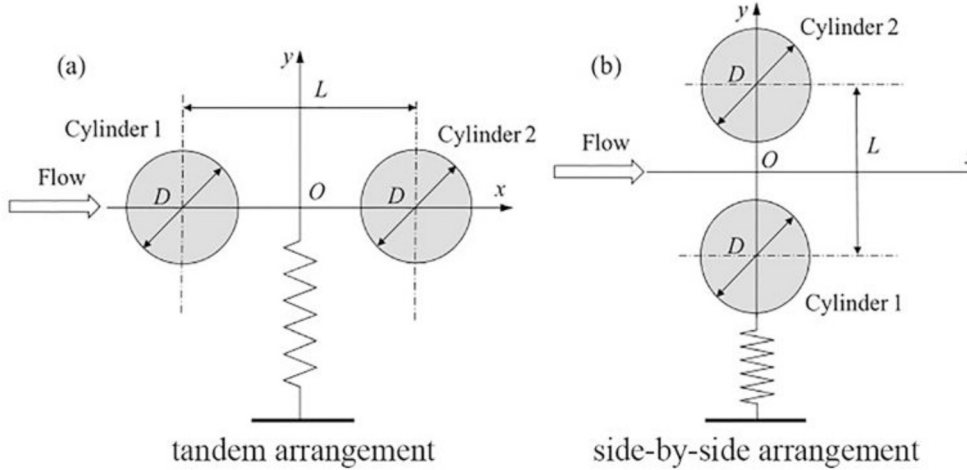


Fig. 64. Schematic of two different arrangements [134].



Fig. 65. The experimental device of tandem cylinders [34] ($L_{en} = 895$ mm; $D = 88.9$ mm; $\zeta_{harness}$: 0–0.24; $K = 400$ – $1,200$ N/m).

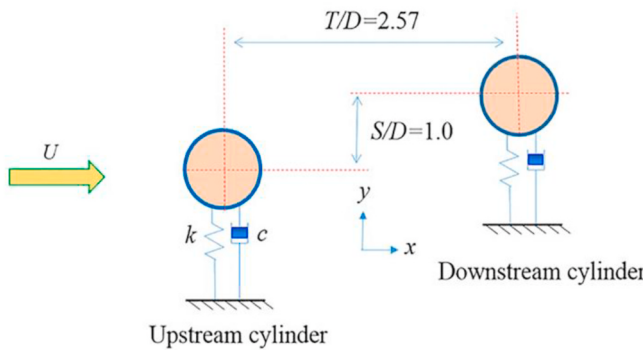


Fig. 66. Schematic of two staggered cylinders [136] ($L_{en} = 895$ mm; $D = 88.9$ mm; $\zeta_{harness}$: 0.04, 0.12, 0.24; $K = 400$ – $1,200$ N/m; $T/D = 2.57$; $S/D = 1.0$).

power conversion, the controlling parameters were selected including the harnessing damping ($\zeta_{harness} = 0.04, 0.12, 0.24$) and spring stiffness ($K = 400, 800, 1,200$ N/m). The maximum power harvested by staggered cylinders was around 28W at $Re = 120,000$ for $K = 800$ N/m, $\zeta_{harness} = 0.24$. To make a comparison with the single rough cylinder, the data in Ref. [55] were used. For a given value of stiffness, the lowest $\zeta_{harness}$ resulted in the lowest power harvested, as shown in Fig. 67. As expected, the upstream cylinder can generate higher power than that of the single cylinder case. Nevertheless, the difference of power

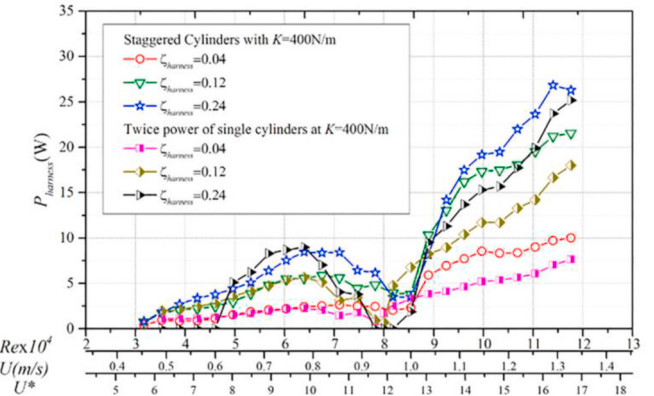


Fig. 67. Total power harvesting by two staggered cylinders for a series of selected damping ratios for $K = 400$ N/m [136] ($T/D = 2.57$; $S/D = 1.0$; $L_{en} = 895$ mm; $D = 88.9$ mm; $\zeta_{harness}$: 0.04, 0.12, 0.24; $K = 400$ – $1,200$ N/m).

harvesting between downstream cylinder and the single case was small. The results showed that total harvested power by two staggered cylinders was higher than twice of the single cylinder when $K = 400$ N/m. With increasing K , the power harvesting difference between upstream cylinder and downstream cylinder decreased.

Besides considering the spacing ratio, the cross-section shape of oscillators was also considered as an important parameter, as we can see in the following studies:

As mentioned in Section 3, in Ref. [81], authors adopted two-dimensional numerical simulations to investigate the VIV energy harvesting by two tandem cylinders with five different cross-section shapes for a series of L/D varying from 2 to 50. It was found that, as $L/D < 5$, the amplitude for upstream cylinder is obviously smaller than the value of larger spacing cases. For $L/D < 35$, compared with the oscillating amplitude of downstream cylinder, the upstream one has a higher value because of the wake flow influence between them. For $L/D > 35$, this difference is greatly reduced. It was verified that the Cir-Tria oscillator obtained higher maximum power efficiency (26.5%) than that of the other different cross-section cases, as shown in Fig. 68. Therefore, Cir-Tria oscillator becomes the optimal oscillator. The square oscillator is the case that harvests the lowest energy than that of all the other cases.

To further analyze the influence of the downstream cylinder on the performance of the aerodynamic piezoelectric energy converter, four interference cylinders with different sections (i.e.: Square, Circular,

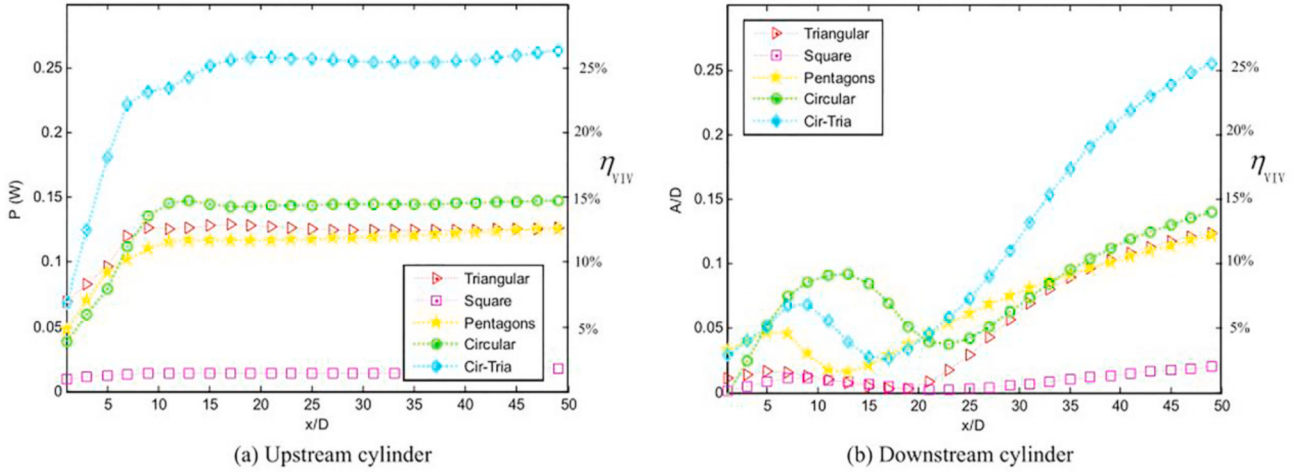


Fig. 68. The diagrams of VIV energy harnessing and efficiency of all section cases [81] ($m^* = 0.93$, $K = 76.5$ N/m, $D = 32$ mm).

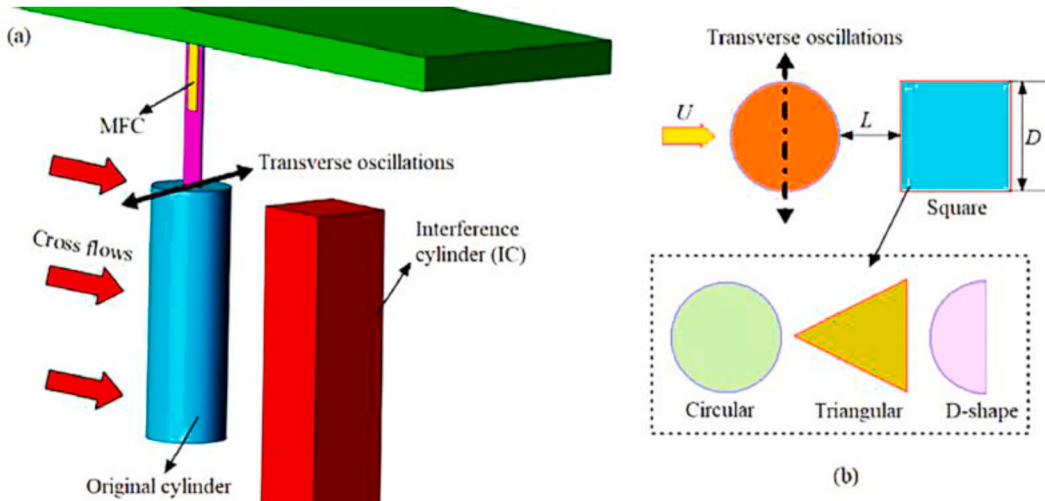


Fig. 69. Schematic for VIV power harvesting model: (a) front view; (b) top view (flow direction left to right) [138] (Original cylinder: $L_{en} = 118$ mm, $D = 33$ mm; Interference cylinder: $L_{en} = 140$ mm, $D = 33$ mm).

Triangular, and D-shape) were proposed in Ref. [138]. It should be noted that this is a fixed-cylinder interference which is placed behind the original circular cylinder, as shown in Fig. 69. The energy harvesting was realized by the transverse oscillation of the upstream cylinder. Making a comparison with other cases, the highest average power ($803.4 \mu\text{W}$) and the widest synchronization range were found in the square case (the stationary in the rear). The results showed that the increase of the synchronization range in the square case was 380% compared to a single vibration cylinder. Nevertheless, for some spacing ratios, the effect of the interference cylinder on power harvesting was negligible by adding the circular or triangular cases in rear. However, the maximum value of average output power of a plate interference is higher than the value of square prism, and this difference between them reached up to 36%.

6.2. Multiple-cylinder configurations

Few researchers have studied FIO of three or four circular cylinders for hydrokinetic power harnessing. Due to the increase in the number of oscillators, the complexity of the flow field increases. Placing multiple cylinders in close proximity and making them work successfully would increase the power-to-volume ratio which is very low in all renewable technologies such as wind or water turbine farms. Therefore, it is

important to explore the energy conversion performance of a multi-cylinder CEC besides the two-cylinder case. The main references are reviewed next.

In [92], authors experimentally explored the influence of spacing ratio ($2.5 \leq L/D \leq 5.0$) on the FIO response of three or four rough tandem cylinders in the range $28,000 < Re < 120,000$. It should be noted that the oscillation occurred in the transverse direction corresponding to incoming flow for all cylinders. In general, for all oscillators, increasing Re is followed by an increase in amplitude. The only obvious difference is that the “bump phenomenon” appears in the initial VIV region for the second oscillator. Beyond that, the maximum amplitude decreases gradually from first cylinder to forth cylinder due to the power loss and velocity reduction of the incoming flow.

The FIO response and power harvesting performance of three and four rough rigid cylinders oscillating transversely to the incoming flow have been investigated in Refs. [11,139]. Kim et al. tested the CEC in the LTFSW channel and Ding et al. numerically using the 2D-URANS method. The numerical results were verified by experimental measurements. Detailed research results are described below.

In [11], authors selected two pivotal parameters to study: the spacing ratio ($L/D = 2.5, 3.0, 3.5, 4.0, 5.0$) and the incoming flow velocity U in the range ($0.51 \leq U \leq 1.45$ m/s). It should be pointed out that the synergy scale (ratio of total converted energy by N times the converted

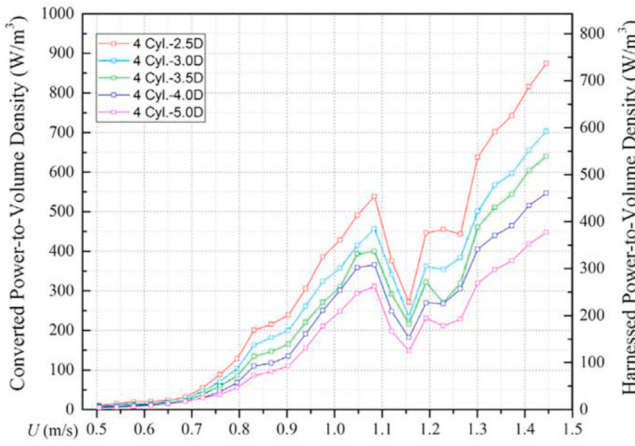


Fig. 70. Four cylinders: Power-to-volume density for five cases of L/D [11] ($L_{en} = 914$ mm; $D = 88.9$ mm; $K = 747.39$ N/m; $m^* = 1.689$).

energy of an isolated cylinder, where N represents the number of cylinders) indirectly reflects the performance of energy conversion. Results confirmed that the maximum synergy scale of the three cylinders and four cylinders was 1.95 and 1.91, respectively. In Fig. 70, the converted power increases as U increases except when $U = 1.08\text{--}1.16$ m/s. Results confirmed that, for the four-cylinder case, increasing the L/D varying from 2.5 to 5.0, drives the decrease in converted power-to-volume density. Results showed that the maximum conversion energy and power efficiency of the four cylinders case can reach up to 81J–88J and 88.6%, respectively.

In [139], authors selected a fixed value of the spacing ratio ($L/D = 2.5$) for three tandem oscillators (Fig. 71). The Reynolds number Re was selected in the range $30,000 < Re < 105,000$. The amplitudes of the three cylinders show an increasing trend as Re increases. Additionally, in galloping, the frequency variation is steady and has a similar value as the natural frequency of cylinders. Fig. 72 shows that increasing the Re number is followed by an increase in total power of the three cylinders except in galloping, which has higher value compared with the single or two-cylinder cases [11,26]. The results showed that the maximum power harnessing and power efficiency are, respectively, 85.26W at $U = 1.2$ m/s and 40.41% at $U = 0.54$ m/s. Although the power efficiency of three cylinders has an obvious advantage in comparison to the single or double-cylinder cases in the low flow velocity, the difference is reduced at high velocity.

In 2015, the 2-D URANS method was used to simulate the FIO response (i.e., oscillation amplitude; frequency; vortex pattern) of four rigid rough tandem cylinders in the range $30,000 < Re < 120,000$ [140]. A Spalart-Allmaras model was added to simulate the turbulence condition. The accuracy of the simulation results was validated by experimental measurements acquired in the LTFSW at the University of

Michigan. At $Re = 62,049$, for the cases of three or four tandem cylinders, the peak value of the amplitude of the first cylinder was $2.9D$, and the vortex pattern was 2P. However, at $Re = 90,254$, the vortex pattern of the first oscillator for three cylinders and four cylinders was 2P+4S and 2P+2S, respectively. Under the influence of upstream cylinders, the downstream cylinder has lower amplitude comparing with the case of upstream cylinders. Additionally, the oscillation frequencies for all cylinders were approximately equal. Ref. [141] also considered the amplitude and frequency of the three or four (rough) tandem cylindrical oscillators.

The above studies were mainly centered on multiple cylinders with tandem and side-by-side configuration. However, there are a few studies on multiple staggered cylinders oscillating in two directions. In addition, the staggered cylinders have more complex interference with each other. The parameters concerning the complexities for the stagger and tandem cylinders are listed in Table 5.

Therefore, it is necessary to study the FIO phenomenon and power harvesting for multiple staggered cylinders. Review of such studies follows.

In [142], authors adopted the numerical simulation to explore the VIV response for three smooth circular cylinders for reduced velocity U^* in the range $3 \leq U^* \leq 12$. The arrangement of those three cylinders was in an equilateral triangle, as shown in Fig. 73. The authors selected three different flow incidence angles ($\gamma = 0^\circ, 30^\circ$, or 60°) and a fixed value of spacing ($L = 4.0D$) between cylinders. The results showed that the different values of γ result in different synchronization range and maximum oscillation amplitude. Particularly, the maximum amplitude for downstream cylinder has higher value than an isolated oscillator because of the strong interference from two upstream cylinders. Recall that galloping may be induced not only geometric asymmetry but also flow asymmetry due to the presence of upstream wakes. In almost every case, the synchronization range of vibration is $4.0 \leq U^* \leq 8.0$, which is wider than that of the single-cylinder ($4.0 \leq U^* \leq 7.0$). It was stated that the three cylinders with an equilateral triangle arrangement have the potential to obtain more energy than that of an isolated oscillator.

Compared with above study [142], similar conclusions have been derived in Refs. [143,144]. Han et al. selected $\gamma = 0^\circ, 60^\circ, 90^\circ$ and $L/D = 1.5$ for $3.0 < U^* < 16.0$. As expected, the effect of flow incident angle on the synchronization range was clear [143]. At $\gamma = 0^\circ$, the synchronization range is $4.0 < U^* < 10.0$; at $\gamma = 60^\circ$, the synchronization range is $3.0 < U^* < 16.0$; at $\gamma = 90^\circ$, the synchronization range is $4.0 < U^* < 11.0$. Han et al. selected $\gamma = 0^\circ, 60^\circ, 75^\circ, 90^\circ, 105^\circ$ and $L/D = 4.0$ for $1.0 < U^* < 30.0$ [144]. The VIV phenomenon of three cylinders (in an equilateral triangular array) has been explored for some spacing ratios varying from 1.5 to 6.0 [145]. Results confirmed that these multiple cylinder systems can develop higher oscillation amplitude than that of a single cylinder. Other similar study of FIV amplitude and force analysis of three cylinders in triangular arrangement was conducted in Ref. [146].

A numerical simulation was utilized to investigate the influence of

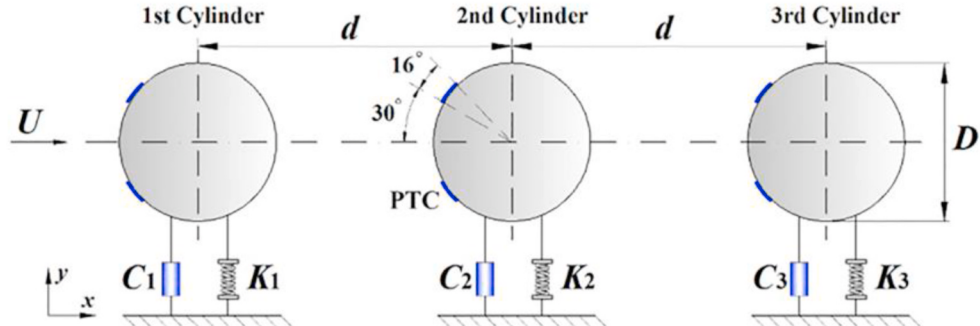


Fig. 71. Physical model of three roughness tandem cylinders [139] (1st cylinder: $D = 88.9$ mm, $K = 834$ N/m, $\zeta_{harness} = 0.0206$, $m^* = 1.681$; 2nd cylinder: $D = 88.9$ mm, $K = 828$ N/m, $\zeta_{harness} = 0.0198$, $m^* = 1.690$; 3rd cylinder: $D = 88.9$ mm, $K = 806$ N/m, $\zeta_{harness} = 0.0172$, $m^* = 1.667$).

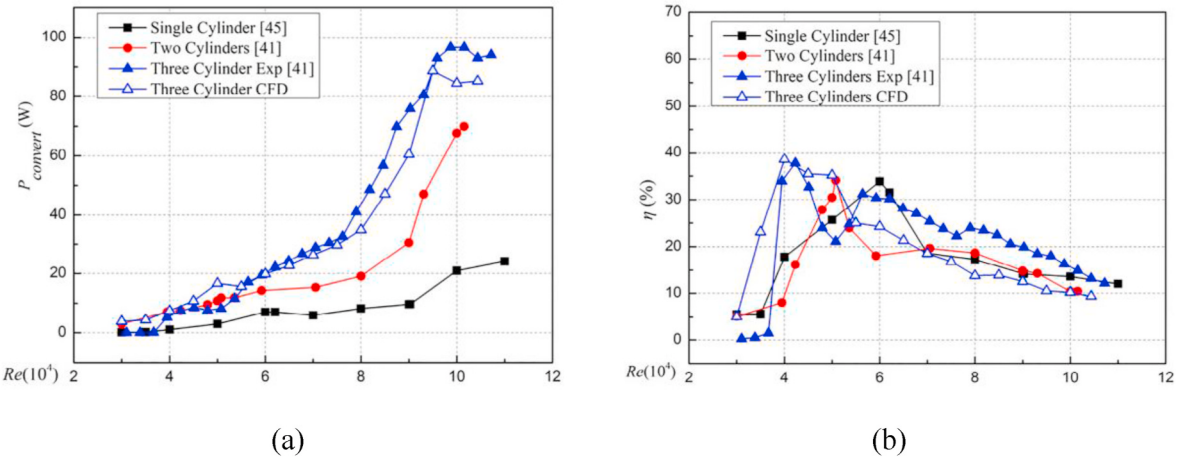


Fig. 72. Power harnessing and efficiency: (a) power harnessing; (b) power efficiency (parameters refer to Fig. 71.) [139].

Table 5

Parameters in tandem/staggered cylinders and the effect on the FIO.

The main parameters/variables	Effects in FIO
Stiffness (K) and mass ratio (m^*)	The oscillation frequency, the VIV synchronization zone, the onset and desynchronization of VIV.
Damping/ratios (ζ)	The VIV synchronization zone, the onset of galloping
Spacing ratio (L/D)	Shielding effect on the downstream cylinder, the onset of VIV and galloping, the oscillation patterns.
Staggered (S/D , transverse spacing or incidence angles)	Shielding effect on the downstream cylinder (less pronounced), the onset of VIV and galloping, the oscillation patterns.

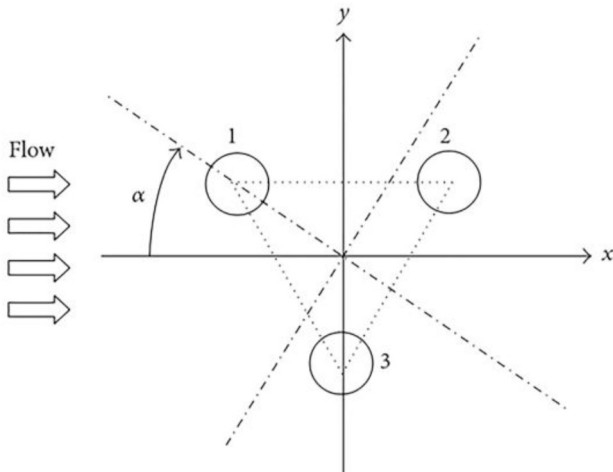


Fig. 73. Schematic of three cylinders in the equilateral triangle arrangement [142] (Spacing $L = 4D$; $m^* = 2.0$; $\zeta_{structure} = 0$).

flow incident angle γ of four cylinders in a square arrangement in VIV at $1000 < Re < 20,000$ [147], as shown in Fig. 74. The authors selected the incident angle $\gamma = 0^\circ, 15^\circ, 30^\circ, 45^\circ$ and cylinder spacing $L/D = 4.0$ for $1.0 < U^* < 20.0$. The synchronization zones of cases $\gamma = 0^\circ, 15^\circ, 30^\circ, 45^\circ$ are $3.0 < U^* < 9.0$, $3.0 < U^* < 12.0$, $3.0 < U^* < 9.0$, $2.0 < U^* < 4.0$, respectively. It was demonstrated that the oscillator vibration in the synchronization zone is regular and stable, indicating that the wider the synchronization region is, the higher the possibility of converting hydrokinetic energy to electric energy. Therefore, in all cases of flow incident angles, the case $\gamma = 15^\circ$ may become the optimal one. In

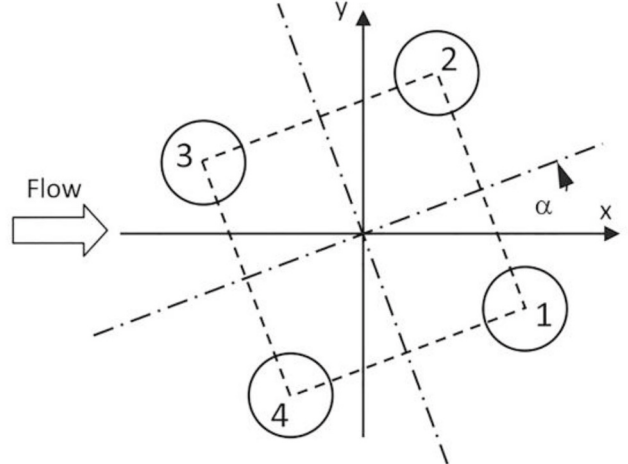


Fig. 74. Schematic of four cylinders in a square arrangement [147].

Ref. [148], authors also focused their attention on proving the strong influence of flow incident angle and incoming flow speed on VIV vibration amplitude and frequency.

The VIV response for four circular cylinders has also been analyzed by the numerical simulation [149]. They varied the spacing ratio in $1.5 \leq L/D \leq 4.0$. As shown in Fig. 75, the arrangements of the four cylinders were categorized in two forms: the four rigidly connected or the four separately mounted. The results showed that, for the four rigidly connected cylinders, $L/D = 1.5$ is the optimal case to realize the maximum vibration amplitude. In addition, a wider synchronization range ($3.0 < U^* < 25.0$) occurred in the case of $L/D = 2.0$. Further, selecting L/D higher than 2.5, owing to the weak interaction between four cylinders, the oscillation amplitude of these cylinders has a similar value as the single-cylinder. The FIV response for the four-cylindrical oscillators in an in-line square array was analyzed in Ref. [150] when $Re = 80$ and 160.

The above studies on staggered arrangement mainly focused on the FIV response. However, related studies on energy harnessing are infrequent. Those are reviewed next.

In [151], authors numerically investigated the VIV power conversion by four-cylinder arrays by changing the spacing between them, as shown in Fig. 76. Spacing in both directions was changed: in-flow spacing ($X = 1.0\text{--}10.0D$); transverse spacing ($Y = 1.0\text{--}8.0D$). In addition, the amplitude response can be divided into three regions: Synchronization region: $X < 2.0D$; Blocking or Enhancing region: $2.0D < X < 4.0D$; Recovery

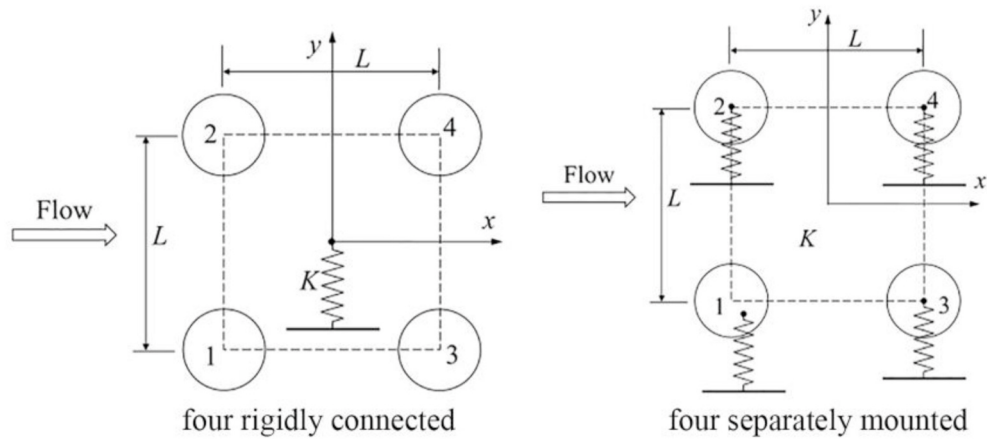


Fig. 75. Schematic diagram of four cylinders in square arrangement in Ref. [149].

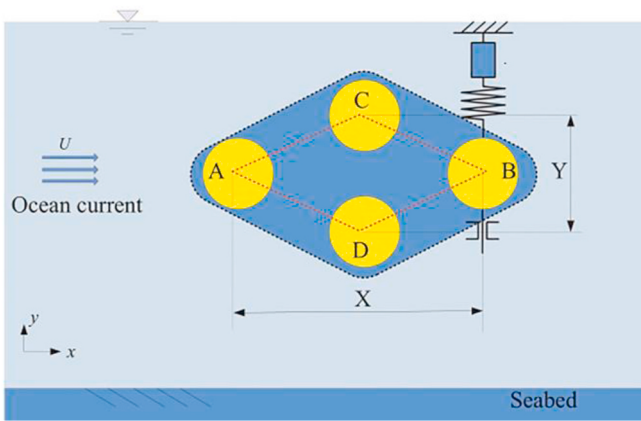


Fig. 76. The model of four staggered cylinders [151] ($D = 90$ mm; $m^* = 1.68$; $K = 814$ N/m; $\zeta_{total} = 0.02$).

region: $X > 4.0D$. For $X < 2.0D$, the amplitudes for four cylinders are about equal. In the Blocking or Encouraged region, the downstream cylinder B has an obvious amplitude enhancement compared to an isolated single cylinder and has a maximum amplitude of $1.78D$. For power harnessing, the maximum values of cylinder A and cylinder B are

$4.15W$ ($X = 1.7D$, $Y = 7.0D$) and $11.95W$ ($X = 2.0D$, $Y = 4.0D$), respectively. The results show that, with decreasing X and increasing Y , corresponding average value of power-to-volume density increases (Fig. 77). Moreover, the maximum density can reach up to $133W/m^3$ for $X = 1.2D$ and $Y = 7.0D$.

A brief summary of the studies on hydrokinetic energy extraction for multi-cylinders is presented in Table 6. It should be pointed out that the maximum power in Table 6 represents the power per unit length of cylinder. Additionally, under the same conditions, the multi-cylinder CEC with interaction have N times the harnessed power of the same number of cylinders without interacting. From Table 6, it can be observed that under the tested conditions, the interaction between multi-cylinders can have a positive effect on power harvesting.

From the papers reviewed above, it can be confirmed that multiple cylinders in tandem, staggered, or in arrays, which include three or four cylinders, can produce a better performance than that of the single-cylinder in the aspects of the energy harvesting and FIV response. However, there are only a few studies on power harnessing on multi-cylinder energy converters. Therefore, this is an area that requires further investigation research experimental and numerical.

7. Converters with mechanically linked oscillators

In recent years, a multi-mass system composed of mechanically connected oscillators has been investigated. The purpose of this research is to explore whether a multi-mass system can harvest more hydrokinetic energy and achieve higher corresponding efficiency than that of a single-mass system. In modeling, taking a dual-mass system as an example, as shown in Fig. 78-a, the coupled equations of the two oscillators can be expressed as follows:

$$m_1\ddot{y}_1 + c_1\dot{y}_1 + K_1y_1 + K_2(y_1 - y_2) = F_{Fluid} \quad (20)$$

$$m_2\ddot{y}_2 + c_E\dot{y}_2 + K_2(y_2 - y_1) = 0 \quad (21)$$

where y_1 and y_2 are the positions of the two oscillating bodies in galloping and the second mass body, respectively. Further, m_1 and m_2 represent the mass of the first oscillating galloping body and the second body, respectively; K_1 and K_2 are the linear spring stiffness values; c_1 and c_E are the viscous damping values. The relevant researches have been investigated in Refs. [152–155]. The performance of the dual mass system can be explored by changing the values of the mass ratio m_2/m_1 , power takeoff coefficient, and spring stiffness. The principle of power harvesting can be explained as follows: The galloping oscillator moves perpendicular to the flow velocity, then, directly drives the secondary mass. Electricity is produced induced by the relative movement between the permanent magnet (driven by secondary mass) and the coil. Even though the dual-mass system enhances the structural complexity

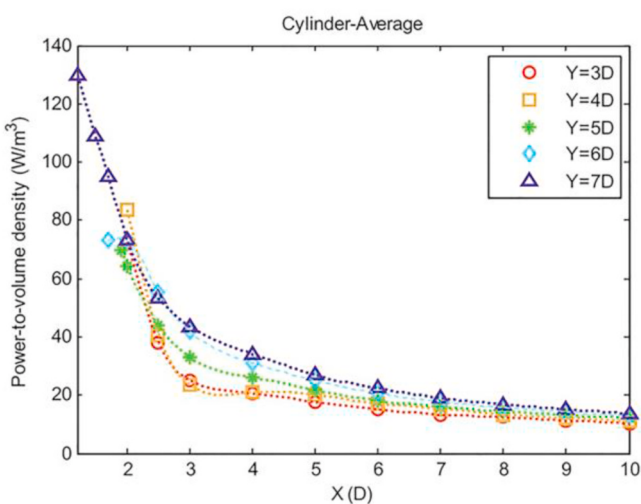


Fig. 77. Average power-to-volume density [151] ($D = 90$ mm; $m^* = 1.68$; $K = 814$ N/m; $\zeta_{total} = 0.02$).

Table 6

Comparison of power harvesting by multiple-cylinder CEC.

Ref.	Method	Number of cylinders	Re	$D(\text{mm})$	$P_{\max}(\text{W/m})$	$N(\text{times})$	$\eta_{\max}(\%)$
[11]	Exp. (Water)	Two Tandem	38,000–114,000	88.9	100.66	1.50	38
[11]	Exp. (Water)	Three Tandem	38,000–114,000	88.9	138.95	1.96	57
[11]	Exp. (Water)	Four Tandem	38,000–114,000	88.9	179.43	1.92	74
[34]	Exp. (Water)	Two Tandem	30,000–120,000	88.9	46.93	6.75	63
[136]	Exp. (Water)	Two Stagger	25,000–120,000	88.9	31.28	1.60	—
[139]	2D CFD (Water)	Three Tandem	30,000–105,000	88.9	85.26	2.17	40.41

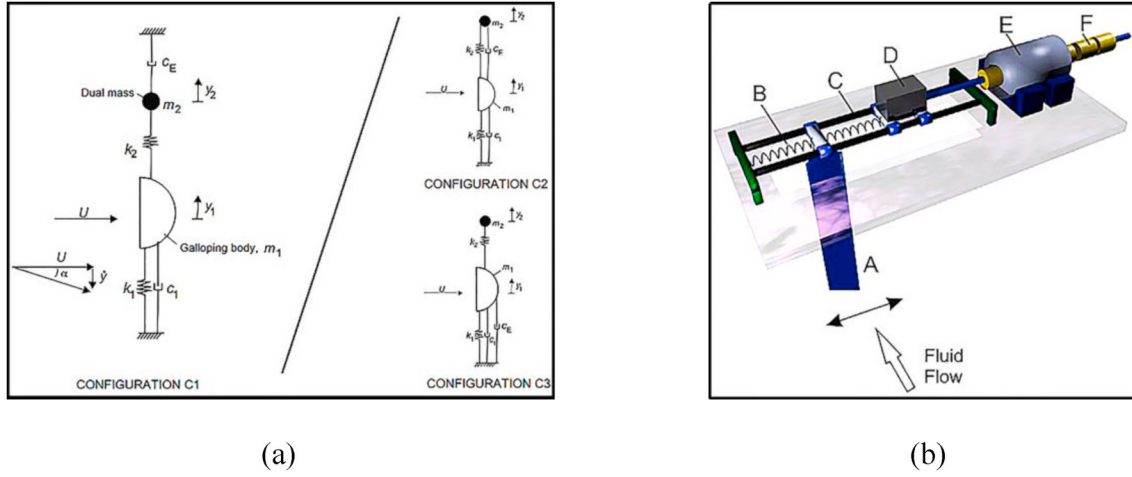


Fig. 78. Diagram of the dual mass system in Ref. [152]: (a) Three possible dual-mass configurations. (b) The simulated three-dimensional model of the first configuration C1 ($L_{en} = 1000 \text{ mm}$; $D = 50 \text{ mm}$; $m^* = 10$).

comparing to the single mass system, it was verified that the former can realize the goal of the research by adjusting the oscillators' parameters, i.e., mass ratio and damping coefficient.

Based on the research in Ref. [156], in Ref. [152], authors applied the dual-mass device to investigate the power harvesting from transverse galloping by utilizing the standard Harmonic Balance Method (HBM). The dual-mass system was designed at three different configurations, as shown in Fig. 78-a. Fig. 78-b is the simulated three-dimensional model of the first configuration C1. The results

indicated that, compared with a single-mass system, the dual mass configuration can harness energy in a broader incoming flow velocity range, thus, it can harvest more energy and achieve higher efficiency. As shown in Fig. 79, taking the first configuration C1 as an example, the increase of the maximum efficiency for this dual mass system can reach up to 12% over the single-mass system. Moreover, the range of reduced velocity improved from $5.0 < U^* < 9.0$ to $8.0 < U^* < 21.0$ and the power efficiency is exceed 0.4. It should be pointed out that the configurations C1 and C2 can improve the efficiency by adding the parasitic damping

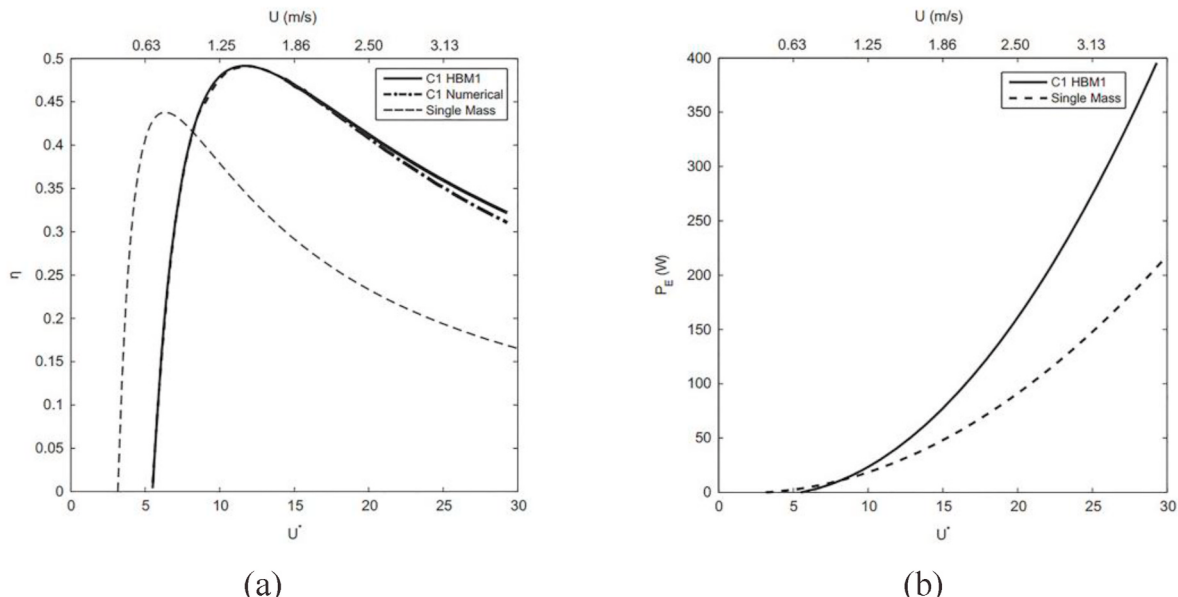


Fig. 79. Power harvesting and efficiency vs. reduced velocity for the first configuration C1 in Fig. 78: (a) Efficiency variation; (b) Power harvesting [152] ($L_{en} = 1000 \text{ mm}$; $D = 50 \text{ mm}$; $m^* = 10$).

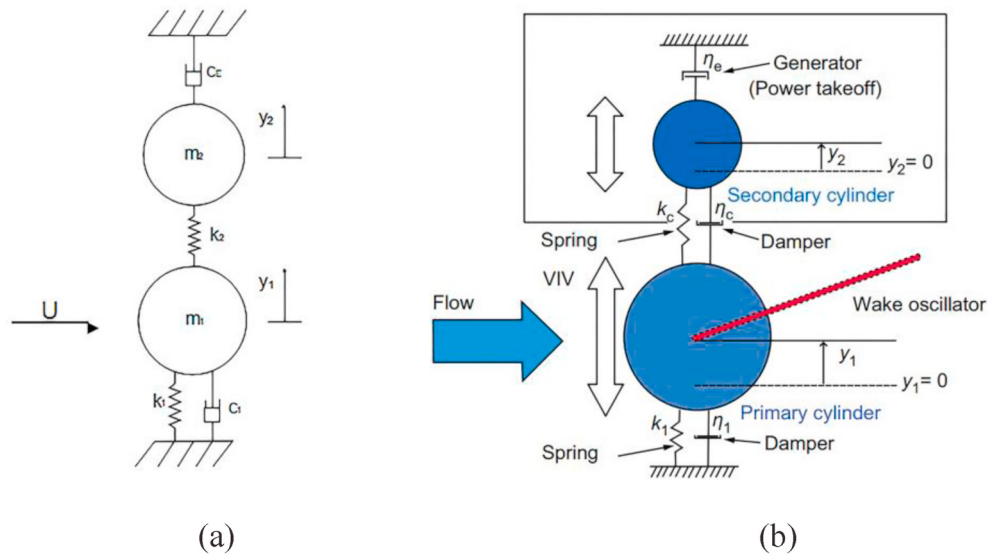


Fig. 80. Schematic of the FIO model of a dual-mass system: (a) Without a wake oscillator. (b) With a wake oscillator [153,154].

under the adaptive values of the mass ratio and frequency ratio.

In order to attain maximum efficiency and increase the flow velocities range of efficient energy harvesting, VIV as another vibration pattern of a dual-mass system was theoretically investigated [153], as shown in Fig. 80-a. The authors found that the dual-mass system, comparing with the corresponding single-mass system, can reach higher maximum efficiency under appropriate relation of mass and spring stiffness between the two system components when the damping coefficient $\zeta_1 \neq 0$. Of course, when $\zeta_1 = 0$, the dual-mass system cannot improve the maximum power efficiency since there is no mechanism for power conversion. It was found that efficient energy harvesting can materialize within a wider range of incoming flow velocity. Therefore, the dual-mass system provides the practical advantage of harnessing energy in an environment of variable velocity of the fluid flow.

Additionally, in Ref. [154], authors pursued similar theoretical research on the dual-mass device in order to improve the VIV energy efficiency. The author added a virtual wake oscillator (with a nonlinear equation of motion) to simulate the phenomenon of Fluid-Structure Interaction to eliminate the computational expenditure, as shown in Fig. 80-b. The nonlinear equations were processed by an averaging method. They reached similar conclusions by showing that the dual-mass system has superior performance and can reach higher power extraction than that of a single-mass system.

The same conclusion was reached in an experiment conducted in Ref. [155]. A two-degree of freedom system was added to the FIO system for comparing its energy harvesting to that of a single degree of freedom system. Particularly, selecting the reduced velocity in the range of 12.0–14.0 when the mass ratio was 1.5 and 2.0, the vibration amplitudes of cylinder A and cylinder B were both larger than that of the corresponding single-mass system. The results indicated that the dual mass system can realize more energy harvesting over a broader range of reduced velocities.

As mentioned above, the dual mass system can obtain more power and achieve higher efficiency than that of the single-cylinder. Nevertheless, this novel direction has not been widely studied in recent years. Therefore, it can be explored further to find a relation between energy harnessing and second mass parameters.

8. Velocity-based, nonlinear, adaptive harnessing damping

In all the papers reviewed up to now, the damping model was the linear viscous damping as in Eq. (9). Damping is the most important parameter as it is vital for energy acquisition from the oscillator in FIO.

The damping ratio ranged from 0.02 to 0.26 [135] but remained constant during a specific test. Thus, the viscous damping force, induced by incoming flow, remains proportional to that oscillating velocity for cylinder. At lower damping ζ_{harness} , the oscillation amplitude ratio A/D and the oscillation velocity are high, pushing the oscillating body to the limit of the experimental energy converter. However, due to low ζ_{harness} , the harvested energy is low [55]. As the damping ratio ζ_{harness} increases, the initial converted energy increases. At high damping ζ_{harness} , though, the low oscillation speed and small amplitude cannot induce an effective FIO, resulting in low energy acquisition that may not even be maintained all the time. Thus, nonlinear adaptive damping based on the oscillation velocity was proposed [23,127] in order to obtain the optimal harnessed energy by selecting the appropriate damping. At low speed, lower damping is required to initiate and maintain VIV and possibly galloping. At high speed of the oscillating body, higher damping will prevent the oscillator from reaching damaging amplitudes while extracting energy from the oscillator. Therefore, they proposed a non-linear model for damping adapting to the oscillator speed as modeled by Eq. (22). For a given fixed damping factor (c_h), the adaptive harnessing damping coefficient is proportional to the oscillator velocity.

$$c_{\text{adapt}}(\dot{y}) = c_h \dot{y} \quad (22)$$

where y represents the vibration displacement. Both in VIV and galloping and to first order, the oscillation can be modeled by a single frequency sinusoidal function, as in Eq. (23)

$$y = A \sin(\omega_{\text{osc}} t) \quad (23)$$

where ω_{osc} is the angular oscillation frequency. Fig. 81 shows the relationship between the nonlinear adaptive harnessing damping and oscillation speed of the cylinder. The c_h values selected in the experiments [23,127] were 12.5, 25.0, 37.5 and 50.0 N/m. For comparison with the linear case, the linear damping value has been chosen as 30.0 N/m [127].

The harnessing damping force can be modeled versus the vibration velocity as:

$$F_{\text{damping}} = c_{\text{adapt}}(\dot{y}) \dot{y} = c_h \dot{y}^2 \quad (24)$$

Thus, the harnessing damping force is quadratic in relation to the velocity. That is, the nonlinear damping is formed adaptive to the oscillator velocity. For the power harnessed using nonlinear adaptive damping, the average value of instantaneous power should be used. The harnessed power equation for nonlinear adaptive damping is:

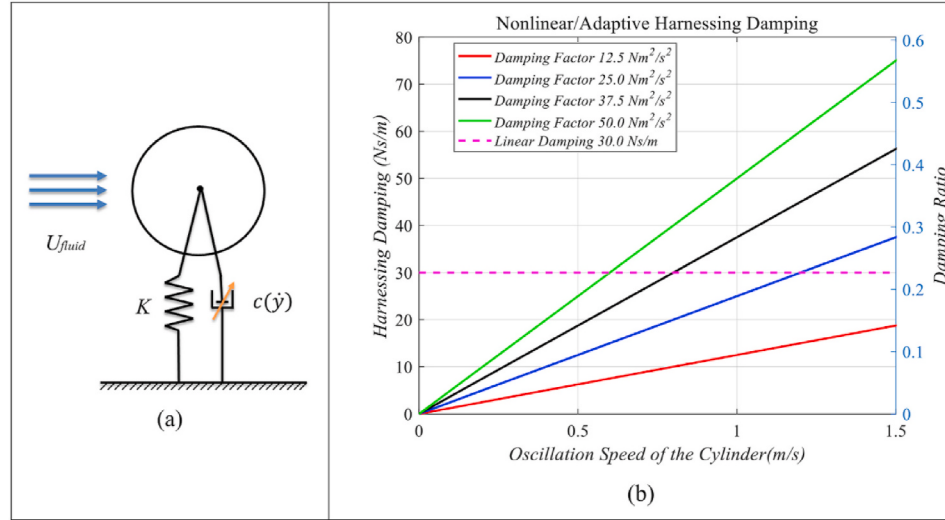


Fig. 81. Schematic of adaptive harnessing damping: (a) The model of Oscillator; (b) Nonlinear/Adaptive Harnessing Damping [23].

$$P_{harness} = \frac{1}{T_{osc}} \int_0^{T_{osc}} (m_{osc}\ddot{y} + c_{adapt}(\dot{y})\dot{y} + Ky)\dot{y}dt \quad (25)$$

where T_{osc} is the period of oscillation. The spring and mass terms are conservative integrating to zero over a cycle. Energy is converted only through the non-conservative term yielding Eq. (26):

$$P_{harness} = \frac{1}{T_{osc}} \int_0^{T_{osc}} c_{adapt}(\dot{y})\dot{y}\dot{y}dt = c_h\dot{y}^3 \quad (26)$$

Thus, the harnessed power is cubic in relation to the velocity.

In their experiments in the MRELab, the team of Bernitsas, implemented the nonlinear adaptive damping using the Vck controller [127]. The model was enabled by using location and velocity information in the encoder of the servo-motor (Fig. 53). That is, a dedicated, specially designed, controller like the Vck that does not bias the FIO is needed to enable adaptive damping experimentally.

The experiments showed that:

- (a) For the adaptive damping case, its velocity range for each flow regime (VIV branches, VIV-galloping transition, and galloping) is not dependent on the value of c_h .
- (b) This is contrary to the linear damping case, where increasing the linear viscous damping lead to narrow corresponding range of all the FIO regimes.
- (c) The higher the value of c_h , the higher of the resulting amplitude ratio.
- (d) One of the most significant phenomena is that this nonlinear adaptive damping can eliminate the gap (regarded as the region which has no power generate) between VIV and galloping, indicating that power harvesting can be realized in all experimental flow velocities. This was also achieved by the nonlinear spring stiffness based on the oscillation position as analyzed in Section 5.
- (e) Regarding the frequency of the oscillatory response, in VIV-galloping transition region, this nonlinear oscillator exhibits a more stable frequency compared with the linear damping oscillator.
- (f) Regarding the harnessed power and efficiency of this ALT current energy converter, compared with the linear damping case, the nonlinear adaptive damping achieves a lower onset velocity for FIO (in the initial VIV branch) without narrowing down the synchronization range of FIO.
- (g) In the transition region, due to the overlap of the VIV and galloping, its harnessed power with nonlinear adaptive is 128% higher than that of the linear damping oscillator.

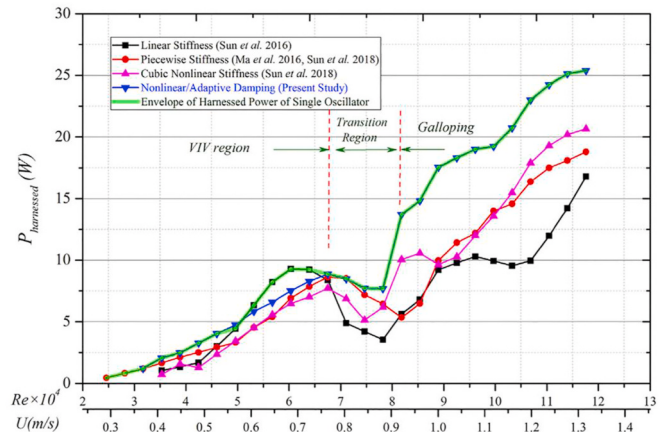


Fig. 82. Power envelop of a single-cylinder converter based on experiments for five oscillator models [127] (Linear Stiffness: $D = 88.9$ mm, $L_{en} = 895$ mm, $K = 400-1,200$ N/m, $\zeta_{harness} = 0-0.24$; Piecewise Stiffness: $D = 88.9$ mm, $L_{en} = 895$ mm, $\zeta_{harness} = 0.13, 0.26, 0.39, 0.53$; Cubic Nonlinear Stiffness: $D = 88.9$ mm, $L_{en} = 915$ mm, $\zeta_{harness} = 0.13, 0.26, 0.39, 0.53$; Nonlinear Damping: $D = 88.9$ mm; $L_{en} = 915$ mm; $K = 400, 600, 800$ N/m).

- (h) Additionally, for galloping, the corresponding power increase reaches around 51%–95% compared to the linear viscous damping.
- (i) As shown in Fig. 82, especially in transition region and galloping, as expected, this energy converter using nonlinear adaptive damping can convert higher energy than that of the other four oscillators including the nonlinear spring stiffness. In other words, the nonlinear adaptive damping converter has become the optimal energy converter if we select the appropriate value of damping factor (c_h).

In 2020, the impact of adaptive harnessing damping was further investigated by replacing the single cylinder with two tandem-cylinders in flow-induced oscillation in the range $24,000 < Re < 120,000$ [23]. The relationship between harnessing damping and velocity of these two tandem-cylinders was selected to be the same as in Ref. [127] for single cylinder (Fig. 81). The two spacing ratios tested were $L/D = 2.01$ and 2.57 ; the three linear spring stiffness values tested were $K = 400, 600, 800$ N/m. One of the purposes of adding adaptive harnessing damping to the two tandem-cylinder system was to reduce the shielding effect. The

shielding effect is a phenomenon with negative impact on the oscillating amplitude for the downstream cylinder, which result in a decrease in power harvesting.

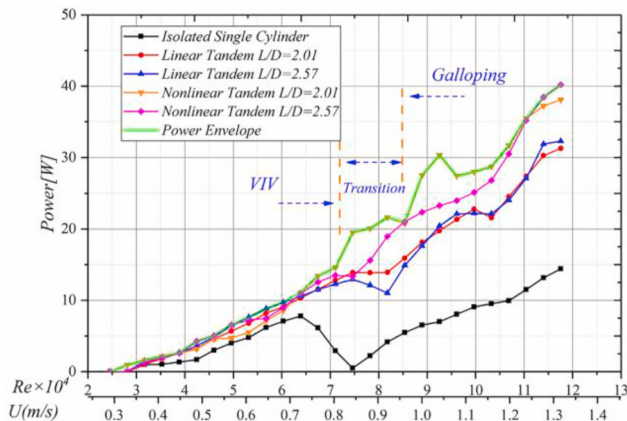
Due to the low damping adapted in low velocity where flow energy is low, the onset velocity of FIOs was lowered to 0.31 m/s. Besides that, in the VIV region, as the nonlinear (c_h) damping coefficient increases, the corresponding power and efficiency both increase. As shown in Fig. 83, compared with the linear tandem cylinders, the corresponding increment of power and efficiency for the nonlinear tandem cylinders is listed in Table 7 [23]. Therefore, implementing adaptive damping enhances the harvested power or its efficiency for two tandem-oscillators, especially in the high-velocity (transition and galloping regions). Most important it eliminates the gap between VIV and galloping.

Combining the results in the two papers [23,127] above, it is concluded that the nonlinear adaptive damping converter with appropriate nonlinear parameters has the highest potential than all the other current energy converters with linear or nonlinear model studied. The adaptive damping technology can balance the variation between the damping and oscillation velocity of the oscillator, resulting in the higher energy harvesting. Research using adaptive damping in nonlinear control can further improve CEC based on FIO.

9. Summary and major conclusions

To maximize the efficiency of ALT Converters over a broad range of the flow velocity, requires understanding of the effects of parameters and nonlinearities of oscillators. Output such as the onset and termination of the VIV synchronization range, VIV-galloping transition region, and onset of galloping are important since they define the range of flow velocity over which a CEC can harness energy in a variable flow-speed environment. By changing the mass or stiffness of the oscillator to passively adjust the natural frequency of the oscillator, the utilization of MHK energy can be effectively improved. Equally important, but more difficult to assess, is the impact of nonlinearities on the design of oscillators to improve the oscillator response. This paper has provided a comprehensive review of response of nonlinear oscillators to harness hydrokinetic energy classifying nonlinearities in six categories. Comparisons made in Tables 1–6 should be most useful in assessing oscillators and comparing nonlinearities and parametric effects. The major conclusions per category follow:

- (1) Geometric changes in oscillator cross-section: Since the FIV typically is triggered by the vortex shedding from the oscillator, using different shapes can be an efficient way to alter the response without changing the oscillating system and structures.



(a)

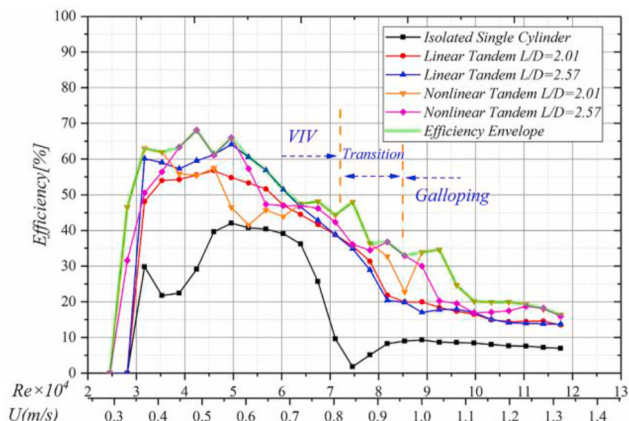
Table 7

[23]. Increase of power and efficiency for a two-cylinder converter with nonlinear adaptive damping compared with the linear one.

Increase (%)	Power	Efficiency
In the transition region	46%	34%
Initial galloping stage	33%	94%
Fully developed galloping region	35%	33%

Non-circular cross section can trigger galloping that taps into higher potential harnessing energy in high flow velocity. e.g., circular, square or rectangular, trilateral shapes. The effect of different shapes is to extend the FIV to galloping, which results in higher harnessed power and possibly efficiency. Different cross-sections at different angle of attack of the cylinder converters are summarized.

- (2) Passive control of FIV: The turbulence control of FIV/O and vortex shedding are summarized. Changing the surface roughness by the means of PTC, placing different shaped rods or fin-shape strips results in a wider range of synchronization regions and increase of the maximum amplitude. The benefit is similar to different cross-sections of the oscillators, since it expands the FIO range of the converter by enabling back-to-back VIV with galloping leaving no gap between them in the flow velocity range tested.
- (3) Position based nonlinear stiffness converter: They allow reduction or increase of the spring restoring force to better match the ability of the fluid to push the cylinder. That is, where the fluid force is small (away from the vortex shedding moment) the spring force may be set to be small. At the moment of shedding the spring resistance may be set to be higher. That results in more efficient way of harnessing hydrokinetic power.
- (4) Multi-cylinder synergistic FIV: The interaction between the cylinders (tandem and staggered), the gap flow, and the vortex patterns between the oscillators, show a positive effect for synergy of the oscillators in the converter. In recent research, as expected, under the same controllable parameters, the harvested or converted power for two tandem cylinders can reach to higher than double compared to corresponding single one. In some experimental and computational testing, the power of two cylinders can reach up to 2.56–7.5 times that of the single one.
- (5) Mechanically linked oscillators: Mechanically linked oscillators in the converter may have similar benefit in enhancing the motion of the oscillators. Despite the limits of the interaction



(b)

Fig. 83. Optimal power and efficiency of nonlinear and linear damping: (a) power; (b) efficiency [23]. ($L_{en} = 895$ mm; $D = 88.9$ mm; $m^* = 1.343$; $L/D = 2.01$ and 2.57 ; $K = 400, 600, 800$ N/m; $c_{structure} = 3.41$.)

between the vortex shedding, gap flow and the mechanically link might result negative effect on the FIV.

(6) **Velocity based adaptive damping:** Velocity based adaptive damping is the optimal solution, so far. It mimics the natural response of fish in exchanging energy between the moving fluid and the oscillator. The introduction of adaptive damping makes it possible to maintain the FIO range (VIV branches, transition to galloping, and galloping) while harnessing energy. In addition, adaptive damping lowers the initial velocity of power harvesting and improves the performance of fluid kinetic energy conversion. At the end of testing range for galloping, as flow velocity increases, corresponding damping or power harnessed are balanced, resulting in a stable process for the power and efficiency.

Credit author statement

Yanfang Lv: Writing – original draft, Writing – review & editing, Investigation, Data curation, Formal analysis, Methodology, Validation, Visualization; Liping Sun: Formal analysis, Resources, Funding acquisition, Validation; Michael M. Bernitsas: Formal analysis, Writing – review & editing, Validation; Hai Sun: Conceptualization, Resources, Data curation, Writing – review & editing, Methodology, Project administration, Validation.

Declaration of competing interest

The authors declare that they have no known competing financial interests or personal relationships that could have appeared to influence the work reported in this paper.

Acknowledgements

This research was funded by the National Key Research and Development of China (No. YS2017YFGH000163), National Nature Science Foundation of China (No.51609053), the Natural Science Foundation of Heilongjiang Province (No. YQ2019E017) and the Cooperative Agreement No. DE-EE0006780 between Vortex Hydro Energy, Inc. and the U. S. Department of Energy. The MRELab of the University of Michigan is a subcontractor through Vortex Hydro Energy.

References

- [1] Strouhal V. Über eine besondere Art der Tonerregung. *Ann Phys* 1878;241(10): 216–51.
- [2] Bearman PW. Circular cylinder wakes and vortex-induced vibrations. *J Fluid Struct* 2011;27(5):648–58.
- [3] Sarpkaya T. A critical review of the intrinsic nature of vortex-induced vibrations. *J Fluid Struct* 2004;19(4):389–447.
- [4] Williamson CHK, Govardhan R. Vortex-induced vibrations. *Annu Rev Fluid Mech* 2004;36:413–55.
- [5] Bernitsas MM, Raghavan K, Ben-Simon Y, Garcia EMH. VIVACE (Vortex Induced Vibration Aquatic Clean Energy): a new concept in generation of clean and renewable energy from fluid flow. In: Proceedings of the 25th international conference on offshore mechanics and arctic engineering; 2006 june 4–9; hamburg, Germany. ASME; 2002. p. 619–37.
- [6] Bernitsas MM. Harvesting energy by flow included motions. In: Dhanak MR, Xiros NI, editors. Springer handbook of ocean engineering. Heidelberg: Springer-Verlag; 2016. p. 1163–244.
- [7] Chang CCJ, Kumar RA, Bernitsas MM. VIV and galloping of single circular cylinder with surface roughness at $3.0 \times 10^4 \leq Re \leq 1.2 \times 10^5$. *Ocean Eng* 2011; 38:1713–32.
- [8] Park HR, Bernitsas MM, Chang CC. Map of passive turbulence control to flow-induced motions for a circular cylinder at $30,000 < Re < 120,000$: sensitivity to zone covering. In: Proceedings of the 32nd international conference on ocean, offshore and arctic engineering; 2013 jun 9–14; nantes, France. ASME; 2013. p. 1–10.
- [9] Park H, Kumar RA, Bernitsas MM. Enhancement of flow-induced motions of rigid circular cylinder on springs by localized surface roughness at $3 \times 10^4 \leq Re \leq 1.2 \times 10^5$. *Ocean Eng* 2013;72:403–15.
- [10] Barrero-Gil A, Pindado S, Avila S. Extracting energy from vortex-induced vibrations: a parametric study. *Appl Math Model* 2012;36(7):3153–60.
- [11] Kim ES, Bernitsas MM. Performance prediction of horizontal hydrokinetic energy converter using multiple-cylinder synergy in flow induced motion. *Appl Energy* 2016;170:92–100.
- [12] Ma CH, Sun H, Nowakowski G, Mauer E, Bernitsas MM. Nonlinear piecewise restoring force in hydrodynamic power conversion using flow induced motions of single cylinder. *Ocean Eng* 2016;128:1–12.
- [13] Liao JC, Beal DN, Lauder GV, Triantafyllou MS. Fish exploiting vortices decrease muscle activity. *Science* 2003;302:1566–9.
- [14] Cottone F, Vocca H, Gammaitoni L. Nonlinear energy harvesting. *Phys Rev Lett* 2009;102:086061.
- [15] Mackowski AW, Williamson CHK. Developing a cyber-physical fluid dynamics facility for fluid-structure interaction studies. *J Fluid Struct* 2011;27:748–57.
- [16] Huynh BH, Tjahjowidodo T, Zhong ZW, Wang Y, Srikanth N. Nonlinearly enhanced vortex induced vibrations for energy harvesting. In: Proceedings of the 2015 IEEE international conference on advanced intelligent mechatronics; busan, korea (South). IEEE; 2015. p. 91–6.
- [17] Huynh BH, Tjahjowidodo T, Zhong ZW, Wang YY, Srikanth N. Numerical and experimental investigation of nonlinear vortex induced vibration energy converters. *J Mech Sci Technol* 2017;31(8):3715–26.
- [18] Lee JH, Xiros N, Bernitsas MM. Virtual damper-spring system for VIV experiments and hydrokinetic energy conversion. *Ocean Eng* 2011;38(5):732–47.
- [19] Lee JH, Bernitsas MM. High-damping, high-Reynolds VIV tests for energy harvesting using the VIVACE converter. *Ocean Eng* 2011;38(16):1697–712.
- [20] Abdelkefi A, Hajj MR, Nayfeh AH. Phenomena and modeling of piezoelectric energy harvesting from freely oscillating cylinders. *Nonlinear Dynam* 2012;70: 1377–88.
- [21] Sun H, Ma CH, Bernitsas MM. Hydrokinetic power conversion using flow induced vibrations with nonlinear (adaptive piecewise-linear) springs. *Energy* 2018;143: 1085–106.
- [22] Sun H, Ma CH, Bernitsas MM. Hydrokinetic power conversion using flow induced vibrations with cubic restoring force. *Energy* 2018;153:490–508.
- [23] Sun H, Bernitsas MM, Turkol M. Adaptive harnessing damping in hydrokinetic energy conversion by two rough tandem-cylinders using flow-induced vibrations. *Renew Energy* 2020;149:828–60.
- [24] Barton DAW, Burrow SG, Clare LR. Energy harvesting from vibrations with a nonlinear oscillator. *J Vib Acoust* 2010;132(2):021009.
- [25] Kumar RA, Sohn CH, Gowda BH. Passive control of vortex-induced vibrations: an overview. *Recent Pat Mech Eng* 2008;1(1):1–11.
- [26] Zdravkovich MM. Flow around circular cylinders volume 1: fundamentals. Oxford: Oxford University Press; 1997.
- [27] Paidoussis MP, Price SJ, Langre de E. Fluid-structure interactions. New York: Cambridge University Press; 2011.
- [28] Sun H, Kim ES, Bernitsas MM. Virtual spring-damping system for flow-induced motion experiments. *J Offshore Mech Arctic Eng* 2015;137(6):061801.
- [29] Bernitsas MM, Ofuegbie J, Chen JU, Sun H. Eigen-solution for flow induced oscillations (VIV and galloping) revealed at the fluid-structure interface. In: Proceedings of the 38th international conference on ocean, offshore and arctic engineering; 2019 jun 9–14; glasgow, Scotland. ASME; 2019. p. 1–21.
- [30] Sun H, Kim ES, Nowakowski G, Mauer E, Bernitsas MM. Effect of mass-ratio, damping, and stiffness on optimal hydrokinetic energy conversion of a single, rough cylinder in flow induced motions. *Renew Energy* 2016;99:936–59.
- [31] Morse TL, Williamson CHK. Prediction of vortex-induced vibration response by employing controlled motion. *J Fluid Mech* 2009;634:5–39.
- [32] Khalak A, Williamson CHK. Motions, forces and mode transitions in vortex-induced vibrations at low mass-damping. *J Fluid Struct* 1999;13(7–8):813–51.
- [33] Luo ZM, Zhang LX. [Influence of parameters on extracting energy from a vortex-induced vibration]. *J Vib Shock* 2014;33(9):12–5 [Chinese].
- [34] Sun H, Ma CH, Kim ES, Nowakowski G, Mauer E, Bernitsas MM. Hydrokinetic energy conversion by two rough tandem-cylinders in flow induced motions: effect of spacing and stiffness. *Renew Energy* 2017;107:61–80.
- [35] Govardhan R, Williamson CHK. Resonance forever: existence of a critical mass and an infinite regime of resonance in vortex-induced vibration. *J Fluid Mech* 2002;473:147–66.
- [36] Lian JJ, Yan X, Liu F. [Development and prospect of study on the energy harness of flow-induced motion]. *South-to-North Water Transfers and Water Science & Technology* 2018;16(1):176–88 [Chinese].
- [37] Yuan JB, Xie T, Shan XB, Chen WS. [Review of current research on energy capture technology by voltage]. *J Vib Shock* 2009;28(10):36–44 [Chinese].
- [38] Kan JW, Fu JW, Wang SY, Zhang ZH, Cheng S, Jiang YH. [Research status and prospect of vortex-induced vibration micro-fluid energy harvester]. *Opt Precis Eng* 2017;25(6):1026–2 [Chinese].
- [39] Skop RA, Griffin OM. A model for the vortex-excited resonant response of bluff cylinders. *J Sound Vib* 1973;27:225–33.
- [40] Dai HL, Abdelkefi A, Wang L. Piezoelectric energy harvesting from concurrent vortex-induced vibrations and base excitations. *Nonlinear Dynam* 2014;77: 967–81.
- [41] Dai HL, Abdelkefi A, Wang L. Theoretical modeling and nonlinear analysis of piezoelectric energy harvesting from vortex-induced vibrations. *J Intell Mater Syst Struct* 2014;25(14):1861–74.
- [42] Akaydin HD, Elvin N, Andreopoulos Y. The performance of a self-excited fluidic energy harvester. *Smart Mater Struct* 2012;21(2):025007.
- [43] Mehmood A, Abdelkefi A, Hajj MR, Nayfeh AH, Akhtar I, Nuhait AO. Piezoelectric energy harvesting from vortex-induced vibrations of circular cylinder. *J Sound Vib* 2013;332:4656–67.
- [44] Erturk A, Inman DJ. A distributed parameter electromechanical model for cantilevered piezoelectric energy harvesters. *J Vib Acoust* 2008;130(4):041002.

- [45] Song RJ, Shan XB, Lv FC, Xie T. A study of vortex-induced energy harvesting from water using PZT piezoelectric cantilever with cylindrical extension. *Ceram Int* 2015;41:768–73.
- [46] Dai HL, Abdelkefi A, Yang Y, Wang L. Orientation of bluff body for designing efficient energy harvesters from vortex-induced vibrations. *Appl Phys Lett* 2016;108:053902.
- [47] Chakrabarti S. Handbook of offshore engineering (2-volume set). Elsevier; 2005.
- [48] Betz A. Introduction to the theory of flow machines. Oxford: Pergamon Press; 1966.
- [49] Plant D. Investigation of indentations versus surface roughness for fluid induced motion of an elastically attached circular cylinder at velocities relevant to the marine environment using CFD [dissertation]. Perth: Murdoch University; 2009.
- [50] Soti AK, Thompson MC, Sheridan J, Bhardwaj R. Harnessing electrical power from vortex-induced vibration of a circular cylinder. *J Fluid Struct* 2017;70:360–73.
- [51] Narendran K, Murali K, Sundar V. Investigations into efficiency of vortex induced vibration hydrokinetic energy device. *Energy* 2016;109(15):224–35.
- [52] Soti AK, Zhao JS, Thompson MC, Sheridan J, Bhardwaj R. Damping effects on vortex-induced vibration of a circular cylinder and implications for power extraction. *J Fluid Struct* 2018;81:289–308.
- [53] Sareen A, Zhao J, Jacomo DL, Sheridan J, Hourigan K, Thompson MC. Vortex-induced vibration of a rotating sphere. *J Fluid Mech* 2018;837:258–92.
- [54] Nakamura Y, Hirata K, Kashima K. Galloping of a circular cylinder in the presence of a splitter plate. *J Fluid Struct* 1994;8(4):355–65.
- [55] Park H, Mentzelopoulos A, Bernitsas MM. Hydrokinetic energy harnessing from slow currents using flow induced oscillations. In: Proceedings of the 39th international conference on offshore mechanics and arctic engineering; 2020 jun 28-jul 3; fort lauderdale, Florida. ASME; 2020.
- [56] Ding L, Zhang L, Wu CM, Mao XR, Jiang DY. Flow induced motion and energy harvesting of bluff bodies with different cross sections. *Energy Convers Manag* 2015;91:416–26.
- [57] Abdelkefi A, Hajj MR, Nayfeh AH. Power harvesting from transverse galloping of square cylinder. *Nonlinear Dynam* 2012;70:1355–63.
- [58] Abdelkefi A, Hajj MR, Nayfeh AH. Piezoelectric energy harvesting from transverse galloping of bluff bodies. *Smart Mater Struct* 2013;22(1):015014.
- [59] Abdelkefi A, Yan ZM, Hajj MR. Performance analysis of galloping-based piezoaeroelastic energy harvesters with different cross-section geometries. *J Intell Mater Syst Struct* 2014;25(2):246–56.
- [60] Javed U, Dai HL, Abdelkefi A. Nonlinear dynamics and comparative analysis of hybrid piezoelectric-inductive energy harvesters subjected to galloping vibrations. *Eur Phys J Spec Top* 2015;224:2929–48.
- [61] Blevins RD. Flow-induced vibrations. second ed. New York: Van Nostrand Reinhold; 1990.
- [62] Dai HL, Yang YW, Abdelkefi A, Wang L. Nonlinear analysis and characteristics of inductive galloping energy harvesters. *Commun Nonlinear Sci Numer Simulat* 2018;59:580–91.
- [63] Zhang BS, Mao ZY, Song BW, Ding WJ, Tian WL. Numerical investigation on effect of damping-ratio and mass-ratio on energy harnessing of a square cylinder in FIM. *Energy* 2018;144:218–31.
- [64] Zhao JS, Leontini J, Jacomo DL, Sheridan J. The effect of mass ratio on the structural response of a freely vibrating square cylinder oriented at different angles of attack. *J Fluid Struct* 2019;86:200–12.
- [65] Zhang BS, Wang K, Song BW, Mao ZY, Tian WL. Numerical investigation on the effect of the cross-sectional aspect ratio of a rectangular cylinder in FIM on hydrokinetic energy conversion. *Energy* 2018;165(Pt A):949–64.
- [66] Zhao JS, Hourigan K, Thompson MC. An experimental investigation of flow-induced vibration of high-side-ratio rectangular cylinders. *J Fluid Struct* 2019;91:102580.
- [67] Hénon P, Amandolesse X, Andrianne T. Energy harvesting from galloping of prisms: a wind tunnel experiment. *J Fluid Struct* 2017;70:390–402.
- [68] Cui ZD, Zhao M, Teng B, Cheng L. Two-dimensional numerical study of vortex-induced vibration and galloping of square and rectangular cylinders in steady flow. *Ocean Eng* 2015;106:189–206.
- [69] Sirohi J, Mahadik R. Piezoelectric wind energy harvester for low-power sensors. *J Intell Mater Syst Struct* 2011;22(18):2215–28.
- [70] Abdelkefi A, Yan ZM, Hajj MR. Modeling and nonlinear analysis of piezoelectric energy harvesting from transverse galloping. *Smart Mater Struct* 2013;22(2):025016.
- [71] Zhang J, Liu F, Lian JJ, Yan X, Ren QC. Flow induced vibration and energy extraction of an equilateral triangle prism at different system damping ratios. *Energies* 2016;9(938):1–22.
- [72] Lian JJ, Yan X, Liu F, Zhang J, Ren QC, Yang X. Experimental investigation on soft galloping and hard galloping of triangular prisms. *Appl Sci* 2017;7(198):1–27.
- [73] Zhang J, Xu GB, Liu F, Lian JJ, Yan X. Experimental investigation on the flow induced vibration of an equilateral triangle prism in water. *Appl Ocean Res* 2016;61:92–100.
- [74] Raghavan K, Bernitsas MM. Experimental investigation of Reynolds number effect on vortex induced vibration of rigid cylinder on elastic supports. *Ocean Eng* 2011;38(5–6):719–31.
- [75] Wang JL, Tang LH, Zhao LY, Zhang ZE. Efficiency investigation on energy harvesting from airflows in HVAC system based on galloping of isosceles triangle sectioned bluff bodies. *Energy* 2019;172:1066–78.
- [76] Alonso G, Meseguer J, Pérez-Grande I. Galloping instabilities of two-dimensional triangular cross-section bodies. *Exp Fluid* 2005;38:789–95.
- [77] Alonso G, Meseguer J, Pérez-Grande I. Galloping stability of triangular cross-sectional bodies: a systematic approach. *J Wind Eng Ind Aerod* 2007;95(9–11):928–40.
- [78] Yang YW, Zhao LY, Tang LH. Comparative study of tip cross-sections for efficient galloping energy harvesting. *Appl Phys Lett* 2013;102:064105.
- [79] Kwon SD. A T-shaped piezoelectric cantilever for fluid energy harvesting. *Appl Phys Lett* 2010;97(16):164102.
- [80] Sirohi J, Mahadik R. Piezoelectric wind energy harvester for low-power sensors. *J Intell Mater Syst Struct* 2011;22(18):2215–28.
- [81] Zhang BS, Song BW, Mao ZY, Tian WL, Li BY. Numerical investigation on VIV energy harvesting of bluff bodies with different cross sections in tandem arrangement. *Energy* 2017;133:723–36.
- [82] Lian JJ, Yan X, Liu F, Zhang J. Analysis on flow induced motion of cylinders with different cross sections and the potential capacity of energy transference from the flow. *Shock Vib* 2017;4356367.
- [83] Sun WP, Zhao DL, Tan T, Yan ZM, Guo PC, Luo XQ. Low velocity water flow energy harvesting using vortex induced vibration and galloping. *Appl Energy* 2019;251:113392.
- [84] Barrero-Gil A, Alonso G, Sanz-Andres A. Energy harvesting from transverse galloping. *J Sound Vib* 2010;329(14):2873–83.
- [85] Raghavan K, Bernitsas MM. Enhancement of high damping VIV through roughness distribution for energy harnessing at $8 \times 10^3 < Re < 1.5 \times 10^5$. ASME. In: Proceedings of the 27th international conference on offshore mechanics and arctic engineering; 2008 jun 15–20. Portugal: Estoril; 2008. p. 871–82.
- [86] Bernitsas MM, Raghavan K. Reduction/Suppression of VIV of circular cylinders through roughness distribution at $8 \times 10^3 < Re < 1.5 \times 10^5$. ASME. In: Proceedings of the 27th international conference on offshore mechanics and arctic engineering; 2008 jun 15–20. Portugal: Estoril; 2008. p. 1001–5.
- [87] Bernitsas MM, Raghavan K. Enhancement of vortex induced forces and motion through surface roughness control. United States Patent and Trademark Office. Patent #8,042,232 B2. Issued on November 1; 2011.
- [88] Kim ES, Bernitsas MM, Kumar RA. Selective roughness in the boundary layer to suppress flow induced motions of circular cylinder at $30,000 < Re < 120,000$. *J Offshore Mech Arctic Eng* 2012;134(4):041801.
- [89] Kinaci OK, Lakka S, Sun H, Fassezke E, Bernitsas MM. Computational and experimental assessment of turbulence stimulation on flow induced motion of a circular cylinder. *J Offshore Mech Arctic Eng* 2016;138(4):041802.
- [90] Chang CC, Bernitsas MM. Hydrokinetic energy harnessing using the VIVACE converter with passive turbulence control. In: Proceedings of the 30th international conference on ocean, offshore and arctic engineering; 2011 jun 19–24; rotterdam, Netherlands. ASME; 2011. p. 899–908.
- [91] Park H, Bernitsas MM, Kumar AR. Using the map of passive turbulence control to flow induced motions to suppress circular cylinder motion at $31,000 \leq Re \leq 120,000$. *J Offshore Mech Art* 2012;134(4).
- [92] Kim ES, Bernitsas MM, Kumar RA. Multicylinder flow-induced motions: enhancement by passive turbulence control at $28,000 < Re < 120,000$. *J Offshore Mech Arctic Eng* 2013;135:021802.
- [93] Ding L, Bernitsas MM, Kim ES. 2-D URANS vs. experiments of flow induced motions of two circular cylinders in tandem with passive turbulence control for $30,000 < Re < 105,000$. *Ocean Eng* 2013;72:429–40.
- [94] Ding L, Zhang L, Bernitsas MM, Chang CC. Numerical simulation and experimental validation for energy harvesting of single-cylinder VIVACE converter with passive turbulence control. *Renew Energy* 2016;85:1246–59.
- [95] Vinod A, Banerjee A. Surface protrusion based mechanisms of augmenting energy extraction from vibrating cylinders at Reynolds number 3×10^3 – 3×10^4 . *J Renew Sustain Energy* 2014;6:063106.
- [96] Quadrante LAR, Nishi Y. Attachment of tripping wires to enhance the efficiency of a vortex-induced vibrations energy generation system. *J Power Energy Syst* 2013;7(3):162–76.
- [97] Nishi Y, Ono K, Kokubun K. Development of a renewable energy system utilizing vortex induced vibration of a cylinder and principle of leverage aiming for application in deep sea. *J Mar Sci Technol* 2012;17:382–9.
- [98] Quadrante LAR, Nishi Y. Effects of tripping rods on the flow around a cylinder and VIV amplification. In: Proceedings of hydroelasticity conference; 2012 [Tokyo, Japan].
- [99] Igarashi T. Effect of tripping wires on the flow around a circular cylinder normal to an airstream. *Bulletin of JSME* 1986;29(255):2917–24.
- [100] Hover FS, Triantafyllou MS. Vortex-induced vibrations of a cylinder with tripping wires. *J Fluid Mech* 2001;448:175–95.
- [101] Alami MM, Sakamoto H, Moriya M. Reduction of fluid forces acting on a single circular cylinder and two circular cylinders by using tripping rods. *J Fluid Struct* 2003;18(3–4):347–66.
- [102] Quadrante LAR, Nishi Y. Amplification/suppression of flow-induced motions of an elastically mounted circular cylinder by attaching tripping wires. *J Fluid Struct* 2014;48:93–102.
- [103] Hu G, Tse KT, Kwok KCS, Song J, Lyu Y. Aerodynamic modification to a circular cylinder to enhance the piezoelectric wind energy harvesting. *Appl Phys Lett* 2016;109(19):193902.
- [104] Hu G, Tse KT, Wei MH, Naseer R, Abdelkefi A, Kwok KCS. Experimental investigation on the efficiency of circular cylinder-based wind energy harvester with different rod-shaped attachments. *Appl Energy* 2018;226:682–9.
- [105] Zhu HJ, Gao Y. Hydrokinetic energy harvesting from flow-induced vibration of a circular cylinder with two symmetrical fin-shaped strips. *Energy* 2018;165(Pt B):1259–81.
- [106] Hu G, Tse KT, Kwok KCS. Enhanced performance of wind energy harvester by aerodynamic treatment of a square prism. *Appl Phys Lett* 2016;108:123901.

- [107] Kowk KCS, Bailey PA. Aerodynamic devices for tall buildings and structures. *J Eng Mech* 1987;113(3):349–65.
- [108] Song J, Hu G, Tse KT, Li SW, Kwok KCS. Performance of a circular cylinder piezoelectric wind energy harvester fitted with a splitter plate. *Appl Phys Lett* 2017;111(22):223903.
- [109] Assi GRS, Bearman PW. Transverse galloping of circular cylinders fitted with solid and slotted splitter plates. *J Fluid Struct* 2015;54:263–80.
- [110] Liang SP, Wang JS, Hu ZM. VIV and galloping response of a circular cylinder with rigid detached splitter plates. *Ocean Eng* 2018;162:176–86.
- [111] Zhu HJ, Zhao HN, Yao J, Tang YB. Numerical study on vortex-induced vibration responses of a circular cylinder attached by a free-to-rotate dartlike overlay. *Ocean Eng* 2016;112:195–210.
- [112] Zhu HJ, Gao Y. Vortex induced vibration response and energy harvesting of a marine riser attached by a free-to-rotate impeller. *Energy* 2017;134:532–44.
- [113] Zhu HJ, Zhao Y, Zhou TM. CFD analysis of energy harvesting from flow induced vibration of a circular cylinder with an attached free-to-rotate pentagram impeller. *Appl Energy* 2018;212:304–21.
- [114] Ma CH, Sun H, Bernitsas MM. Nonlinear piecewise restoring force in hydrokinetic power conversion using flow induced motions of two tandem cylinders. *J Offshore Mech Arctic Eng* 2018;140(4):041901.
- [115] Zhang LB, Abdelkefi A, Dai HL, Naseer R, Wang L. Design and experimental analysis of broadband energy harvesting from vortex-induced vibrations. *J Sound Vib* 2017;408:210–9.
- [116] Nasser R, Dai HL, Abdelkefi A, Wang L. Piezomagnetoelastic energy harvesting from vortex-induced vibrations using monostable characteristics. *Appl Energy* 2017;203:142–53.
- [117] Mackowski AW, Williamson CHK. Nonlinear restoring forces in vortex-induced vibration. Nov 20–22. In: The 64th annual meeting of the APS division of fluid dynamics. APS; 2011.
- [118] Mackowski AW, Williamson CHK. An experimental investigation of vortex induced vibration with nonlinear restoring forces. *Phys Fluids* 2013;25(8):087101.
- [119] Wang EH, Xu WH, Gao XF, Liu LQ, Xiao Q, Ramesh K. The effect of cubic stiffness nonlinearity on the vortex-induced vibration of a circular cylinder at low Reynolds numbers. *Ocean Eng* 2019;173:12–27.
- [120] Tjahjowidodo T, Al-Bender F, Brussel HV. Quantifying chaotic responses of mechanical systems with backlash component. *Mech Syst Signal Process* 2007;21(2):973–93.
- [121] Facchinetti ML, Langre ED, Biolley F. Coupling of structure and wake oscillators in vortex-induced vibrations. *J Fluid Struct* 2004;19(2):123–40.
- [122] Farshidianfar A, Dolatabadi N. Modified higher-order wake oscillator model for vortex-induced vibration of circular cylinders. *Acta Mech* 2013;224:1441–56.
- [123] Pellegrini SP, Tolou N, Schenk M, Herder JL. Bistable vibration energy harvesters: a review. *J Intell Mater Syst Struct* 2012;24(11):1303–12.
- [124] Ramlan R, Brennan MJ, Mace BR, Kovacic I. Potential benefits of a non-linear stiffness in an energy harvesting device. *Nonlinear Dynam* 2010;59:545–58.
- [125] Huynh BH, Tjahjowidodo T. Experimental chaotic quantification in bistable vortex induced vibration systems. *Mech Syst Signal Process* 2017;85:1005–19.
- [126] Huynh BH, Tjahjowidodo T, Zhong ZW, Wang Y, Srikanth N. Design and experiment of controlled bistable vortex induced vibration energy harvesting systems operating in chaotic regions. *Mech Syst Signal Process* 2018;98:1097–115.
- [127] Sun H, Bernitsas MM. Bio-Inspired adaptive damping in hydrokinetic energy harnessing using flow-induced oscillations. *Energy* 2019;176(1):940–60.
- [128] Xu WH, Ji CN, Sun H, Ding WJ, Bernitsas MM. Flow-induced vibration of two elastically mounted tandem cylinders in cross-flow at subcritical Reynolds numbers. *Ocean Eng* 2019;173:375–87.
- [129] Kim S, Alam MM, Sakamoto H, Zhou Y. Flow-induced vibrations of two circular cylinders in tandem arrangement. Part 1: characteristics of vibration. *J Wind Eng Ind Aerod* 2009;97(5–6):304–11.
- [130] Prasanth TK, Mittal S. Flow-induced oscillation of two circular cylinders in tandem arrangement at low Re . *J Fluid Struct* 2009;25(6):1029–48.
- [131] Park H, Kumar AR, Bernitsas MM. Suppression of vortex induced vibrations of rigid circular cylinder on springs by localized surface roughness at $3 \times 10^4 \leq Re \leq 1.2 \times 10^5$. *Ocean Eng* 2016;111:218–33.
- [132] Park H, Bernitsas MM, Kim ES. Selective surface roughness to suppress flow-induced motion of two circular cylinders at $30,000 < Re < 120,000$. *J Offshore Mech Arctic Eng* 2014;136(4):041804.
- [133] Usman M, Hanif A, Kim IH, Jung HJ. Experimental validation of a novel piezoelectric energy harvesting system employing wake galloping phenomenon for a broad wind spectrum. *Energy* 2018;153:882–9.
- [134] Zhao M. Flow induced vibration of two rigidly coupled circular cylinders in tandem and side-by-side arrangements at a low Reynolds number of 150. *Phys Fluids* 2013;25(12):123601.
- [135] Sun H, Ma CH, Kim EO, Nowakowski G, Mauer E, Bernitsas MM. Flow-induced vibration of tandem circular cylinders with selective roughness: effect of spacing, damping and stiffness. *Eur J Mech B Fluid* 2019;74:219–41.
- [136] Xu WH, Ji CN, Sun H, Ding WJ, Bernitsas MM. Flow-induced vibration and hydrokinetic power conversion of two staggered rough cylinders for $2.5 \times 10^4 < Re < 1.2 \times 10^5$. *J Offshore Mech Arctic Eng* 2018;140(2):021905.
- [137] Xu WH, Ji CN, Sun H, Ding WJ, Bernitsas MM. Flow-induced vibration (FIV) and hydrokinetic power conversion of two staggered, low mass-ratio cylinders, with passive turbulence control in the TRSL3 flow regime ($2.5 \times 10^4 < Re < 1.2 \times 10^5$). In: Proceedings of the 36th international conference on ocean, offshore and arctic engineering; 2017 jun 25–30; trondheim, Norway. ASME; 2017.
- [138] Zhang LB, Dai HL, Abdelkefi A, Wang L. Experimental investigation of aerodynamic energy harvester with different interference cylinder cross-sections. *Energy* 2019;167:970–81.
- [139] Ding L, Zou QF, Zhang L, Wang HB. Research on flow-induced vibration and energy harvesting of three circular cylinders with roughness strips in tandem. *Energies* 2018;11(11):2977.
- [140] Ding L, Zhang L, Kim ES, Bernitsas MM. URANS vs. experiments of flow induced motions of multiple circular cylinders with passive turbulence control. *J Fluid Struct* 2015;54:612–28.
- [141] Wang EH, Xu WH, Yu Y, Zhou LD, Incecik A. Flow-induced vibrations of three and four long flexible cylinders in tandem arrangement: an experimental study. *Ocean Eng* 2019;178:170–84.
- [142] Wang HK, Yu GL, Yang WY. Numerical study of vortex-induced vibrations of three circular cylinders in equilateral-triangle arrangement. *Adv Mech Eng* 2013;287923.
- [143] Han P, Pan G, Tian WL. Numerical simulation of flow-induced motion of three rigidly coupled cylinders in equilateral-triangle arrangement. *Phys Fluids* 2018;30(12):125107.
- [144] Han P, Pan G, Jin ZH, Xia H. Vortex induced vibration of three rigidly coupled cylinders in equilateral triangle arrangement at small spacing ratio. *OCEANS 2018 MTS/IEEE charleston*. IEEE; 2018.
- [145] Xu F, Ou JP. [Numerical simulation of vortex-induced vibration of three cylinders subjected to a cross flow in equilateral arrangement]. *Acta Aerodyn Sin* 2010;28(5):582–90 [Chinese].
- [146] Goher HR, Shah BA, Lakdawala AM. Numerical investigation of flow induced vibration for the triangular array of circular cylinder. *Procedia Eng* 2013;51:644–9.
- [147] Zhao M, Cheng L. Numerical simulation of vortex-induced vibration of four circular cylinders in a square configuration. *J Fluid Struct* 2012;31:125–40.
- [148] Gao YY, Yang K, Zhang BF, Cheng KY, Chen XP. Numerical investigation on vortex-induced vibrations of four circular cylinders in a square configuration. *Ocean Eng* 2019;175:223–40.
- [149] Zhao M, Kaja K, Xiang Y, Cheng L. Vortex-induced vibration of four cylinders in an in-line square configuration. *Phys Fluids* 2016;28(2):023602.
- [150] Han ZL, Zhou D, He T, Tu JH, Li CX, Kwok KCS, et al. Flow-induced vibrations of four circular cylinders with square arrangement at low Reynolds numbers. *Ocean Eng* 2015;96:21–33.
- [151] Zhang BS, Mao ZY, Song BW, Tian WL, Ding WJ. Numerical investigation on VIV energy harvesting of four cylinders in close staggered formation. *Ocean Eng* 2018;165:55–68.
- [152] Vicente-Ludlam D, Barrero-Gil A, Velazquez A. Enhanced mechanical energy extraction from transverse galloping using a dual mass system. *J Sound Vib* 2015;339:290–303.
- [153] Xu-Xu J, Barrero-Gil A, Velazquez A. Dual mass system for enhancing energy extraction from vortex-induced vibrations of a circular cylinder. *Int J Mar Energy* 2016;16:250–61.
- [154] Nishi Y. Power extraction from vortex induced vibration of dual mass system. *J Sound Vib* 2013;332(1):199–212.
- [155] Nishi Y, Fukuda K, Shinohara W. Experimental energy harvesting from fluid flow by using two vibrating masses. *J Sound Vib* 2017;394:321–32.
- [156] Vicente-Ludlam D, Barrero-Gil A, Velazquez A. Optimal electromagnetic energy extraction from transverse galloping. *J Fluid Struct* 2014;51:281–91.